8-29-2017

Design, Synthesis and Characterization of Metal Oxide Adsorbents and Catalysts for Environmental Applications

Wei Zhong
University Of Connecticut, wei.zhong@uconn.edu

Design, Synthesis and Characterization of Metal Oxide Adsorbents and Catalysts for Environmental Applications

Wei Zhong, Ph.D.

University of Connecticut, 2017

In this thesis, I will focus on the design and synthesis of metal oxides as adsorbents and catalysts for different types of environmental applications, such as water remediation, biogas cleanup. Controlled synthesis of these materials with unique crystalline structures, physical, and chemical properties will be carried out to achieve an improved performance. Correlations between the material property and performance will be investigated by varieties of characterization methods.

In the first part, I will employ perovskite materials for catalytic wet air oxidation (CWAO) reactions for water remediation. $LaNiO_{3-\delta}$ (LNO) was applied for degradation of methyl orange (MO) azo dye in aqueous solutions under dark ambient conditions (room temperature, atmospheric pressure) without additional lights or chemical stimulants. The mechanism behind MO degradation by LNO under dark ambient conditions was unraveled by a series of characterization methods. Considering the large variety of perovskites in terms of constituents and composition, an excellent perovskite material should be tailorable for water remediation applications. Fuel cell performance for the double perovskite material $PrBaCo_2O_5$ (PBC) was briefly shown.

Wei Zhong, Ph.D.

University of Connecticut, 2017

In the second part, I will demonstrate a facile way for synthesizing mesoporous aluminas (MAs) with uniform and monomodal pores via a modified inverse micelle synthesis method. The effects of reaction times, surfactant chain lengths, and heat treatments on the textural properties of MA were adjusted to optimize the texture properties for biogas cleanup. The tuned MA of the large mesopore volume achieved high octamethylcyclotetrasiloxane (D4 siloxane) adsorption capacity, and maintained approximate 85% of its original adsorption capacity, demonstrating a sustainable adsorption performance and high potential for related industrial applications. Arsenic adsorption was performed to illustrate the application of MA for heavy metal removal.

The third part, I supported transition metals on optimized mesoporous alumina for methane oxidation. The texture properties were summarized and Temperature-programmed studies were used for understanding the mechanism for methane partial oxidation. Different ratios of copper supported on alumina were designed for methane combustion and exhibited improved performance with regard to the loading amount, which was explained by further characterization methods.

Design, Synthesis and Characterization of Metal Oxide Adsorbents and Catalysts for Environmental Applications

Wei Zhong

Bachelor of Engineering, Southwest University of Science and Technology, China, 2009

Master of Engineering, University of Science and Technology of China, 2012

A Dissertation

Submitted in Partial Fulfillment of the

Requirements for the Degree of

Doctor of Philosophy

at the

University of Connecticut

2017

APPROVAL PAGE

Doctor of Philosophy Dissertation

Design, Synthesis and Characterization of Metal Oxide Adsorbents and Catalysts for Environmental Applications

Presented by

Wei Zhong, Master of Engineering

Major Advisor _____

Dr. Steven L. Suib

Associate Advisor _____

Dr. S. Pamir Alpay

Associate Advisor _____

Dr. Yu Lei

University of Connecticut
2017

Dedicated to my family and friends

"Let not steadfast love and faithfulness forsake you; bind them round your neck; write them on the tablet of your heart."

Acknowledgement

I would like to express my sincere gratitude to my advisor Dr. Steven L. Suib for his continuous support, and encouragement throughout my graduate studies. He is the best advisor anyone can ask for. Things I have learned from Dr. Suib are not only about research, but also the enthusiasm to work, the positive attitude to others, and the responsibility. I am also grateful to my committee members, Dr. S. Pamir Alpay, Dr. Yu Lei, Dr. Jie He, Dr. Mark Aindow, and Dr. Puxian Gao for their generous help and advice. Also, I greatly appreciate Dr. Frank Galasso for his suggestion and motivation throughout my Ph.D. life, Dr. William Willis for patiently training me on XPS and helpful discussions, Dr. Mu-Ping Nieh for his guidance, Mrs. Bonnie Suib for giving us courage and help.

My sincere thanks also go to my colleagues and collaborators for their helpful discussion and generous contributions to my research and Ph.D. life, Dr. Ting Jiang, Dr. Sheng-Yu Chen, Dr. Zhu Luo, Dr. Yongtao Meng, Dr. Chung-Hao Kuo, Dr. David Kriz, Dr. Le Ge, Dr. Shoucheng Du, Dr. Curtis Guild, Dr. Yashan Zhang, Dr. Wenqiao Song, Dr. Sourav Biswas, Dr. Saiful Islam, Dr. Lakshitha Pahalagedara, Dr. Madhavi Pahalagedara, Dr. Ran Miao, Dr. Niluka Wasalathanthri, Dr. Jing Jin, Dr.Gavin Richards, Dr. Abdelhamid El-Sawy, Tahereh Jafari, Junkai He, Biswanath Dutta, Andrew Meguerdichian , Shannon Poges, Chris Monteleone, John Macharia, Yanliu Dang, Mahbubur Shakil, Yang Wu, Tharindu Ehsan Moharreri, Shanka Dissanayke and everyone else in Suib's group. I also thank the faculty for teaching the courses and chemistry department staff, Dr. Heng Zhang, Dr. You-Jun Fu, Charlene Fuller, Emilie Hogrebe, Osker Dahabsu, and all the IMS laboratory staff.

Finally, I especially thank my parents and friends. Their unconditional love and support keep me moving forward when times are rough. I could not imagine myself getting this far without them.

Table of Contents

List of Figures

List of Tables

Chapter 1. Introduction

1.1 Mesoporous Alumina

The researchers from Mobil Research and Development Corporation invented mesoporous molecular sieves, which revealed new possibilities for materials with large pore sizes and narrow pore size distribution. From then on, many papers published on the synthesis, characterization and application for mesoporous materials.[1] As for the synthesis of mesoporous silica, this area is well studied and understood.

The synthesis of mesoporous alumina is more complex than that of silica. Alumina is a well-known adsorbent and support for catalysis applications. The conventional production route is precipitation.[1] There are various aluminum oxide-hydroxide precursors, bayerite, nordstrandite, boehmite, pseudoboehmite, which can be transformed to different phases of alumina. Bagshaw, Pinnavaia, *et al.* [2,3] used non-ionic templates to synthesize mesoporous alumina through aluminum alkoxide hydrolysis. Vaudry *et al.*[4] adopted anionic carboxylic acids as direct agents for the synthesis of mesoporous alumina with pore size of 2 nm. Yada *et al.* [5,6] used dodecyl sulfate to synthesize lamellar and hexagonal mesostructures. Cabrera *et al.* [7] showed cationic cetyltrimethylammonium bromide can be used as the surfactant to adjust pore sizes of mesoporous alumina.

Electrostatic interaction is the synthesis base for M41S mesoporous molecular sieves. Other synthesis pathways include charge reverse, counter mediate, and neutral interaction. [1] The synthesis of mesoporous alumina uses all of these pathways. Pinnavaia *et al.* [2,3] employed non-ionic polyethylene oxides as surfactants and aluminum alkoxides as a precursor to synthesize mesoporous alumina with a wormhole motif. Luo *et al.* and Deng *et al.* [1,8] used triblock copolymers for synthesizing mesoporous alumina. Vaudry *et al.*[4] described anionic directing agents, lauric and stearic acids, for the synthesis of mesoporous alumina in alcohols, chloroform or formamide. And the precursors are aluminum alkoxides. Yada *et al.* [5,6,9] used precipitation methods with urea and sodium dodecyl sulfate to synthesize aluminum-based surfactant mesophases. Cabrera *et al.*[7]synthesized mesoporous alumina in cationic route by using hexadecyl trimethyl ammonium bromide and triethanol amine, which is a good procedure for tailoring the pore sizes.

1.2 Characterization

The main characterization methods for mesoporous alumina are X-ray powder diffraction (XRD), nitrogen sorption tests and transmission electron microscopy (TEM). The characterization results of XRD, nitrogen sorption tests and TEM should agree with each other. It is useful to detect the diffraction in the low value ranges of 2θ from XRD. There is usually only one diffraction line in contrast to several diffraction lines for siliceous mesoporous molecular sieves. [1] Since calcination can remove the organic phase, the intensity of the diffraction line increases after calcination.[1] The presence of low-angle diffraction peaks indicate the material is mesostructured or ordered.[10–12] Jaroniec *et al.* [12] illustrated the peak in low-angle XRD patterns indicate a uniform mesoporosity, which means the possibility of mesopores' organization. However, Pinnavaia *et al.*[3] reported that the low-angle XRD line may result from the regular separation between channel walls. For example, one peak can be shown in the low-angle range for wormhole-like mesoporous materials. Though regular in average diameter, the wormhole-like channels have no long-range order. That is, the channels appear to be packed randomly. Nitrogen sorption measurements are important techniques to provide information for mesoporous molecular sieves, i.e. surface areas, pore size distribution, and pore volume. The isotherms usually have a horizontal plateau because there are no larger pores. The steep increase in the adsorbed amount starts at a larger partial pressure with the pore size increasing.[1]

Adsorption is the adhesion of one or more components on the surface. The forces between moleculars in physisorption include the dispersion forces, repulsive forces, polarization, and field dipoles. Desorption is the reverse procedure of adsorption.[13] The external surface is the envelope encompassing the particles or agglomerates. While the internal surfaces are the walls of all pores and cavities.[13] There are six types of adsorption isotherms in physisorption (**Figure 1.1**). Type I isotherm is concave to the x axis, which are observed with microporous materials. Type II isotherm is seen with non-porous or macroporous solids, which means monolayer-multilayer adsorption. Type III isotherm is convex to the x axis, which is not common. Type IV isotherm has a characteristic hysteresis loop, which is due to capillary condensation in mesopores. The Kelvin equation describes the vapor pressure change on a curved surface, which suggests

that the fluid condenses at a vapor pressure below that saturated vapor pressure. [14] The initial part is monolayer-multilayer adsorption. Type V isotherm is uncommon, which is observed by porous materials. Type VI isotherm is multiplayer adsorption obtained with a non-porous material. The reasons for hysteresis are as follows: the contact angle during adsorption and desorption is different. There are also ink-bottle type pores; the shape of meniscus in cylindrical pores is different. Hysteresis loops may show varieties of shapes (**Figure 1.1**). H1 and H4 are extreme types. The branches of H1 are almost vertical, while they are horizontal in H4. Type H2 and H3 are intermediate shapes between the extreme conditions. The pore structures is reflected from the shape of the hysteresis loop. H1 type has narrow pore size distribution, with agglomerates of uniform spheres in approximately a regular array. H2 type is hard to describe, which may be attributed to simplified "ink bottle" pores. An H3 type loop has no limiting adsorption at high relative pressure, which is obtained for slit-shaped pores formed by plate-like particles. An H4 type loop is observed for narrow slit-like pores. [13]

The common methods for calculating surface area are Langmuir and Brunauer-Emmett-Teller (BET) methods. The Langmuir model is suitable for monolayer adsorption. The BET method is the well-known way to determine the surface area of porous materials, which extends the model to multilayer coverage. The BET equation is as follows:

$$\frac{P}{n^a*(P^0-P)} = \frac{1}{n_m^a*C} + \frac{(C-1)P}{n_m^a*CP^0} \quad [1]$$

(n^a – the adsorbed amount at the relative pressure P/P^0, n_m^a – monolayer capacity, C- BET constant).

Total surface area is given by equation [2].

$$\mathrm{SA} = \frac{n^a\ N}{M} * A_{acs} \quad [2]$$

(N-Avagadro number, M-the molecular weight of adsorbate, A_{acs} - cross sectional area of adsorbate)

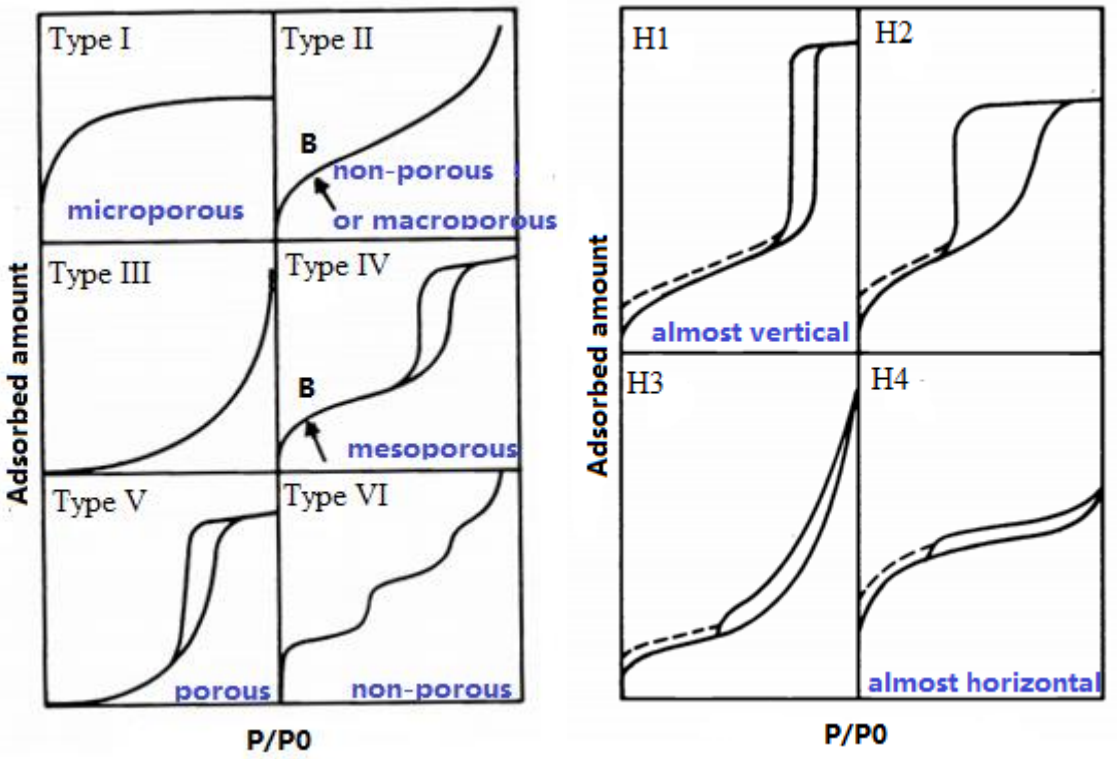

Figure 1.1 Types of physisorption isotherms and hysteresis loops. Adapted from[13]

Specific surface area is total surface area divided by the weight of sample. A linear relationship between $P/n^a * (P^0 - P)$ and P/P^0 usually exists in the range of 0.05-0.3. The pore size distribution is the distribution of pore volume corresponding to pore size. The Barrett, Joyner & Halenda (BJH) method is a modified Kelvin equation, which calculates pore size distributions from isotherms and applies to mesoporous materials. Density Functional Theory (DFT) is based on statistical mechanics, which deals with the sorption phenomena in micropores and mesopores.[15]

TEM characterizes pore sizes and channel ordering. In TEM images of mesoporous materials, wormhole-like or sponge-like pores show no apparent order of the pores in the arrangement. Ordered mesostructures

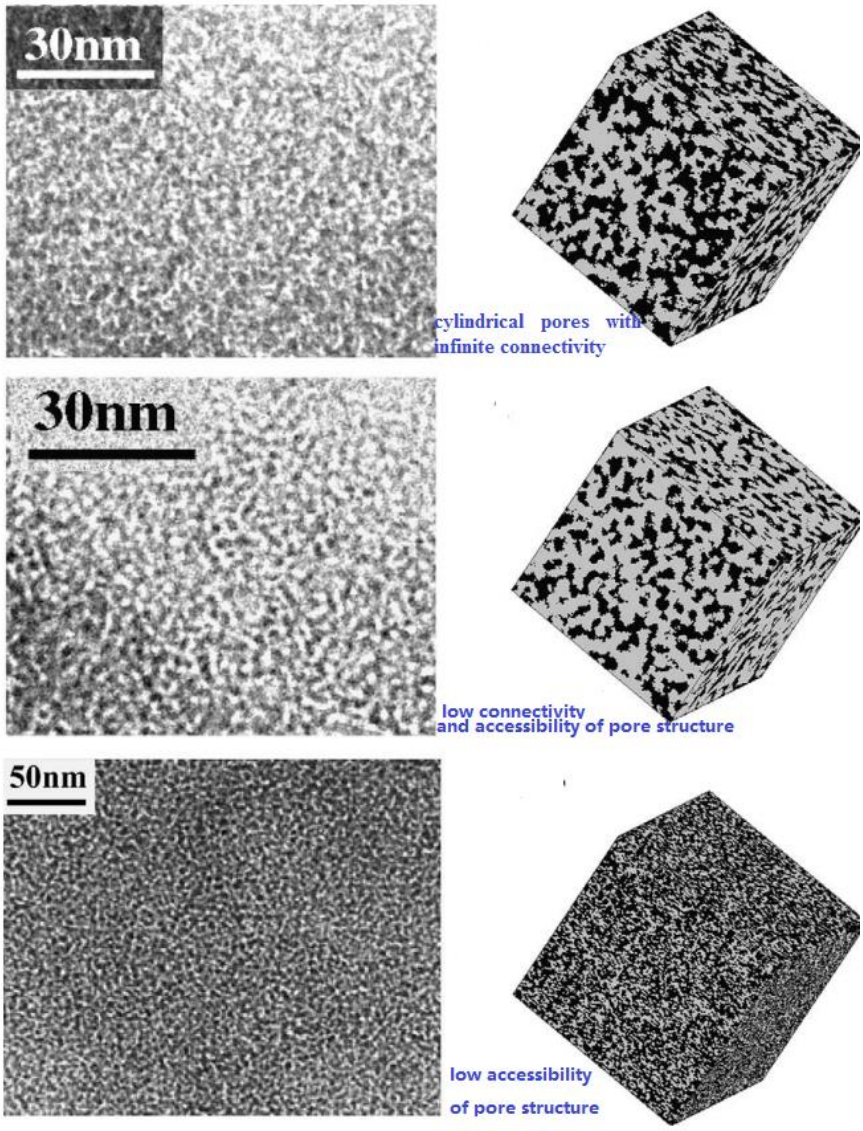

Figure 1.2 TEM images of alumina samples synthesized in the presence of poly(oxyalkylene) block polymers. 3-D reconstructed images of modified porous alumina (black colour corresponds to void space and grey colour to solid phase). Adapted from [155]

like siliceous MCM-41 have long-range channels with hexagonal arrangements.[3] For the reported mesostructured alumina, the low-angle XRD peak (position, width, and intensity) changes with synthesis conditions, which provides little structural information. [16] For example, XRD combined with nitrogen sorption analysis interpret the channel motifs as "wormhole-like". TEM studies show that those materials could have varieties of different porous structures, as shown in **Figure 1.2**. Mesoporous alumina prepared

using polyoxyalkylene polymers as surfactant has no ordered pores when observed from the TEM images. In the XRD patterns there are no changes seen when chelating agents and solvents change, though N_2 sorption tests show obvious modifications. Although the wormhole-like TEM images appear for these systems, Stochastic reconstruction methods can illustrate their differences in terms of connectivity. However, the reconstruction methodology has to be further verified using quantitative data of structural properties for materials.

MAS NMR can provide the coordination of aluminum. As reported in the literature, [3,17] the most intense peak lies at 5-6 ppm, which corresponds to the aluminum atoms in an octahedral coordination. Calcination during the temperature range of 500-800 ^{o}C does not obviously change the coordination of aluminum.[1]

1.3 Adsorption

Adsorption is the enrichment of a gas or liquid occurring on the material surface, which is of great importance.[18] Adsorbents are used for purifying liquids, separating gases or controlling drug delivery, etc. Moreover, adsorption plays a key role in numerous solid reactions. As previously discussed for the nitrogen sorption characterization technique, gas adsorption is used for surface property measurements. The interaction between the adsorbate and adsorbent has two kinds of forces, such as physisorption and chemisorption. Compared to various adsorption isotherms of physisorption, Type I isotherms are generally shown for chemisorption due to a chemically bound monolayer.

A physical treatment for siloxanes is required because of their inert properties.[19] Subrenat *et al.* reported for activated carbon that the adsorption velocity is more rapid than zeolites or silica gels due to their high surface areas. The adsorption capacity is also high for activated carbon because of its high surface area and adsorption capacity. The reduced adsorption capacity of linear siloxane L2 may be a result of a disruptive effect of the methyl group. The adsorption capacities decrease with the increasing temperature and humidity has a strong effect on the adsorption capacity of silica gel.

1.4 Texture and Surface Properties

Aluminas synthesized by different methods have different properties. Alumina hydrate (gibbsite, boehmite, bayerite) is produced through hydrolysis or precipitation of aluminum precursors, such as nitrate, alkoxides.[20] Calcination of boehmite at 400-800 ^{o}C produces gamma alumina. W. El-Nadjar *et al.* showed that textural properties depend on synthesis routes. Aluminas synthesized by precipitation have the lowest surface areas, while sol-gel methods achieve higher surface areas. [20] The pore size is around 5-8 nm when P123 is used as a surfactant. Alumina prepared by the EISA route shows hexagonal pore structure, while sol-gel or precipitation routes result in less organized pore structures.

Infrared spectra is used to characterize free hydroxyl groups of O-H stretching bands in the range of 3900-3500 cm^{-1}. There are five types of OH groups on the alumina surface, which are determined by the number of bonding Al^{3+} ions and the coordination number of Al^{3+}. [20] Alumina synthesized by the EISA method shows strong Lewis acid sites compared to sol-gel or precipitation methods. However, the synthesis method affects the ratio between perturbed hydroxyl groups and Lewis acid sites. [20]

1.5 Catalytic Methane Oxidation

Enrique Iglesia *et al.* [21] described reaction paths for C-H bond activation of methane on Pd clusters. The C-H bond cleaves on oxygen-saturated Pd, Pd, or PdO clusters through homolytic H-abstraction, oxidation addition, or sigma-bond metathesis pathways, respectively. P. Hu *et al.* [18] used *in situ* studies combining photoelectron spectroscopy and vibrational spectroscopy to explore the mechanism of methane oxidation over $NiCo_2O_4$. C-H dissociation is followed by CH_3 species that couple with lattice oxygen atoms to form CH_3O, which is due to the low binding energy of CH_2 on the separated Ni cation sites. [18]

Chapter 2. Effect of Lanthanum Carbonate on Dye Degradation by Perovskite-type $LaNiO_{3-\delta}$ Material

2.1 Introduction

The serious organic pollution of water sources, including dye effluents, has become a hot topic in recent years. To date, advanced oxidation processes (AOPs), such as photocatalysis,[22] Fenton-like reactions,[23] and wet air oxidation (WAO),[24] are possibly the best technologies to eliminate serious organic pollutants in water.[25–28] The widely used photocatalyst TiO_2 is only active in the ultraviolet light range and the quantum yield is not satisfying.[29] For Fenton-like reactions, consumption of H_2O_2 is huge.[29] Among AOPs, the WAO process is known to effectively treat effluents with a high content of organic matter, for which direct biological purification is inappropriate.[25] WAO performance can be enhanced by using catalysts (CWAO) under milder conditions, however, a temperature in the range of 80-180 ^oC and a pressure in the range of 1-5 MPa are required.[30] Due to the lack of stability of solid catalysts in water and complicated designs inherent to the multiphase nature of the CWAO reactors, industrial applications of CWAO remain scarce.[31] The best catalysts now are noble metal-based. Therefore, low-cost, environmentally friendly catalysts with high stability and activity at lower temperature and pressure are desired for CWAO.[30,32–36]

It is of great interest to degrade dye under dark ambient conditions (room temperature, atmosphere pressure) without additional lights or chemical stimulants. Recently some groups have reported organic pollutant degradation under ambient conditions.[24,30,32–35,37,38] For example, Wu *et al*.[29] catalytically degraded methyl orange using layered perovskite $La_4Ni_3O_{10}$ under dark ambient conditions. Li *et al*.[39] reported La_2NiO_4 that exhibited high activity to mineralize 4-chlorophenol even in the dark. Dvininov *et al*.[38] found Pt-$HCa_2Nb_3O_{10}$ could catalyze air oxidation of methyl orange without light at room temperature. Leiw *et al*. [37] explored $SrFeO_{3-\delta}$ on degradation of bisphenol A and methyl orange under dark ambient conditions. Sun *et al.* [40] reported $LaCoO_{3-\delta}$ had dye degradation activity in the dark.

Perovskites, with formula ABO_3, are probably the most studied mixed-oxide systems in heterogeneous catalysis. A and B are cations and O is an oxygen anion. In the ideal cubic structure (**Figure 2.1**), B cation

is surrounded by an octahedron of anions, and A cation has cuboctahedral coordination. In the antiperovskite structure, the cation and anion are in the reversed positions compared to the corresponding perovskite unit cell. Recently, perovskite type materials were evaluated as substitute candidates for noble metals in water depollution by Royer *et al.* [31] In 1985, Fierro *et al.*[41] studied a series of $LaMO_3$ (M: first row transition metal) perovskite-type materials and concluded that the best catalysts for gas phase oxidation reactions are $LaCoO_3$, $LaNiO_3$, $LaMnO_3$, which readily adsorb oxygen and are easily reduced. Cobalt, nickel, and manganese-based perovskites are mostly studied in gas phase oxidation reaction.[42–44] Nickel-based $LaMO_3$ perovskites are reported in few water remediation studies. An insight into the catalytic properties and electrical conductivity changes of $LaNiO_3$ in the oxidation of ethanol, acetaldehyde, and methane at temperatures higher than 150 ^oC was gained by Ling *et al.*[45,46] The oxidation reaction was

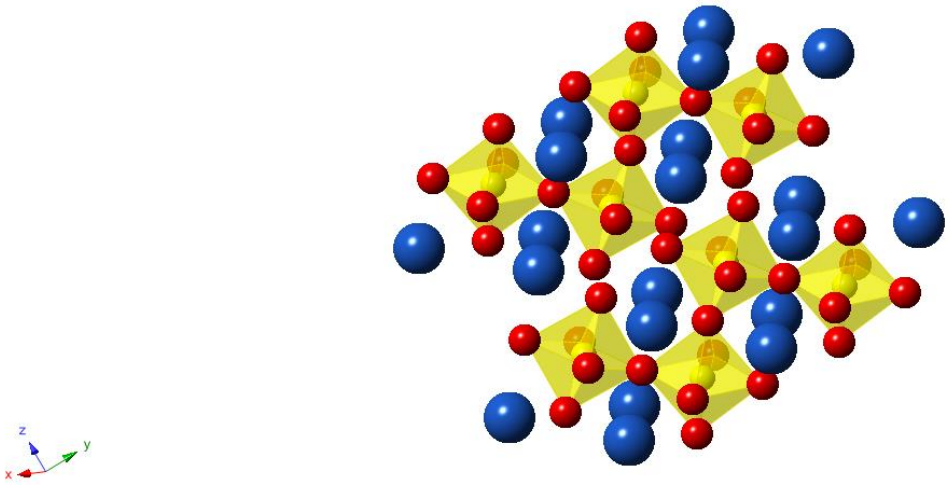

Figure 2.1 Structure of perovskite $LaNiO_3$. (Blue-La, Yellow-Ni, Red-O)

accompanied by loss of lattice oxygen. Visible light driven photocatalytic activity of $LaNiO_3$ was reported by Li *et al.*[47] The degradation percentage of 10 ppm methyl orange over 2 g L^{-1} $LaNiO_3$ was about 74.9% after 5 h.

In other fields of study, mixed nickelates are of particular interest, as the presence of Ni^{3+} and oxygen non-stoichiometry are shown to enhance their catalytic properties.[48] As a native p-type semiconductor, $LaNiO_3$ has broad applications as electrodes, ferroelectric materials, and conductive thin films due to excellent electronic and magnetic performance.[47,49–51]

However, carbonate phase can be formed on perovskites during reaction. [31,42] Structure collapse is a huge concern for perovskite-type oxide catalysts when they are applied to liquid-phase reaction systems or exposed to ambient environments.[52–55] Thus the relationship between perovskite structure and catalytic activity during reaction is an important issue.

To expand the application of perovskite type materials, it is necessary to understand the role this kind of material plays in aqueous phase reactions. Methyl orange (MO), a probe compound of azo dye, can be degraded by $LaNiO_{3-\delta}$ (LNO) even under dark ambient conditions with a fast rate and high degradation efficiency. Comparative details of the degradation efficiency and reaction conditions between LNO and ambient catalysts with similar structures or degradation profiles are also listed in **Table 2.1**.This observation prompted our study to determine the mechanism behind this process. Few have reported LNO as a catalyst for dye degradation under dark, mild conditions. No explanations have been claimed for such phenomena of LNO perovskite type materials so far. In this work, we identified the intermediates formed during MO degradation by LNO, and the mechanism behind this phenomena. Moreover, carbonate formed on LNO acts to synergistically decompose MO.

Table 2.1 Comparative details of the degradation efficiency and reaction conditions of $LaNiO_{3-\delta}$ (LNO) and reported catalysts with similar structures or degradation profiles.

Catalyst	Reaction conditions	Degradation profile[#]	Reference
LNO (calcined at 700 ^{o}C)	Dye : methyl orange 5 ppm (stirring speed: 500 rpm) Catalyst loading : 1.5 g/L Conditions: ambient; dark Inputted oxidant: None	Efficiency : 94.3%, after 4 h New absorbance peak: 244 nm (intermediate species)	This work
$LaNiO_3$	Dye : methyl orange 10 ppm Catalyst loading : 2 g/L Conditions: visible-light	Efficiency : 74.9%, after 5 h	[47]
	Inputted oxidant: None	NA*	

$La_4Ni_3O_{10}$	Dye : methyl orange 5 ppm (stirring speed: 500 rpm) Catalyst loading : 1.5 g/L Conditions :ambient	Efficiency: ~70%, after 3.5 h; ~80%, after 48 h (Dark, without stirring)	[29]
	Inputted oxidant: None	New absorbance peak: 244 nm (aromatic intermediates)	
La_2NiO_4	Dye : methyl orange 5 ppm (stirring speed: 500 rpm) Catalyst loading : 1.5 g/L Conditions: 30^oC;dark	Efficiency : 70%, after 12 h	[39]
	Inputted oxidant: None	NA	
$BaFeO_{3-\delta}$ (calcined at 700 ^oC)	Dye : methyl orange 20 ppm Catalyst loading : 1 g/L Conditions :ambient; dark	Efficiency: ~ 40%, after 50 h	[56]
	Inputted oxidant: None	NA	
$LaCoO_{3-\delta}$ (calcined at 700 ^oC)	Dye : methyl orange 20 ppm Catalyst loading : 1 g/L Conditions: ambient; dark	Efficiency : ~12.5%, after 45 h	[57]
	Inputted oxidant: None	NA	
Pt-$HCa_2Nb_3O_{10}$	Dye : methyl orange 20 ppm Catalyst loading : 0.67 g/L Conditions: ambient; dark Inputted oxidant: None	Efficiency : ~30%, after 250 min New absorbance peak:374 nm (intermediate species)	[38]

degradation efficiency is according to dye concentration percentage with time in references.

* NA: not available

2.2 Experimental

2.2.1 Catalyst Preparation

All chemical reagents purchased from Sigma-Aldrich Co. were of analytical grade and used without further purification. In a typical citrate sol-gel synthesis, 12 mmol of La $(NO_3)_3 \cdot 6H_2O$, and 12 mmol of Ni $(NO_3)_2 \cdot 6H_2O$ were dissolved in 30 mL of distilled deionized water (DDW). Citric acid 48 mmol with

another 30 mL DDW was added into the solution above. The resulting light green solution was kept at 70-80 ^{o}C for 3 h, and was then transferred into an oven at 100 ^{o}C overnight. The obtained green gel was calcined at 500 ^{o}C in a furnace for 3 h, yielding a fluffy black product. The product was ground in a marble mortar and annealed at 700 ^{o}C for 3 h to get the desired material. Catalysts reclaimed after reaction were washed with ethanol and acetone for three times each and dried at room temperature in a vacuum oven. Reclaimed catalysts are named as LNO-after-reaction conditions, for example, LNO-after-ambient represents LNO reclaimed from dark ambient conditions.

2.2.2 Characterization

X-ray diffraction (XRD) measurements were conducted using a Rigaku Ultima IV diffractometer with Cu Kα radiation (1.5406 Å wavelength), a beam voltage of 40 kV, and a current of 44 mA. The morphology was observed using a field emission scanning electron microscope (FE-SEM, JEOL 6335F) equipped with an energy-dispersive X-ray analysis (EDS) system. The surface area of the material was determined by using the Brunauer-Emmett-Teller (BET) method on a Quantachrome Autosorb-1-1C automated adsorption system. Thermogravimetric analysis was performed on a TA instrument TGA Q500. The measurement was taken from 25 ^{o}C to 900 ^{o}C at a ramp rate of 10 ^{o}C per minute under N_2 atmosphere. X-ray photoelectron spectroscopy (XPS, ΦPhysical Electronics Industries Inc.) was carried out to analyze the chemical state of surface elements of the materials. Fourier transform infrared spectroscopy (FTIR, Nicolet Magna 560) with TGS detector was used to detect organic groups on LNO after the reaction if there are any.

2.2.3 Catalytic Test and Analytical Methods

The reaction was performed at room temperature and atmospheric pressure. Herein the dark condition was simulated by using a 250 mL beaker wrapped with aluminum foil leaving several small holes on the cover. Typical catalytic reaction conditions as described were used unless specifically stated otherwise. For each test, 0.15 g of LNO was added into 100 mL of MO solution with an initial concentration of 5 ppm in a beaker. The sonication of 5 min (pulse on: 10 s; pulse off: 2 s; amplitude: 20 %) was used to evenly

distribute LNO in MO solution. This suspension was further kept under magnetic stirring at a speed of 500 rpm. At given time intervals, ca. 3 mL of the suspension was sampled and pressed through an Acrodisc 0.45 μm syringe filter (Pall Corporation, MI) to remove any solid particulates to avoid scattering the incident beam of the UV-vis spectrometer. The sample solutions were then put into quartz UV-vis cells (path length=1.0 cm), and the absorbance spectra were measured using a Shimadzu UV-2450 ultraviolet-visible spectrophotometer (Shimadzu Scientific Instruments, Tokyo, Japan).

A calibration curve for the dye was made by measuring the λ_{max} for a series of standard solutions. A linear calibration curve for MO concentrations was obtained according to Beer's law (**Figure 2.2**). The decrease in absorption intensity at 464 nm for MO dye was monitored to calculate the concentration and determine the percentage [% =C/C_0*100%, where C and C_0 are the final and initial (0 h) concentrations, respectively, shown in Figure S1, average of three trials, Mean ± SD].The dye degradation intermediates were identified by a Quattro II mass spectrometer (Waters, USA) with a Z-spray electrospray ionization (ESI) source in negative mode. Shimadzu HPLC instrument equipped with Zorbax SB-C18 column (5 um, 150 mm × 2.1mm) was used for the sample solution analysis. Eluent solution was an acetonitrile-10 mM ammonium formate (20/80, v/v) solution with flow rate at 0.6 ml/min. For each analysis, a10 μL sample was injected

into the instrument by an auto-sampling device and the UV-vis detector was operated at 464 nm to detect the MO dye and its degradation by-products.

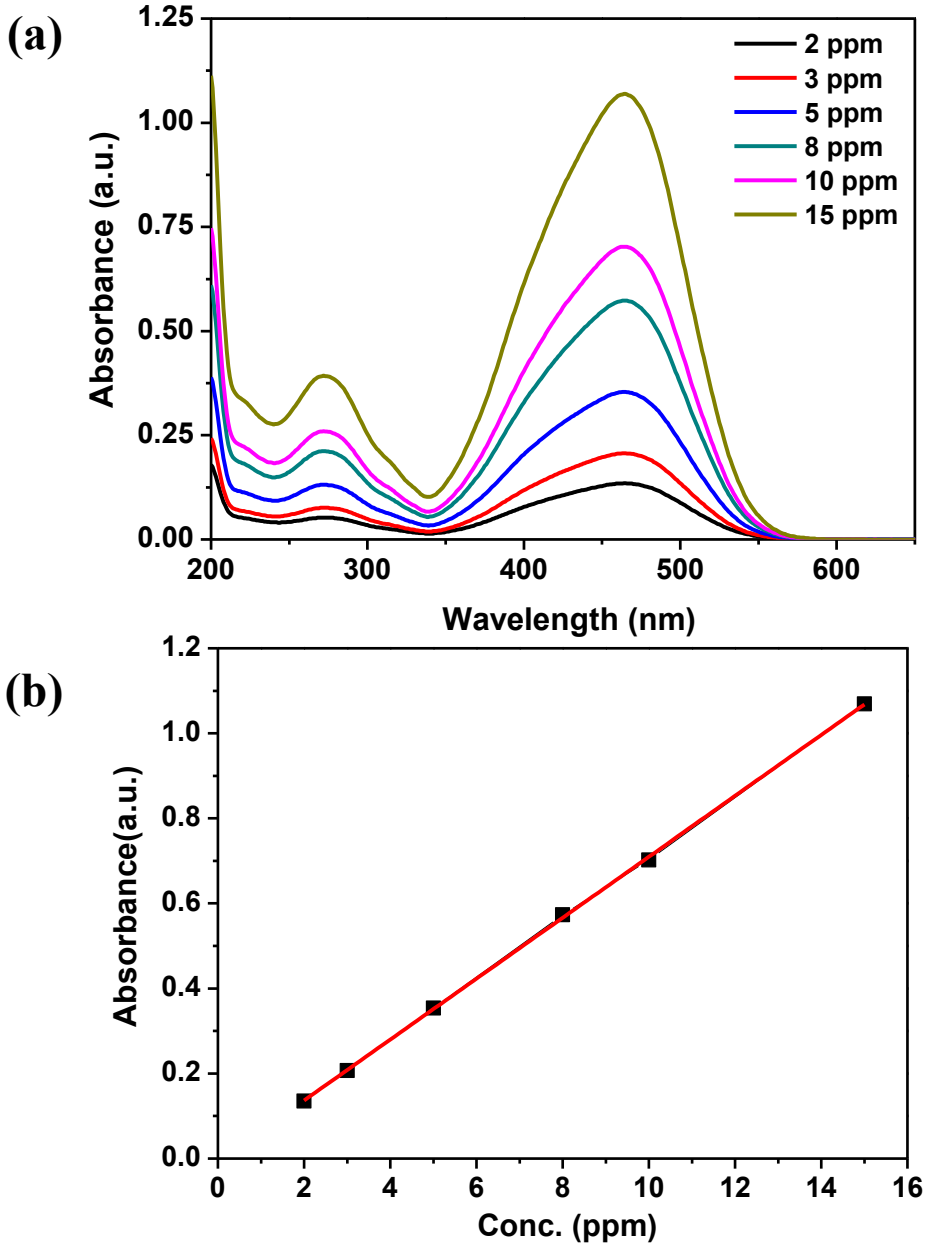

Figure 2.2 (a) MO standard solution UV-vis spectra; (b) MO linear calibration curve[#].

#a linear calibration curve for series of MO standard solution was obtained. A=0.07164*C-0.00676(R^2=0.99977, A-absorbance, C-concentration)

2.2.4 Reaction under Specific Gas (N_2, O_2, or CO_2) Condition

A 100 mL portion of 5 ppm MO solution was kept in a conical flask sealed with a rubber septum. The dye solution was degassed by purging nitrogen into the bottom solution overnight through a long glass tube. A 0.15 g portion of LNO was put in a 3-neck flask with a pressure equalized dropping funnel, which was sealed with a Precision Seal Septum to create a closed system. A vacuum pump was connected to the flask covered with aluminum foil. Before the experiment, the degassed MO solution was added into the funnel with a syringe. One valve was opened to evacuate the system. MO solution was transferred into the flask after evacuation for 2 h and was constantly stirred during reaction. After another 2 h, N_2 was purged in the system. This degradation experiment was conducted with N_2 being purged throughout the experiment. Reactions under O_2 or CO_2 condition used a similar procedure.

2.3 Results

2.3.1 Structure of LNO and LNO-after-Ambient

The X-Ray Diffraction pattern of as-formed LNO is presented in **Figure 2.3**. All peaks correspond well to those of JCPDS card number 34-1181.This material has a rhombohedral structure with space group R-3c.[58] The SEM image of as-formed LNO is shown in **Figure 2.4**. LNO is composed of blocks with average particle size of approximately 50 nm. Only La, Ni, and O elements are detected by EDS (

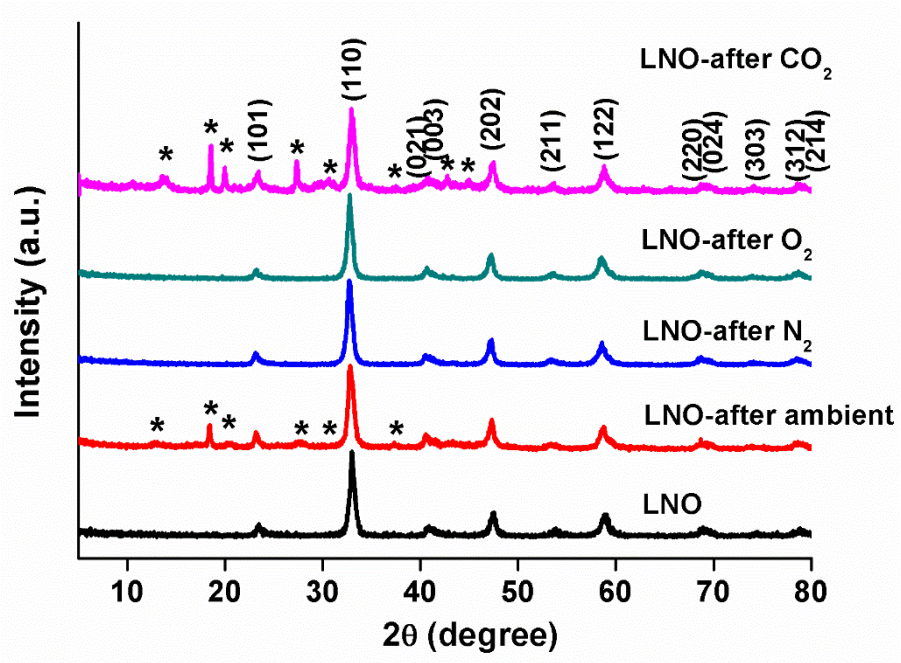

Figure 2.3 The powder XRD patterns of as-formed LNO, LNO-after reaction under dark ambient condition #, LNO after reaction under nitrogen, oxygen and carbon dioxide. #labeled with (hkl) for LaNiO3-δ (JCPDS card #34-1181) and peaks of an impurity phase labeled by*.

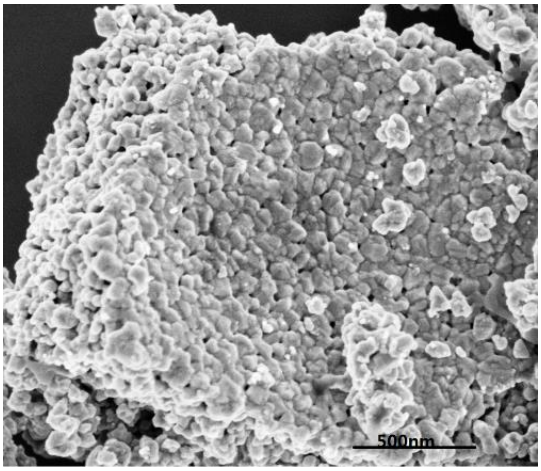

Figure 2.4 SEM image of as-formed LNO.

Table 2.2), and the atomic ratio of La:Ni is 1.07, matching stoichiometric value of 1. The measured surface area of LNO is 6 m^2g^{-1}.

Table 2.2 EDS of As-formed LNO[#].

Elements	wt. %	at. %	La:Ni
La	62.6	27.1	
Ni	24.7	25.3	1.07
O	12.7	47.7	
Total	100	100	

#EDS was obtained from three different sites on as-formed LNO.

LNO-after-ambient shows all of the peaks recorded for the as-formed LNO, as well as peaks at 13.94°, 18.46 °, 19.92°, 27.36 °, 30.56 °, 37.36 °, representing an impurity phase. These peaks indicate the formation of lanthanum carbonate (lanthanum-analog calkinsite). This is confirmed by FTIR and TGA measurements.

FTIR spectra of MO, as-formed LNO and LNO-after-ambient are shown in **Figure 2.5**. The spectrum for LNO-after-ambient shows peaks at wavenumbers 1471, 1373, 1049, 850, 748 cm^{-1}, which are not found in the FTIR spectrum of MO or as-formed LNO. They can be assigned to carbonate and H_2O. There are two main weight loss steps for LNO-after-ambient in the TGA curve (**Figure 2.6**). The first one is ~15% at 488 °C, the second one is ~3% at 767 °C. These amount to a total loss of ca. 18%. SEM images of as-formed LNO and LNO-after-ambient are shown in **Figure 2.7**. The relatively smooth surface of LNO before reaction, is covered with plate-like grains after reaction.

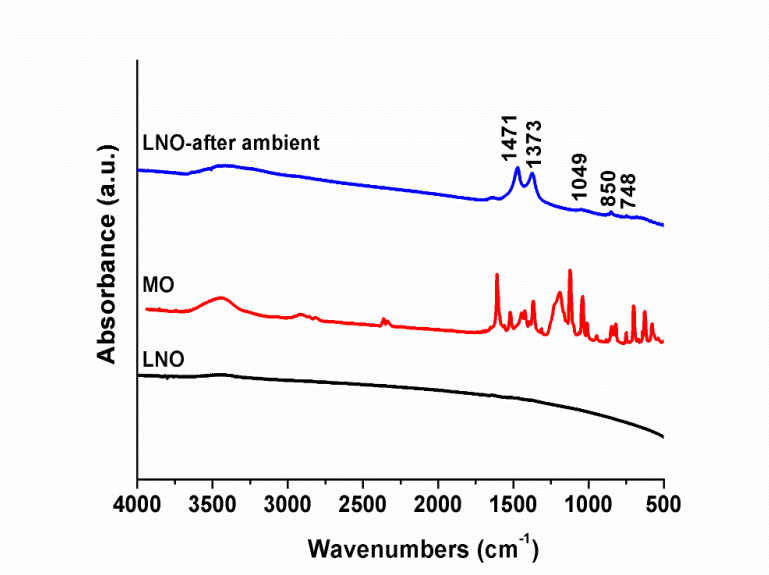

Figure 2.5 FTIR spectra of as-formed LNO, MO, LNO after reaction under dark ambient condition.

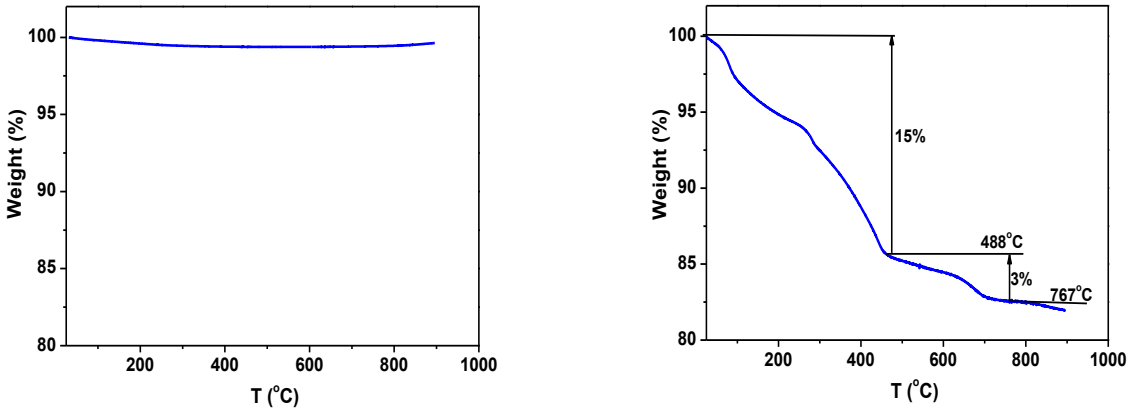

Figure 2.6 TGA curve of (a) as-formed LNO (b) LNO after reaction under ambient dark conditions.

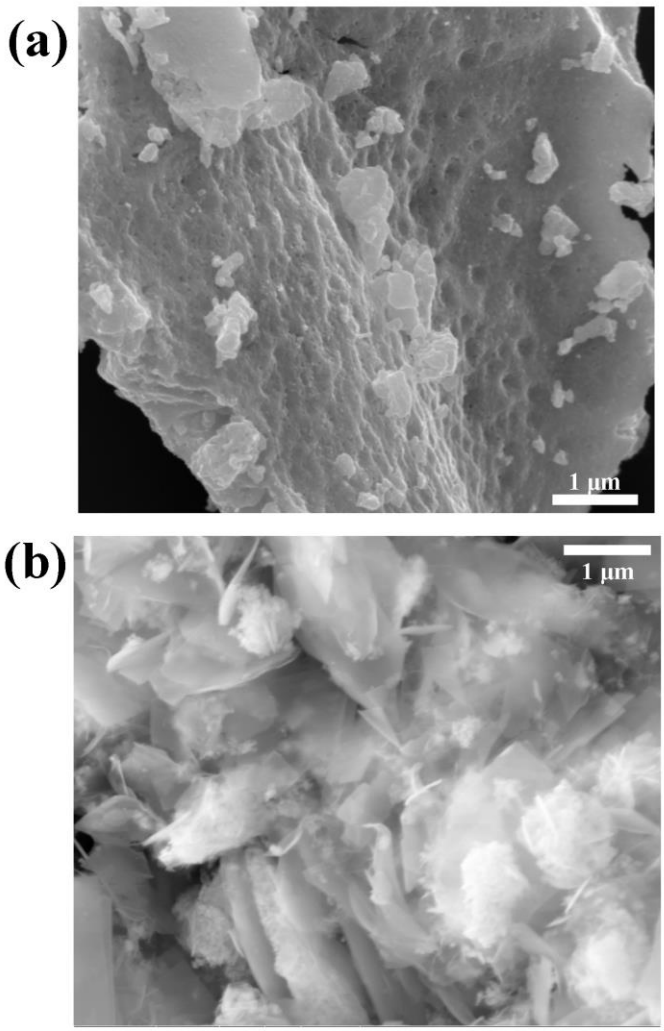

Figure 2.7 SEM images of LNO (a) before reaction and (b) after reaction under dark ambient conditions.

2.3.2 Degradation Profiles and Intermediate Analysis

The MO UV-vis spectrum under ambient dark conditions is shown in **Figure 2.8**. Pure MO aqueous solution, labeled as "0h", has weak (270 nm) and strong absorptions (464 nm) in the UV and visible spectral regions, respectively. The absorbance value of peak at 464 nm decreases with reaction time. However, a new peak occurs at ca. 244 nm, which increases first and then decreases. After 4 h, there is almost no absorption at 464 nm and the absorbance at 244 nm is maximized.

The species formed during MO degradation under dark ambient conditions were investigated by ESI/MS experiments. ESI/MS spectra of MO aqueous solution at 0 h, 4 h are presented in **Figure 2.9**. One main peak corresponding to a species at m/z=304.1 was observed before reaction (0 h). This species at m/z=304.1

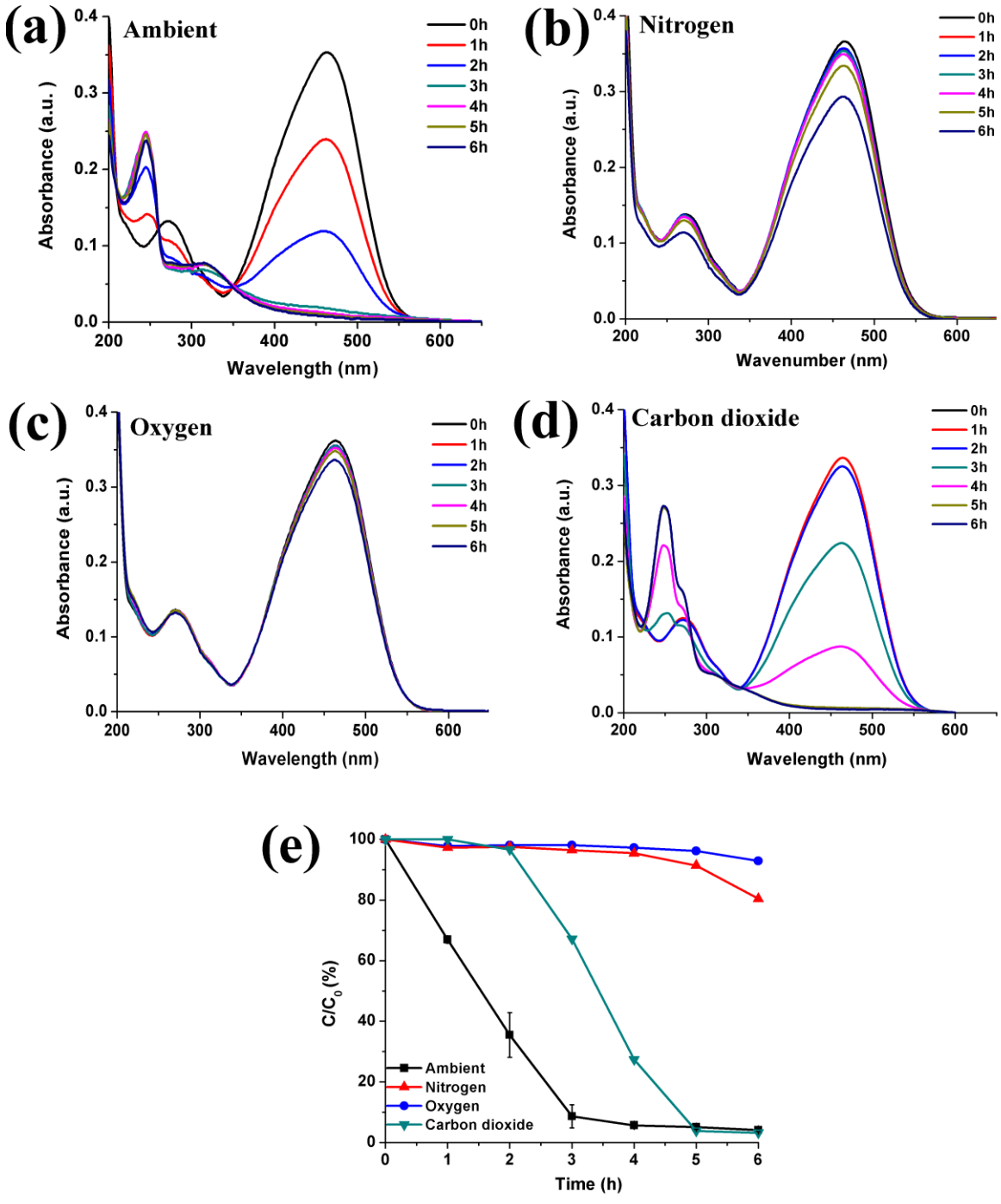

Figure 2.8 Sampled MO UV-vis spectra (a) under ambient dark condition, (b) under nitrogen, (c) under oxygen, (d) under carbon dioxide and (e) MO concentration percentage with time under different conditions[#]. [#]reaction parameters: MO-5 ppm, LNO-1.5 g L^{-1}, stirring speed: 500 rpm.

disappeared after 4 h and three new species formed at m/z=172.9, 156.0, 121.1 at 4 h. **Table 2.3** presents HPLC data of sampled MO solutions treated by the dispersed LNO (a) 0 h, (b) 4 h, and (c) standard chemical of N, N-dimethyl-p-phenylenediamine (DPD). Before reaction, only one peak at retention time=15.40 min is observed in the HPLC profile. During reaction, there are two major peaks appeared, at retention time 3.60 min and 4.80 min, respectively. Interestingly, in the HPLC profile of standard chemical DPD, there are two peaks at retention time=3.48 min, 4.98 min. This proves the intermediate during reaction has an almost identical retention time as DPD.

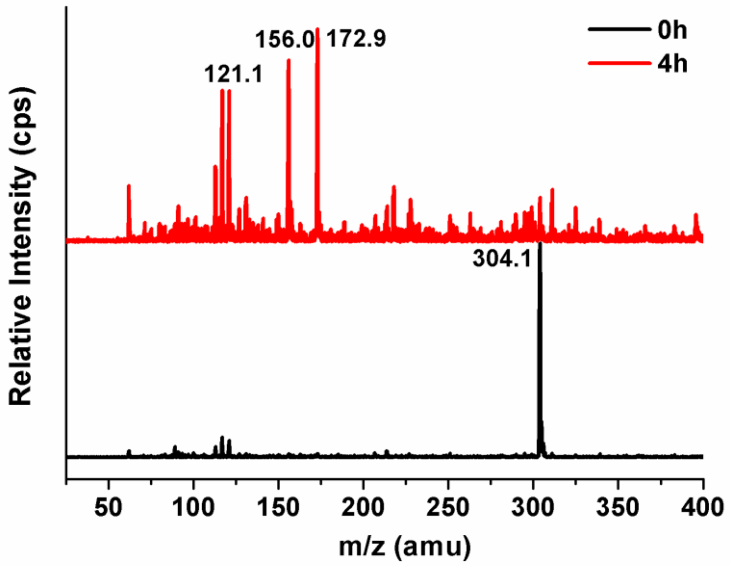

Figure 2.9 ESI/MS spectra of MO solution before reaction (0 h) and during reaction (4 h) under dark ambient condition.

2.3.3 Mechanism studies

To reveal the mechanism behind MO degradation with LNO under dark ambient conditions, the dye degradation reaction was carried out under N_2, O_2 and CO_2 conditions, respectively. No phase change is observed for LNO-after-N_2 or LNO-after-O_2. Lanthanum carbonate phase was observed for LNO-after-CO_2. MO is degraded even under N_2 conditions. Characteristic absorption peaks of MO decrease slowly during 6 h (**Figure 2.8b**). However, purging O_2 into aqueous solution does not improve but decreases the dye degradation rate (**Figure 2.8c**). By purging CO_2 alone to the reaction system (**Figure 2.8d**), there is a similar MO dye degradation trend with that under dark ambient conditions. While for commercial lanthanum carbonate ($La_2(CO_3)_3 \cdot xH_2O$, **Figure 2.10**), the MO concentration percentage is 87.6% after 6 h under dark ambient conditions. **Figure 2.8e** compares MO dye concentration percentage with time under N_2, O_2 and CO_2 with that under dark ambient conditions. After 6 h, the MO concentration percentages are 80.4%, 92.9%, 3.2% and 4.1%, respectively.

Table 2.3 HPLC data of MO solution treated with LNO and standard chemical of N,N-dimethyl-p-phenylenediamine (DPD).

Solution samples	Retention time (min)		
(a)0h	15.40		
(b) 4h	3.60	4.80	8.80
(c) N,N-dimethyl-p-phenylenediamine (DPD)	3.48	4.98	

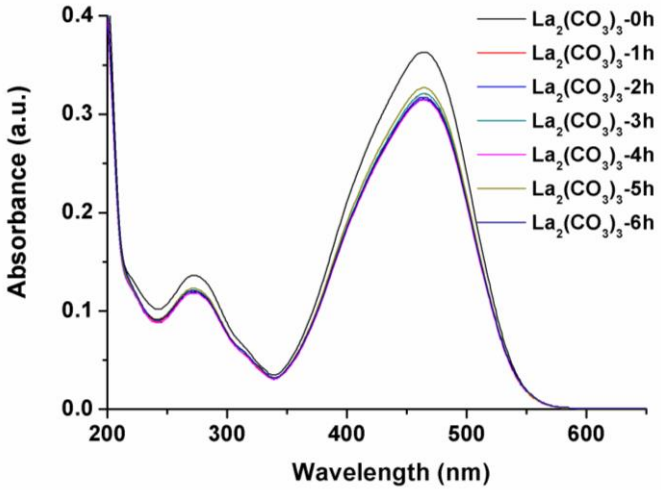

Figure 2.10 Sampled MO UV-vis spectra with commercial Lanthanum carbonate under ambient dark condition.

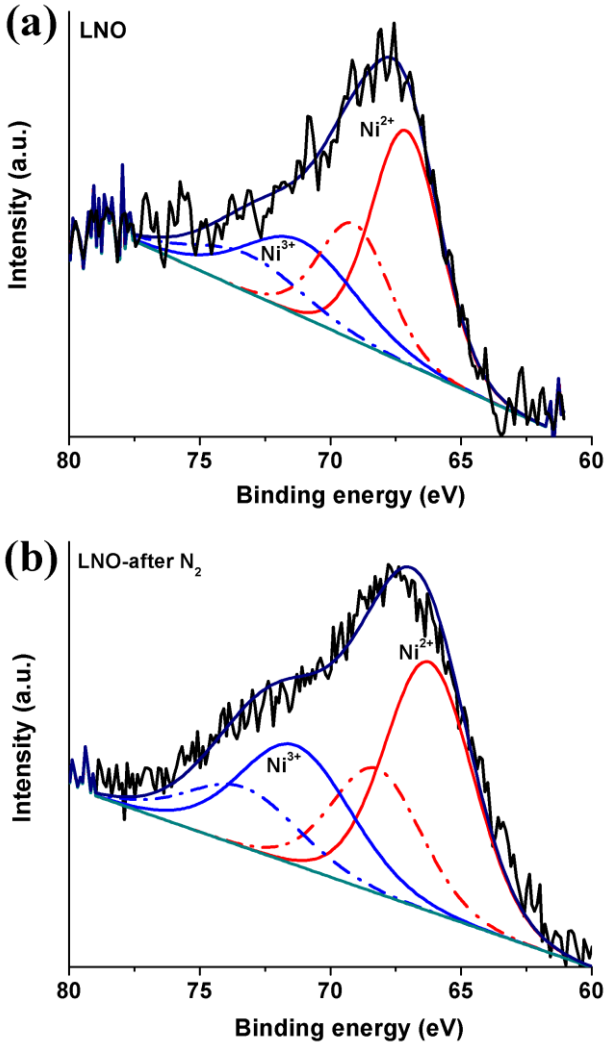

Figure 2.11 Experimental and deconvoluted Ni 3p XPS data[#] for (a) as-formed LNO and (b) LNO after reaction under N_2 conditions. #black lines: raw data; red lines: Ni^{2+} 3p3/2 (solid) and Ni^{2+} 3p1/2 (dashed) components; blue lines: Ni^{3+} 3p3/2 (solid) and Ni^{3+} 3p1/2.

A study of the LNO surface by XPS was carried out to detect the species involved in the reaction.[58] To understand the chemical state of nickel, the valence simulation curve of nickel is used to analyze the valence distribution. As shown in **Figure 2.11**, the line shapes of Ni 3p peak for LNO and LNO-after-N_2 are different, which also indicates different concentrations of Ni oxidation states. The peaks at 66 eV and 71 eV can be assigned to Ni^{2+} 3p3/2 and Ni^{3+} 3p3/2, respectively.[49,59] Based on fitting results, the Ni^{2+}/Ni^{3+} ratios can be obtained. For as-formed LNO, the ratio is 1.9:1; for LNO-after-N_2 is 1.7:1.

2.3.4 Solid Oxide Fuel Cell Performance Evaluations for Double Perovskite $PrBaCo_2O_5$

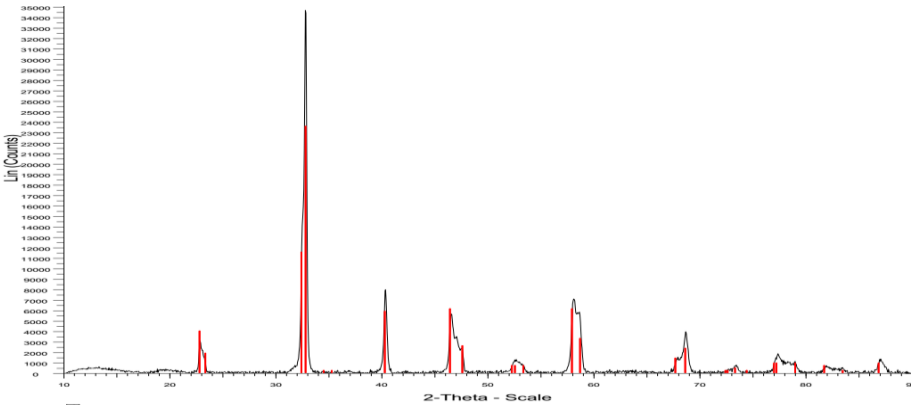

Figure 2.12 XRD pattern for double perovskite $PrBaCo_2O_5$ (PBC).

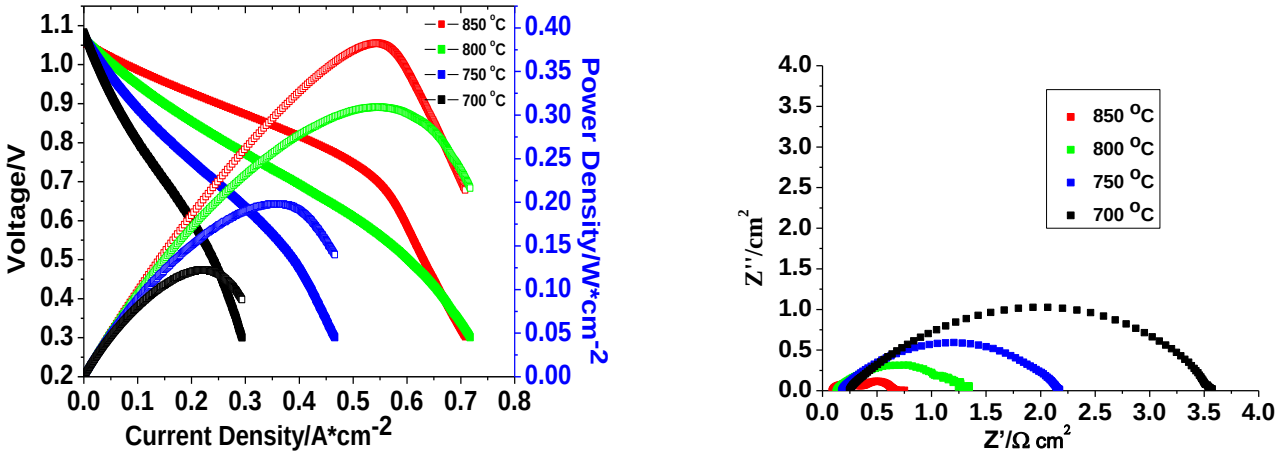

Figure 2.13 Solid oxide fuel cell performance for single cell with PBC as cathode.

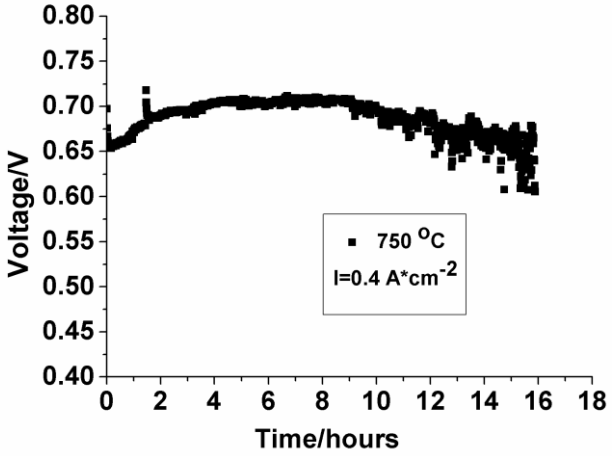

Figure 2.14 Stability test for single cell with PBC as cathode.

Double perovskite phase of $PrBaCo_2O_5$ (PBC) is formed (**Figure 2.12**). The fuel cell performance for PBC is not high enough due to its relatively large polarization resistance as shown in **Figure 2.13**, which can be improved by adding GDC to form composite cathode. The stability test (**Figure 2.14**) shows the cathode can be stable for 10 hrs.

2.4 Discussion

2.4.1 Changes to LNO-after-Ambient

The FTIR spectrum of LNO-after-ambient provides useful information of the existence of the CO_3^{2-} ion in this material. Bands at 1049, 850, 1471, and 748 cm^{-1} are assigned to ν_1, ν_2, ν_3 and ν_4 modes of CO_3^{2-} ion, respectively. Similarly with the work reported by Jeevanandam *et al*.,[60] the peak at 1373 cm^{-1} is attributed to the bending vibrational mode of H_2O. A broad band at ca. 3400 cm^{-1} is assigned to the stretching mode of hydroxyl groups of bound water molecules. Since La_2O_3 is reported to readily form carbonates or hydroxyl carbonates when exposed to atmospheric carbon dioxide under ordinary conditions,[61] it is reasonable to speculate this carbonate is lanthanum carbonate.

The peaks for the impurity phase in the XRD pattern of Error! Reference source not found. correspond ell to (101), (200), (210), (202), (311), (400) of (La, Ce) calkinsite (JCPDS card #06-0076).[62] After reaction, the lanthanum analog calkinsite (La2(CO3)3·4H2O) is formed while the main phase is still LNO. Calkinsite has a platy morphology, like that seen in the SEM image of LNO-after-ambient (**Figure 2.7 b**).

While the TGA of LNO-after-ambient shows a weight loss of 18%, there is no weight loss for pure LNO up to 900 ºC (**Figure 2.6a**). Weight loss in TGA under N_2 of LNO-after-ambient is interpreted as follows. The sample loses adsorbed and bound H_2O of ~15% from 25 ºC to 488 ºC (theoretical weight loss value of bound water from $La_2(CO_3)_3 \cdot 4H_2O$ is 14%), CO_2 is released at 767 ºC. Since CO_2 weight loss is ~3%, the carbonate amount is estimated approximately 10% in sample LNO-after-ambient.

2.4.2 Degradation Pathway and Intermediate Analysis

MO is generally considered to be very stable to light and difficult to oxidize.[38] Dark experiments under ambient condition prove that MO is not degraded without adding LNO (**Figure 2.15**). UV-vis spectroscopy was applied to determine the kinetics of MO decolorization, and the types and amounts of intermediate

products of the decomposition.[63] If the reaction is allowed to occur for more than 1 h, a pale yellow color is observed and new peaks are formed in the UV range, suggesting MO is indeed degraded, instead of just being absorbed by LNO with a small surface area. The absorption peak at ca. 464 nm corresponds to the azo bond due to the n-π* transition.[63] That peak in the UV-vis spectrum of MO decreases during reaction, which indicates that the azo bond of MO is broken down by LNO under ambient dark conditions. After 4 h, nearly all of the azo bonds of MO are broken down. Approximately 94.3% degradation efficiency is achieved after a 4 h reaction. The new absorption at about 244 nm appears simultaneously with azo bond cleavage indicating that there are newly produced compounds. This peak is attributed to the absorption from aromatic intermediates, which may originate from the two sides of the azo bond and/or their derivatives. Another characterization technique, ESI/MS, is needed to understand the degradation mechanism, as discussed later.

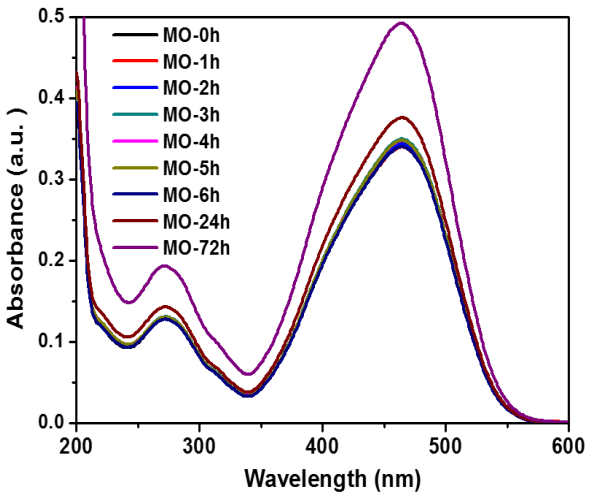

Figure 2.15 UV-vis spectra of MO aqueous solution without adding LNO[#].

#MO aqueous solution is stable without adding LNO. Absorbance of MO solution increase after 24 h, 72 h due to water evaporation.

In the negative mode ESI/MS spectrum of pure MO solutions, the peak at m/z=304.1 corresponds to the anion of MO ($[M-H]^-$). Before reaction, only one peak at m/z=304.1 is detected. During reaction, this peak

gradually disappears and the appearance of new peaks with m/z < 304.1 suggests that smaller fragments of dye are formed during the reaction. The peak at m/z=172.9 suggests the formation of sulfanilic acid anion after azo bond cleavage. The peak at m/z=156.0 is a radical anion due to deamination of sulfanilic acid anion caused by in-source collision induced dissociation in the mass spectrometer[64]. The peak at m/z=121.1 can be assigned to demethylation of DPD. The symmetric cleavage of azo bond was observed in previous reports before the destruction of the aromatic ring.[30,65,66]

Based on the observations of UV-vis spectra, ESI/MS and HPLC spectra, it is proposed that MO is cleaved symmetrically to form DPD and sulfanilic acid anion as the main intermediate. **Scheme 2.1** shows the possible pathway of MO decomposition. Sulfanilic acid are known metabolites in the breakdown of MO, and are nontoxic to experimental plants and bacteria.[65–67]

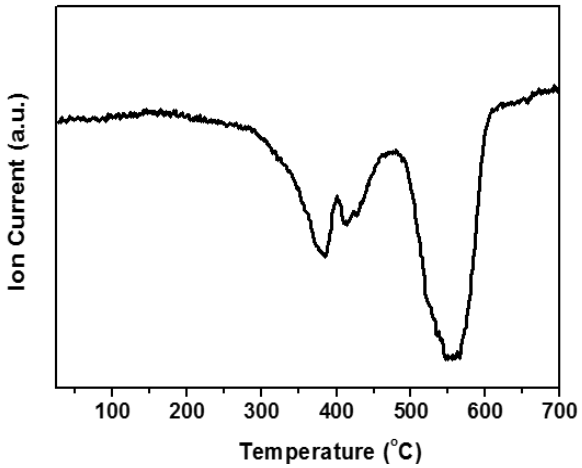

Figure 2.16 TPR profile of as-formed LNO[#].

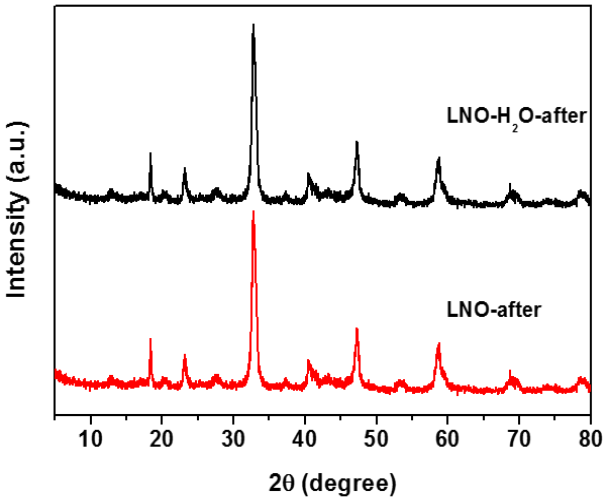

Figure 2.17 XRD Pattern of (lower) LNO after reaction and (upper) LNO after dissolved in DDW (distilled deionized water)[#]. # the difference between (lower) and (upper) is whether adding methyl orange or not.

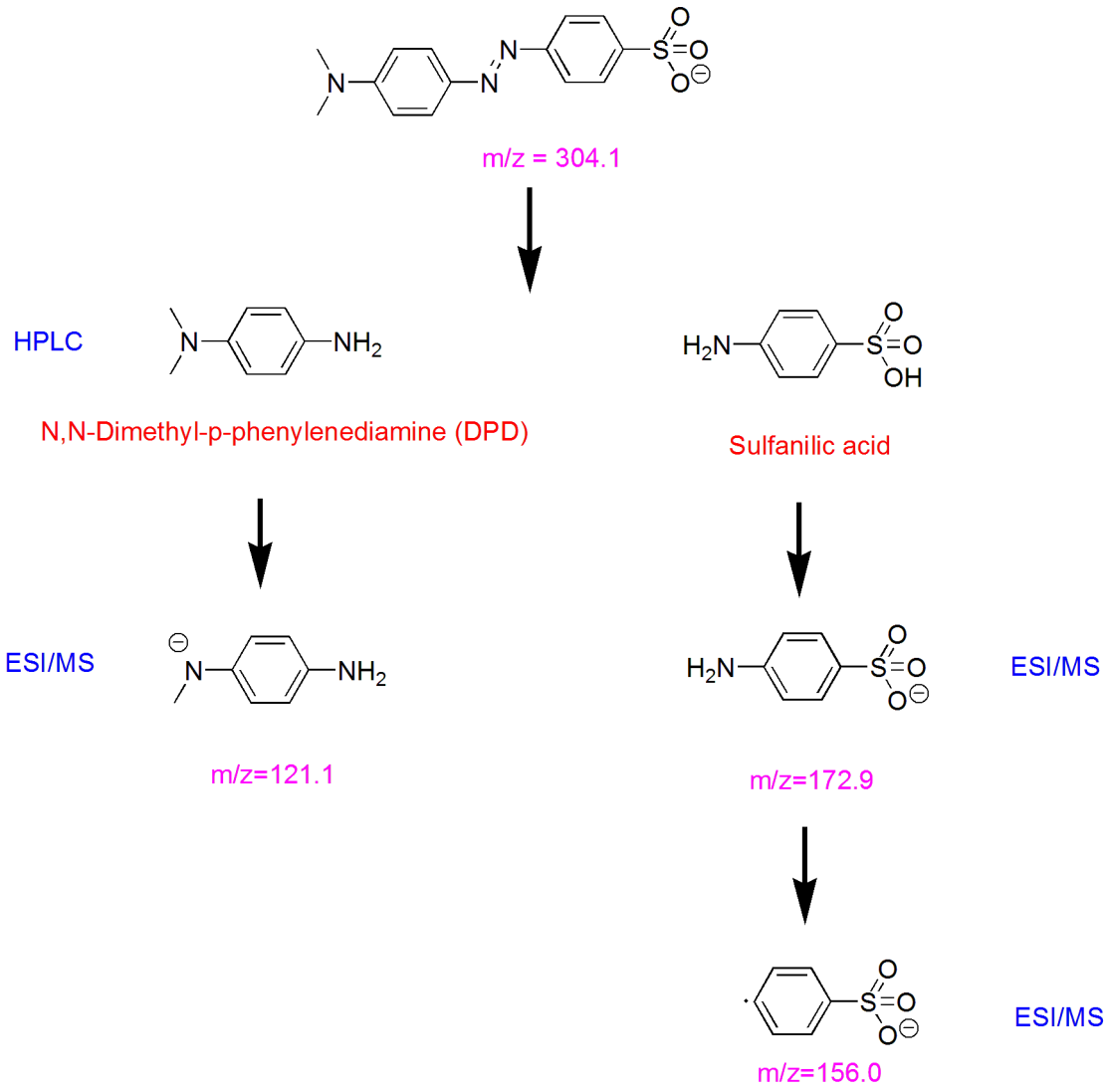

Scheme 2.1 Proposed structures of main intermediates of MO dye based on ESI/MS and HPLC experiments.

2.4.3 Mechanism Studies

When under N_2 conditions, MO is degraded at a relatively slow speed. The XPS analysis reflects the composition and chemical state of the surface of samples.[32] Since the Ni 2p 3/2 lines for both Ni^{2+} and Ni^{3+} are strongly overlapped with the La 3d 3/2 satellite line, it is not easy to determine the Ni^{2+}/Ni^{3+} ratio in a La-dominated region. Although the intensity of the Ni 3p peak is really weak compared to that of the Ni 2p 3/2 core-level peak, there is no interference with other peaks, thus the accuracy is improved.[49,68] Therefore,

Ni 3p core-level spectra are used here to distinguish Ni^{2+} and Ni^{3+}. According to XPS deconvolution results, nickel in LNO is partially oxidized from 2+ to 3+ after reaction under N_2. It is possible that methyl orange in aqueous solution serves as an electron acceptor, allowing this oxidation to happen at room temperature.[29] Besides oxidation of nickel, other factors must exist to promote MO degradation under dark ambient conditions.

In gas phase oxidation reactions, such as CO, propene, and isobutene oxidation, LNO is a very good oxygen adsorbent and adsorbed oxygen plays an important role in its excellent catalytic activity.[41] O_2 dissolved in water may also speed up the degradation reaction, since LNO may react with O_2 to generate ·OH radicals to attack the dye, as in a typical catalytic wet air oxidation process. At first, we considered dissolved oxygen as an important factor in this aqueous dye degradation reaction. However, purging O_2 for 6 h does not increase but decreases the MO degradation rate (**Figure 2.8c**). Therefore, the effect of O_2 dissolved in aqueous solution can be excluded here. To prove CO_2 gas has a promoting effect, CO_2 is purged during reaction. This procedure has a similar result with that under dark ambient conditions after 6 h. On the other hand, the high concentration of MO after 6 h for commercial lanthanum carbonate (**Figure 2.10**) proves that the degradation effect is not only coming from lanthanum carbonate.

The presence of carbonate on the LNO is important. The formation of lanthanum carbonate on the surface of LNO speeds up breaking down of the azo bonds. Under N_2 condition, nickel plays an important role; while under CO_2 conditions, carbonate promotes the degradation rate. Therefore, lanthanum carbonate and nickel work synergistically to degrade MO under dark ambient conditions. The good adsorption of MO on lanthanum carbonate could promote electron transfer between MO and nickel of LNO. Under N_2 or O_2 conditions, CO_2 is excluded and the adsorption of LNO is slow and small, so the degradation rate is slow during 6 h reaction.

2.5 Conclusions

In summary, a perovskite type material $LaNiO_{3-\delta}$ (LNO) was synthesized by a sol-gel citrate process and successfully employed in the non-photocatalytic degradation of the azo dye model compound methyl orange (MO) in aqueous solution. The degradation percentage of MO (5ppm) in aqueous solution over LNO was 94.3 % after 4 h without any light or chemical stimulants under ambient dark conditions. The degradation pathway of MO proceeds through azo bond cleavage to form the main intermediate, sulfanilic acid anion and DPD. Around 10% lanthanum carbonate (lanthanum-analog calkinsite) was observed after adding DDW. In addition, reactions under nitrogen, oxygen and carbon dioxide conditions were performed to understand the mechanism behind the dark degradation phenomenon. The MO degradation rate is much faster under ambient condition than that under nitrogen or oxygen. Further, nickel was confirmed to be oxidized by XPS on LNO after reaction under nitrogen. Carbon dioxide can promote MO degradation rate. Therefore, it is proposed that MO is treated by two synergic effects arising from nickel on LNO surfaces with the formation of lanthanum carbonate. This study discovers that LNO has a high degradation efficiency even under dark ambient conditions and unravel the mechanism by means of reactions under different gas conditions. Perovskite structure is maintained when CO_2 is excluded, which does not show as good degradation efficiency as the collapsed structure does.

Chapter 3. Modified Inverse Micelle Synthesis for Mesoporous Alumina with a High D4 Siloxane Adsorption Capacity and Arsenic Removal Efficiency

3.1 Introduction

Biogas (primarily methane and carbon dioxide) produced from anaerobic digestion of waste materials possesses considerable energy value. Traces of impurities in the biogas (e.g., sulfides, halides, and siloxane compounds) need to be removed before use.[69–75] Siloxane, one of the impurities, refers to a subgroup of silicones containing Si−O bonds with organic chains attached to the silicon atom.[69] During biogas combustion, siloxane, if not removed beforehand, can form abrasive microcrystalline silica particles which inhibit heat conduction and lubrication of the engine.[70,76,77] Current technologies for siloxane removal from biogas are mainly based on adsorption. Adsorbents cover a variety of materials such as activated carbons, zeolites, molecular sieves, or silica gels.[69,70,78] The most widely used adsorbents are activated carbons (ACs),[79] but regeneration of ACs is difficult due to the polymerization of adsorbed siloxanes on the AC surface.[69,73,80]

Mesoporous materials, especially MA, [81–85] are considered promising for siloxane adsorption because of their proper pore diameters,[69,82] and high surface areas. In our previous work, mesoporous aluminosilicates prepared by the same synthetic strategy showed improved adsorption performance with higher aluminum concentrations. As for mesoporous aluminosilicates, surface area and pore volume are two key factors that strongly influence the adsorption capacity of D4 siloxane.[86] Apart from the goal of high pore volumes, pore size is another particularly significant textural property to consider. Porous materials with continuously adjustable pore sizes have attracted great interest in a variety of applications such as molecular sieves, selective adsorption, and size-selective catalysis.[7,87] All of these have led us to develop MA materials with adjustable pore sizes and high pore volumes.

Different synthetic methods have been employed for preparing MA, such as an aerosol generation method using block copolymers, a modified sol-gel method with organic templates, and an evaporation-induced self-assembly (EISA).[88,89] However, these common synthetic pathways are all deduced from the synthesis methods of mesoporous silica yielding unsatisfactory alumina materials.[7] Examples of the unadjustable pore size MAs synthesized by the currently available methods can be found from Vaudry *et al.,* who reported MA materials with a narrow pore size distribution prepared by anionic surfactants (carboxylic acids),[4] and Kim *et al,,* who synthesized MAs of identical pore size (4 nm) irrespective of the variation of surfactant/aluminum precursor ratio.[90]

The main contribution of this research is to explore controllable MA synthesis. As shown in **Table 3.1**, water content is critical during the synthesis. Therefore the reagent to water ratio has to be strictly controlled.[91] Our synthetic strategy includes a non-polar solvent in order to minimize the effects of water and create a fast evaporation process. This strategy has been successfully used for preparing different mesoporous transition metal oxides, such as manganese oxide,[92,93] cobalt oxide,[94] titanium oxide,[22,95] and iron oxide,[96,97] which displayed superior performances in different applications. However, this is the first time this synthetic strategy has been used for the preparation of MA (**Table 3.1**). The synthesis parameters have been modified to develop this synthetic strategy further. It is important and significant to learn more about this synthetic strategy through this study, which may be applied to other mesoporous systems. Reaction times, surfactant chain lengths and calcination temperatures , which are commonly used for adjusting pore sizes,[7,98–100] were chosen as parameters for adjusting textural properties (pore sizes, surface areas, and pore volumes) of alumina. The synthesized MAs have been demonstrated to have a great D4 siloxane adsorption capacity, compared with commercially activated alumina. Some insights to correlate synthesis parameters with the material textural properties and adsorption performance are also involved in this study.

Table 3.1 Synthesis parameters and textural properties of MA in the literature.

Surfactant	Precursor/ Solvent	Water	Reaction time	Pore morph-ology	Surface areas (m^2/g)	Pore size adjustable	Authors [Ref.]
Anionic (carboxylic acid)	Aluminum Sec-butoxide /Alcohol	Yes	Aged 24h, heated at 383 K for 2 days	Randomly ordered	710	No 2 nm	F. Vaudry, Mark E. Davis, *et al.* [4]
Non-ionic (containing polyethylene oxide)	Tri-sec-butoxyaluminum /Sec-butyl alcohol	Yes	19 h	Wormhole	420-535	Yes 2.4-4.7 nm	Stephen A. Bagshaw and Thomas J.Pinnavaia [3]
Non-ionic (containing polyethylene oxide)	Aluminium sec-butoxide /Sec-butanol	Yes	40 h	Wormhole	Pure alumina: 267-391	Yes 5-5.5 nm	Wenzhong Zhang and Thomas J.Pinnavaia [101]
Cationic (cetyltrimethylammonium bromide)	Aluminium sec-butoxide /TEA (triethanolamine)	Yes	Aged 72 h	Wormhole	250-340	Yes 3.3-6 nm	S. Cabrera, Marcos, M., Pedro Amorôs, *et al.* [7]
Stearic acid	$Al(sec\text{-}BuO)_3$ /Sec-butyl alcohol	Yes	24 h	Wormhole	316-380	No 4 nm	P.Kim, Jongheop Yi, *et al.* [90]
Carboxylic acid with TEA	Aluminum nitrate /Water	Yes	Stir 12 h, Aged for 24 h at 90°C	Wormhole	214- 376	Yes 3.3 -6.5 nm	B.Naik, N.N. Ghosh, *et al.* [102]
Non-ionic (containing polyethylene oxide)	Alumium sec-butoxide /1-butanol	No	4-8 h	Wormhole	56 -314[a]	Yes 3.1-5.4 nm	This Work

[a] Higher calcination temperature or longer hold time for samples with a reaction time of 8 h may result in higher surface area according to Table 1 in the main text.

Arsenic is classified as a carcinogen by U.S. EPA, which is usually in the form of inorganic oxyanions. [87] The maximum contaminant level of arsenic in drinking water is 0.01ppm. Arsenate, the valence state of As (V), is more toxic than arsenate with As (III). Efficient removal of arsenic from drinking water is highly required to meet the maximum contaminant level. There are several methods for arsenic treatment, for example, precipitation, ion exchange, adsorption, and membrane filtration. Among the treatment methods, adsorption is less expensive, safer and easier for operation. The requirement for adsorbents is uniform and accessible pores, a high surface area, and stability. [87] Therefore it is interesting to investigate the arsenic treatment efficiency of mesoporous alumina as a possible adsorbent.

3.2 Experimental

3.2.1 Synthesis of MA

All chemicals were used as received without further purification. During the synthesis, 5 g aluminum sec-butoxide (Alfa-Aesar) was diluted in 10 g 1-butanol (Sigma-Aldrich) with stirring at ambient temperature. Then 2 g Pluronic P123 (Poly (ethylene glycol)-block-Poly(propylene glycol)-block-Poly(ethylene glycol); PEO_{20}-PPO_{70}-PEO_{20}; Sigma-Aldrich) was added. At the same time, 2 g nitric acid (J.T.Baker) was dissolved in 10 g 1-butanol. The two solutions were reacting at 120 ^{o}C for 6 h, yielding a transparent gel. The gel was washed several times with ethanol to remove surfactants and dried in a vacuum oven at room temperature overnight. Different reaction times of 4-8 h were studied at 120 ^{o}C with P123 as the surfactant. The obtained powders, after grinding, were placed in a cuvette and calcined in air at 450-600 ^{o}C for 1-4 h, with a 2 ^{o}C min^{-1} heating rate. To explore the effect of surfactant chain lengths, 0.2 g Brij56 ($C_{16}H_{33}(PEO)_{10}OH$; Sigma-Aldrich), and 4.3 g F127 ($PEO_{106}PPO_{70}PEO_{106}$; Sigma-Aldrich) were also investigated. Surfactant F127 has a longer chain length of PEO block than that of P123. Compared to the Pluronic triblock copolymers, Brij56 surfactant is a much shorter diblock polymer composed of a hydrophilic PEO block and $C_{16}H_{33}$ alkyl chains. The obtained powders were calcined in air at 500 ^{o}C for 1 h, at a 2 ^{o}C min^{-1} heating rate. The synthesis parameters for different samples are recorded in **Table 3.3**.

Table 3.2 Chemical properties of different surfactants.

Surfactants	Formulas	Molecular weights (g/mol)	Supplier
Brij 56	C_{16} $(EO)_{10}$	682	Sigma-Aldrich
Pluronic P123	$(EO)_{20}(PO)_{70}(EO)_{20}$	5800	Sigma-Aldrich
Pluronic F127	$(EO)_{106}(PO)_{70}(EO)_{106}$	12600	Sigma-Aldrich

Table 3.3 Synthesis parameters for different samples.

Sample	Reaction time	Surfactant	Calcination temperature	Calcination hold time
Al120-4h	4 h	P123	500 ^{o}C	1 h
Al120-6h	6 h	P123	500 ^{o}C	1 h
Al120-8h	8 h	P123	500 ^{o}C	1 h
Al-Brij56	6 h	Brij56	500 ^{o}C	1 h
Al-P123	6 h	P123	500 ^{o}C	1 h
Al-F127	6 h	F127	500 ^{o}C	1 h
Al500-1h	6 h	P123	500 ^{o}C	1 h
Al500-2h	6 h	P123	500 ^{o}C	2 h
Al500-4h	6 h	P123	500 ^{o}C	4 h
Al450-1h	6 h	P123	450 ^{o}C	1 h
Al600-1h	6 h	P123	600 ^{o}C	1 h

3.2.2 Characterization

X-ray diffraction (XRD) analyses were performed in a Rigaku Ultima IV diffractometer (Cu Kα radiation, λ=1.5406 Å) with an operating voltage of 40 kV and a current of 44 mA. The low angle PXRD patterns were collected over a 2-theta range of 0.5-10° with a continuous scan rate of 0.5° min^{-1}. The wide angle PXRD patterns were collected over a 2-theta range of 10-80° with a

continuous scan rate of 2.0° min^{-1}. Nitrogen sorption experiments were conducted in a Quantachrome Autosorb-1-1C automated adsorption system. The powders were degassed for 6 h at 150 ^{o}C. Surface areas were calculated using the Brunauer-Emmett-Teller (BET) method. Pore size distributions and pore volumes were calculated using the Barrett-Joyner-Halenda (BJH) method from the desorption isotherm. Morphological characterization was done using an FEI Teneo LoVac FEG-SEM. Transmission electron microscopy (TEM) images of synthesized mesoporous materials were recorded on a JEOL 2010 FasTEM microscope operated at 200 kV. CO_2 temperature-programmed desorption (TPD) was conducted using a Netzsch TG 209 F1 Libra thermogravimetric analyzer coupled to a QMS 403C quadrupole mass spectrometer. The samples were pretreated at 200 ^{o}C for 1 h to clean the sample surface before each test. CO_2 adsorption was performed at 27 ^{o}C with 50 cm^3/min 5% CO_2 balanced in Ar for 1 h. Physisorbed CO_2 was removed by flowing argon for 30 min. After that, the samples were heated from 27 ^{o}C to 900 ^{o}C under 15 ^{o}C/min in argon. Pyridine adsorption studies were performed with 13 mm diameter self-supporting pellets using a Nicolet Magna 560 FTIR. The pellets were cleaned at 250 °C overnight. A 1 M pyridine solution in methanol was dropped on pellets, and physisorbed pyridine was removed at 200 °C for 90 min. The spent adsorbent Al120-8h after the first run was analyzed using a Bruker Avance III 400 MHz solid state magic-angle spinning nuclear magnetic resonance (MAS NMR) spectroscopy, and a PHI model 590 X-ray photoelectron spectroscopy (XPS).

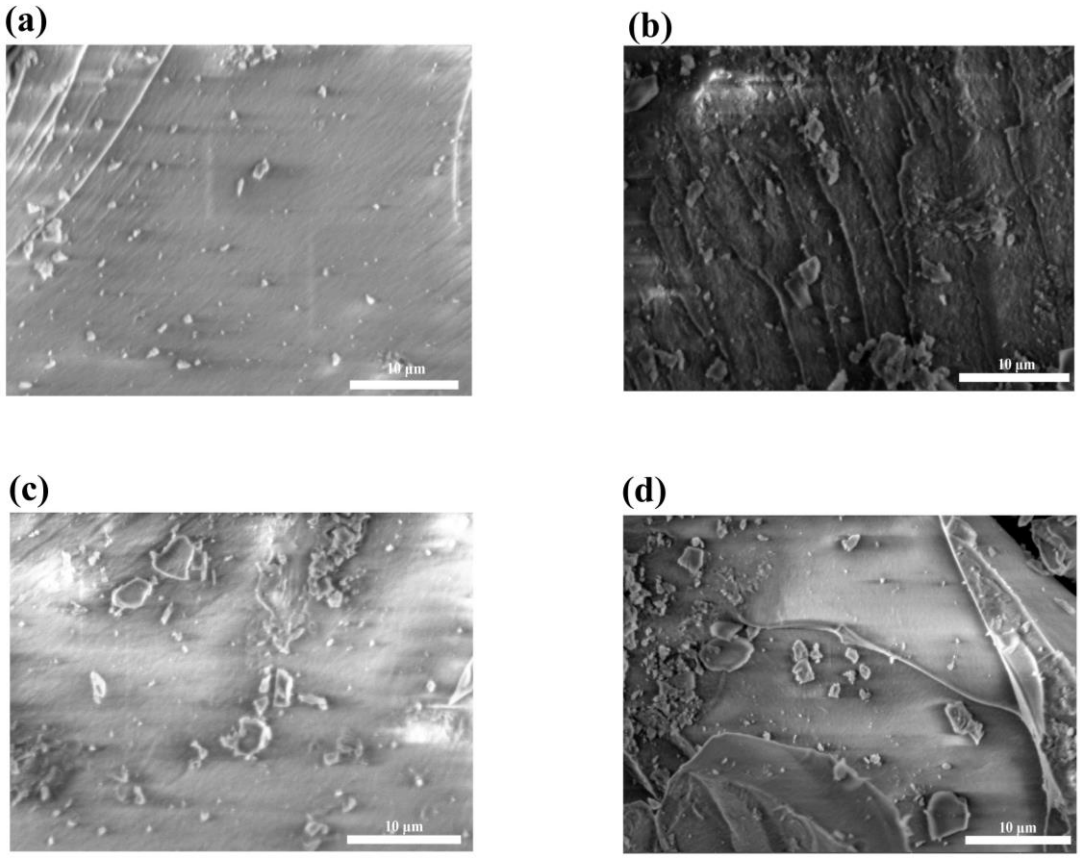

Figure 3.1 SEM images of as-prepared mesoporous alumina (a) Al120-8h; (b) Al-F127; (c) Al600-1h; (d) Al500-4h.

3.2.3 D4 Siloxane Adsorption

Each D4 siloxane (Sigma-Aldrich) adsorption test was performed over 100 mg of adsorbent material at room temperature and atmospheric pressure in a tubular quartz reactor (15 cm long, 0.6 cm internal diameter). D4 siloxane was introduced with a 15 mL/min N_2 carrier gas flow. The D4 siloxane amount in the carrier gas was approximately 6.4 mg/60 min. After passing through the adsorbents, a gas wash bottle filled with 200 mL hexane (Sigma-Aldrich) was used to trap the residual siloxane in the carrier gas. The D4 siloxane concentration in the solvent trap was sampled every 20 min and measured in an Agilent gas chromatography/ mass selective detector (GC/MSD) system (GC 7820A and MSD 5975) equipped with an HP-1 capillary column (12 m × 200 µm × 0.33 µm). Calibration was carried out using D4 siloxane standards.

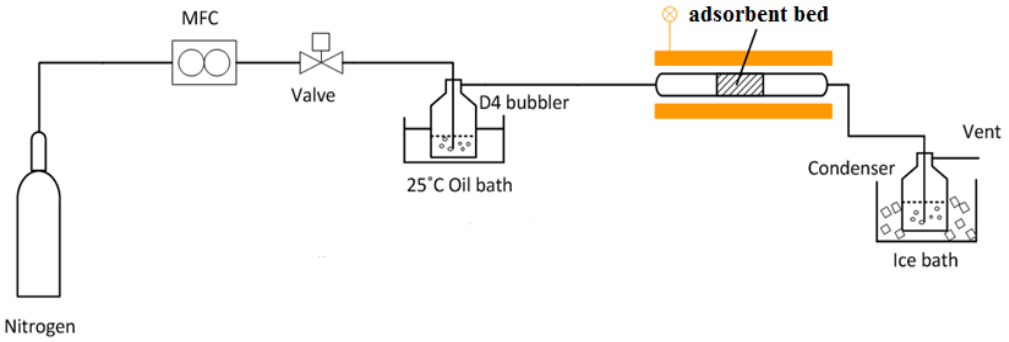

Figure 3.2 Schematic diagram of set-up for D4 siloxane adsorption test.

Breakthrough time was identified from adsorbent breakthrough curves, and then breakthrough capacity was obtained from the corresponding saturation curve. The saturation curve was obtained by subtraction of the adsorbent breakthrough curve from the blank breakthrough curve (tested with no adsorbents), which presented the D4 amount adsorbed. Saturation capacity is the maximum adsorption capacity. The spent adsorbent was recovered after the adsorption tests, mixed with 50 mL of hexane, and centrifuged after sonication to extract the adsorbed siloxane from the adsorbent. The extract was then analyzed in the GC/MSD system to obtain the wash capacity of the adsorbents, which was identical to its saturation capacity. The adsorbent after extraction was dried at 100 ^{o}C overnight and tested again for evaluation of its stability.

3.3 Results

3.3.1 Modification of MA Pore Size by Adjusting the Reaction Time and Surfactant

All the MA materials in **Figure 3.3a** show one broad XRD line in the low angle region, and the wall thicknesses are calculated accordingly (**Table 3.4**). There is only one peak in the low angle XRD range, indicating a nano-sized periodicity and uniform mesoporosity.[12,103] The peak positions are 9.3 nm, 11.8 nm, and 14.7 nm with reaction times at 4 h, 6 h, and 8 h, respectively, which

indicates the pore size increases with reaction time. The peak positions are 9.8 nm, 11.8 nm, and 14.7 nm with

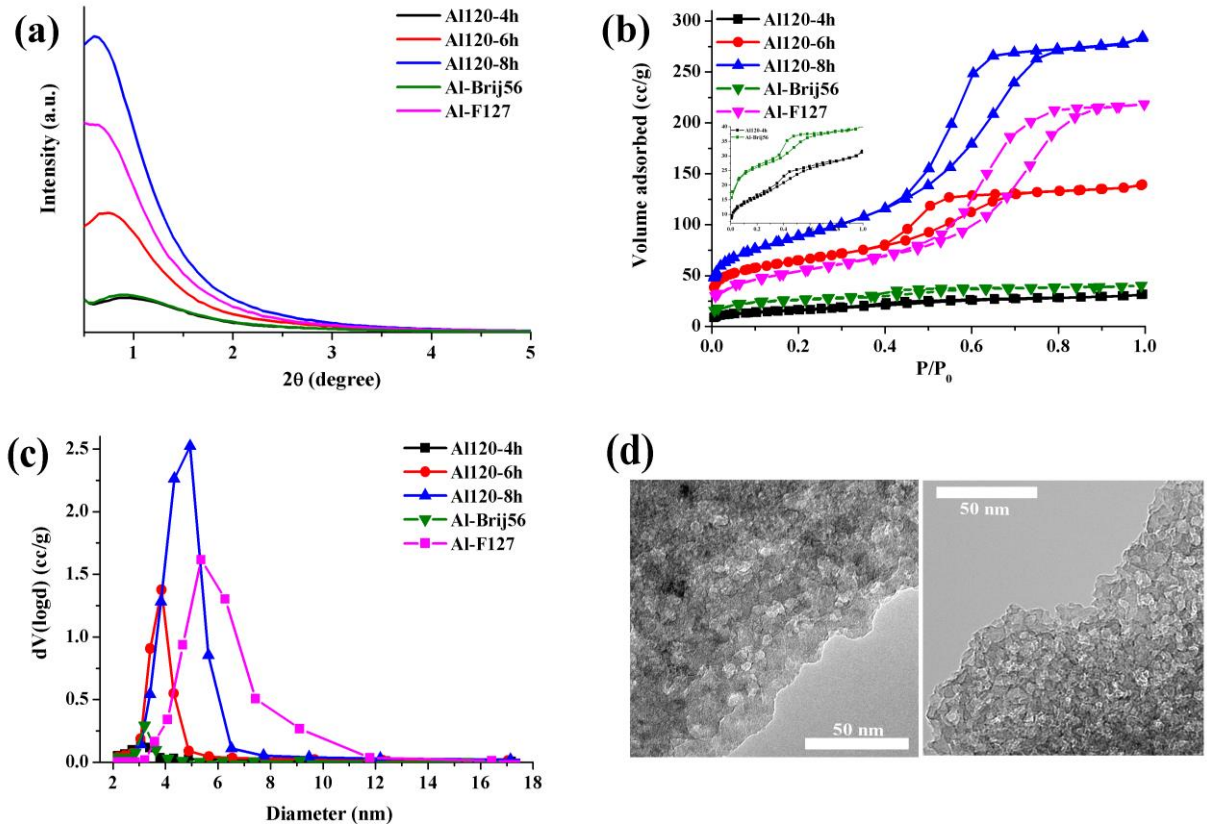

Figure 3.3 (a) Low angle XRD patterns (b) N_2 sorption isotherm curves (inset: isotherm curves of Al120-4h, Al-Brij56) and (c) pore size distributions of mesoporous alumina samples Al120-4h, Al120-6h, Al120-8h, Al-Brij56 and Al-F127. (d) TEM images of representative samples Al120-6h and Al120-8h.

surfactants of Brij56, P123, and F127, respectively, which indicates that the pore size increases with the chain lengths of the surfactants. The wide angle XRD patterns of these samples (**Figure 3.4**) after subsequent thermal treatment up to 900 ^{o}C for 1 h (**Figure 3.5**).

.

Table 3.4 Textural properties of mesoporous alumina of different reaction times, surfactants and calcination temperature and hold time.

[a]Not available. [b]Calculation is according to Bragg's law. [c]Wall thickness δ=(d-D)/2.

Sample	Surface area (SA, m^2/g)	Pore diameter (D, nm)	Pore volume (V, cc/g)	Low-angle XRD peak position (d, nm)[b]	Wall thickness (δ, nm)[c]
Al120-4h	56	3.1	0.05	9.3	3.1
Al120-6h	223	3.8	0.20	11.8	4
Al120-8h	314	4.3	0.46	14.7	5.2
Al-Brij56	83	3.2	0.06	9.8	3.3
Al-P123	223	3.8	0.20	11.8	4
Al-F127	190	5.4	0.36	14.7	4.7
Al500-1h	223	3.8	0.20	11.8	4
Al500-2h	283	3.9	0.24	8.8	2.5
Al500-4h	293	3.8	0.28	9.8	3
Al450-1h	85	3.4	0.09	10.4	3.5
Al600-1h	298	3.4	0.30	11.0	3.8
Commercially activated alumina	201	3.4	0.26	NA[a]	NA[a]

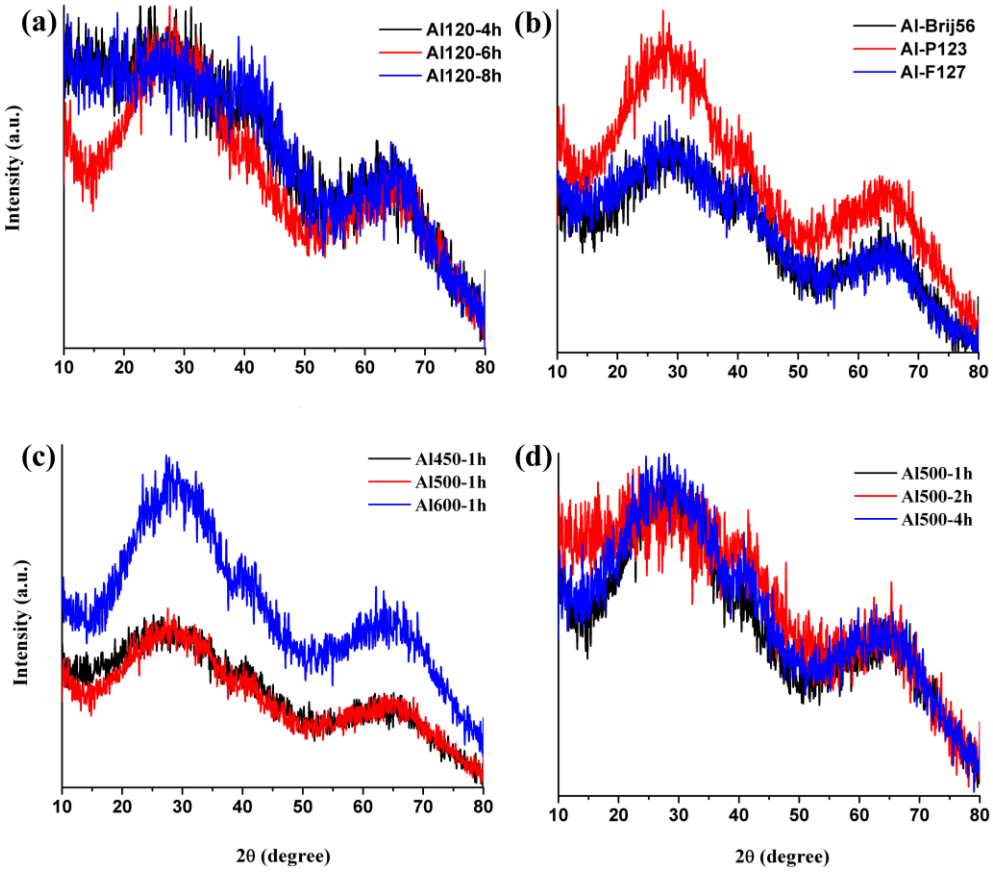

Figure 3.4 Wide angle X-ray diffraction patterns of mesoporous alumina (a) Al120-4h, Al120-6h and Al120-8h; (b) Al-Brij56, Al-P123 and Al-F127; (c) Al450-1h, Al500-1h and Al600-1h; (d) Al500-1h, Al500-2h and Al500-4h.

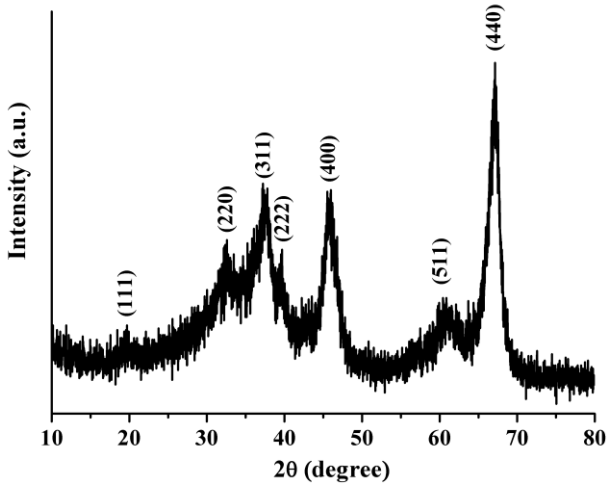

Figure 3.5 Wide angle X-ray diffraction patterns of mesoporous alumina Al120-8h-900 (as-formed Al120-8h sample calcined at 900 ^{o}C for 1h).

Mesoporosity of the alumina is further illustrated by the N_2 adsorption/desorption isotherms and BJH desorption pore size distributions (**Figure 3.3b, c**). All alumina samples show a similar well-defined step in the adsorption isotherm (Type IV isotherm), indicating a regular mesoporous structure,[98] and a hysteresis in the desorption isotherm over the same relative pressure range (H1 hysteresis loop), suggesting the formation of cylindrical pores.[103] **Figure 3.3b**shows that the capillary condensation steps for samples Al120-4h, Al120-6h, and Al120-8h shift slightly to greater relative pressures, indicating an increase in the size of mesopores with the increasing reaction time. The similar trend was also observed for samples Al-Brij56, Al-P123 (Al120-6h), and Al-F127, indicating an increase in the mesopore size with the chain lengths of the surfactants. In **Figure 3.3c**, the pore diameter of the mesoporous Al120-4h, Al120-6h, and Al120-8h is observed to increase with reaction time. The pore diameter of mesoporous Al-F127 is larger than that of Al-P123, while the pore size of Al-Brij 56 is the smallest among the three samples with different surfactants as the variable parameter (**Figure 3.3c**). The TEM images of the representative samples Al120-6h and

Al120-8h (**Figure 3.3d**) show that no apparent order in the pore arrangement exists, which is in good agreement with low angle XRD patterns. The pore packing motif can be described as "wormhole-like".[3,7] Though regular in average diameter, the wormhole-like channels have no long-range order. That is, the channels appear to be packed randomly. The low angle XRD line may result from the regular separation between single channel walls.[3] The pore size is improved with the reaction time increasing from 6 h to 8 h.

3.3.2 Modification of MA Surface Area and Pore Volume by Adjusting the Calcination Temperature and Hold Time

Mesoporosity is maintained at different calcination temperatures and hold times as shown in low angle XRD patterns (**Figure 3.6a**). The resulting MA materials all have low crystallinity

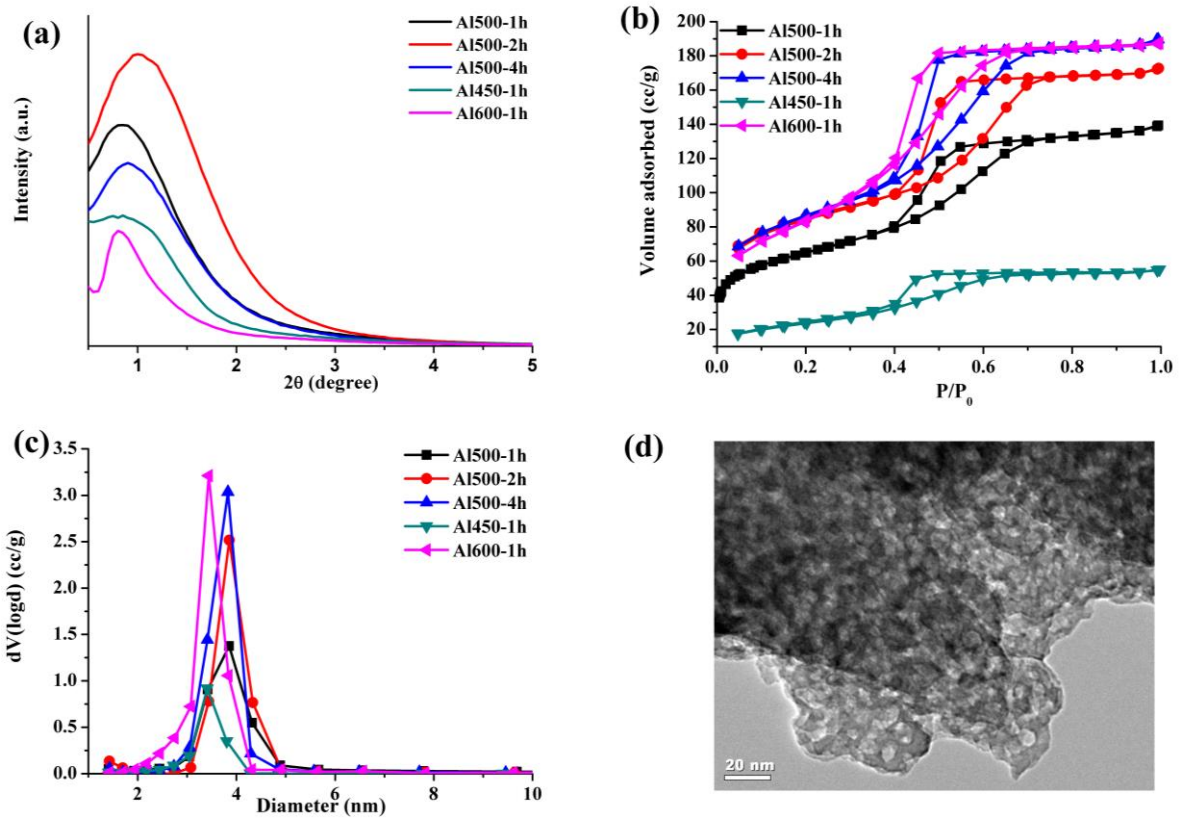

Figure 3.6 (a) Low angle X-ray diffraction patterns, (b) N_2 sorption isotherm curves and (c) pore size distributions of mesoporous alumina samples Al500-1h, Al500-2h, Al500-4h, Al450-1h and Al600-1h. (d) Transmission electron microscopy (TEM) image of Al500-1h.

(**Figure 3.4**). All of the as-prepared samples show mesoporous characteristic Type IV isotherms and monomodal pore size distributions regardless of the calcination temperature or hold time(**Figure 3.6b,c**). As shown in **Table 3.4**, the surface area and pore volume increase when the calcination temperature is increased from 450 ^{o}C to 600 ^{o}C, whereas the pore size does not have an obvious change with an increasing calcination temperature. The surface area and pore volume also increase with an increase of calcination hold time, though the hold time has no obvious effect on the pore size of MA. All of these results signify that a good control of surface area and pore volume of MA is achieved by tuning the heat treatment parameters. The high resolution TEM image (**Figure3.6d**) of Al500-1h (Al120-8h) shows a highly interconnected pore system.

3.3.3 D4 Siloxane Adsorption

With regard to pore volumes, reaction time is an important factor in the synthesis method, so Al120-6h and Al120-8h were chosen for D4 siloxane adsorption tests. Commercially activated alumina is the most well-known alumina sample for adsorption or catalysis. **Figure 3.7** shows a comparison of D4 siloxane adsorption tests of the as-synthesized samples (Al120-6h and Al120-8h) and commercially activated alumina. As revealed from the D4 breakthrough curve in **Figure 3.7a**,

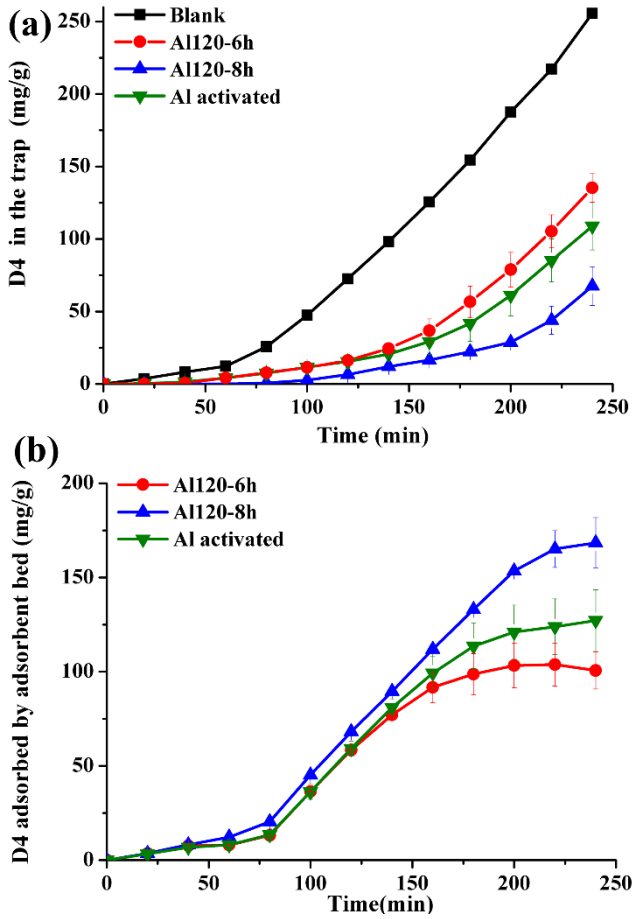

Figure 3.7 (a) Breakthrough curves obtained by plotting accumulated D4 siloxane in the hexane trap versus time. (b) Saturation curves obtained by plotting adsorbed D4 siloxane on adsorbents Al120-6h, Al120-8h, and commercially activated alumina.

D4 does not break through with Al120-8h until 100 min (breakthrough capacity: ~45 mg/g). However, commercially activated alumina and Al120-6h have breakthroughs at approximately 60 min (breakthrough capacity: ~8 mg/g). That means Al120-8h has approximate 5.6 times greater breakthrough capacity than commercially activated alumina. According to the D4 saturation curve (**Figure 3.7b**), the saturation capacity of commercially activated alumina is 127 mg/g. For Al120-8h, the saturation capacity is 168 mg/g, indicating an improvement of 32% compared to that of commercially activated alumina. Surface areas and pore volumes of commercially activated alumina are also recorded in **Table 3.4** (N_2 sorption related measurements are shown in **Figure 3.8**).

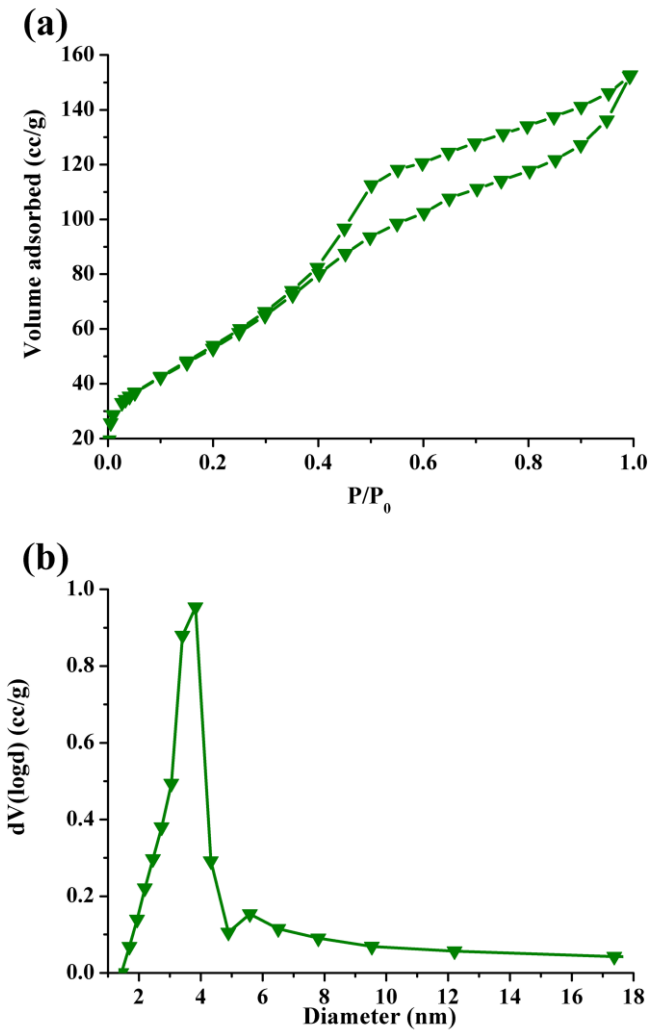

Figure 3.8 (a) N_2 sorption isotherm curve, and (b) pore size distribution of commercial activated alumina.

3.3.4 Adsorbent Regeneration

MA Al120-8h can be easily regenerated. The wash capacities of the adsorbents from the first (1st) to third (3rd) recycle are 162, 148, 143 mg/g, respectively, which maintains 96%, 88%, and 85% capacity of the fresh adsorbent (**Figure 3.9a**) . Wide scan XPS data (**Figure 3.9b**) reveal an atomic ratio of Si/Al ~0.4 on the surface of the spent Al120-8h after one run. In contrast, the most widely used adsorbent activated carbons (ACs) are not easily recovered even at higher temperatures (250-300 ^{o}C) for a longer period of time,[104] which is an effect related to the polymerization of D4

on the surface of ACs due to the phenolic and carboxylic groups on their surfaces. A 96% capacity can be maintained for the first recycle of Al120-8h, indicating that a polymerization phenomenon is not evident after one D4 siloxane adsorption run. This can be further verified by ^{29}Si MAS NMR (**Figure 3.9c**) and ATR (**Figure 3.9d**) measurements on spent Al120-8h after one run.

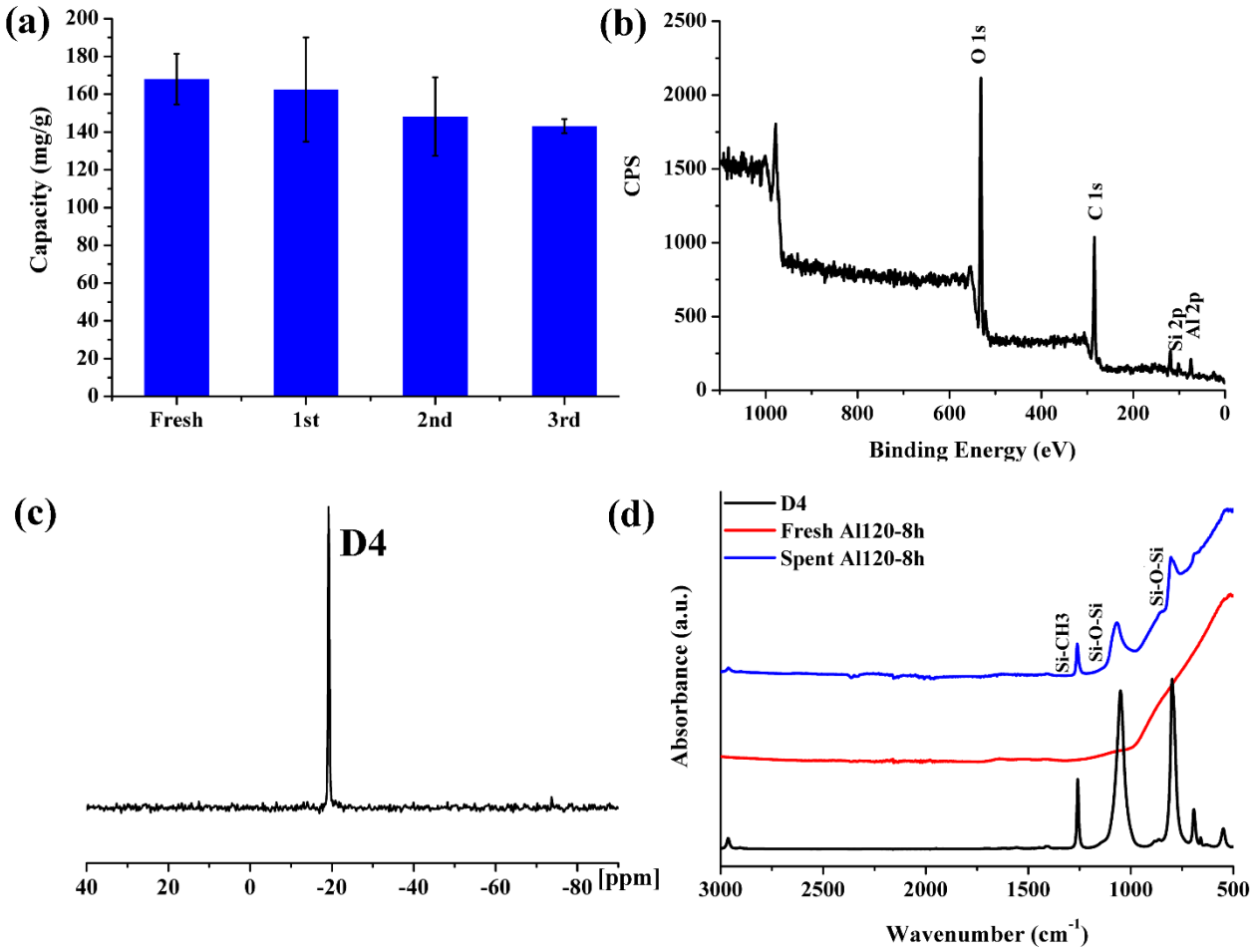

Figure 3.9 (a) Wash capacities of regenerated adsorbent Al120-8h. (b) XPS of full-range spectrum, and (c) ^{29}Si MAS NMR spectrum for spent adsorbent Al120-8h after one run. (d) ATR spectra of D4, fresh and spent Al120-8h after one run.

Since only one peak at δ= -19 is observed in the ^{29}Si MAS NMR spectrum for spent Al120-8h after one run (**Figure 3.9c**), NMR peaks for other siloxanes are not observed, which indicates that there is no obvious polymerization on the Al120-8h adsorbent.[105] The ATR spectrum of spent Al120-8h recorded after one D4 siloxane adsorption run is compared with the spectra of the fresh adsorbent and D4 (**Figure 3.9d**). Bands at wavenumbers of 1255, 1062, and 804 cm^{-1} are detected

for spent Al120-8h, which are ascribed to the Si–CH_3 bonds, the asymmetric, and the symmetric stretches of the Si–O–Si bridge bonds of D4 siloxane, respectively.[104] There are no other bands, and no polymerization for Al120-8h after one run is observed.[106] After recycling three times, there is excellent stability of the adsorbents as compared to significant reported losses of capacity for activated carbons and silica gel.[69,106,107]

3.3.5 Arsenic Adsorption Evaluation

Table 3.5 Arsenic uptake capacity summary for different samples.[#]

Samples	As (V) uptake capacity (mg/g)	Notes and References
Yoldas' alumina	34	SA= 300 m^2/g[87]
Activated alumina	~16	SA= 370 m^2/g[87]
Mesoporous alumina	121	SA=307 m^2/g, PV=0.39 cc/g[87]
MCM-41	110	SA= 481 m^2/g; [108] aminosilane-grafted mesoporous silica
SBA-1	260	SA= 126 m^2/g; [108] aminosilane-grafted mesoporous silica
Al120-4h	240	SA= 56 m^2/g, PV= 0.05 cc/g (This work)
Al120-6h	244	SA=223 m^2/g, PV=0.2 cc/g (This work)
Al120-8h	255	SA= 314 m^2/g, PV=0.5 cc/g (This work)

The arsenic adsorption evaluation conditions: 30 mg Al120-8h, 30 ml 200 ppm As (V) solution, shaking for 15 h. Averaged from 3 runs.

As shown in **Table 3.5**, uptake capacity has linear relationship with pore volume in this work. In agreement with the literature,[87] the most critical factor of mesoporous alumina for arsenic adsorption is a regular pore structure(interlinked pore system preferred), and pore volume is also a controlling factor (when surface area is the same).[87] Besides, no post-treatment (such as functionalization) is needed as compared with mesoporous silica.[108]

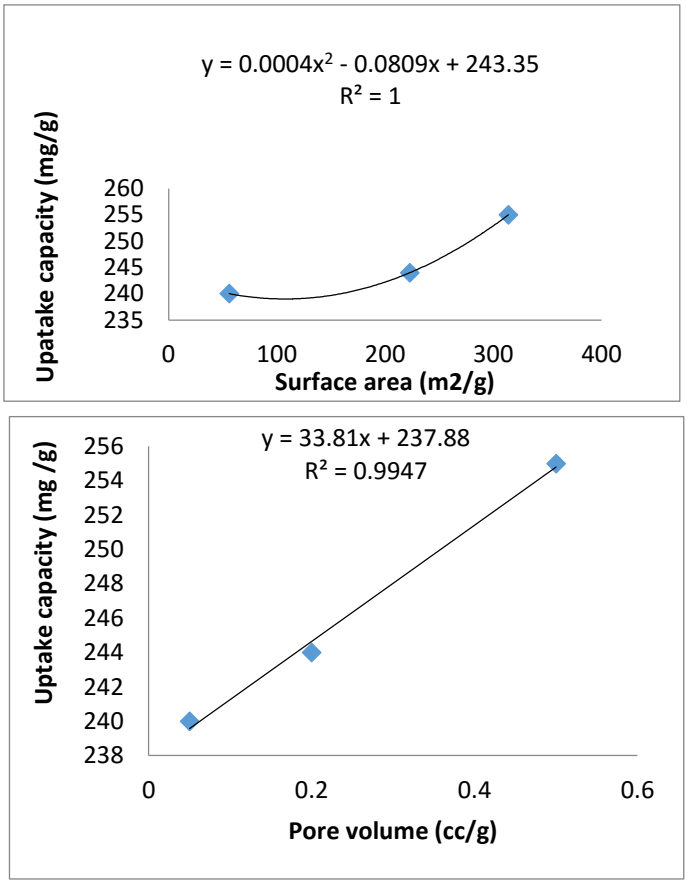

Figure 3.10 The relationship between arsenic uptake capacity and surface properties of alumina.

3.4 Discussion

3.4.1 Formation of MA

Inverse micelles are formed as nanoreactors by surfactants as shown in **Scheme 3.1**. Aluminum oxo-clusters are stabilized in hydrated inverse micelles at a low pH and interact with surfactant via a charge transfer interaction or via hydrogen bonding. The aluminum precursor loaded inverse micelles are packed randomly during the reaction at 120 °C. A concomitant color change to yellow after reaction for approximately 20 mins indicates the formation of NO_x (a wide range of nitric oxides), which is observed during the synthesis of other mesoporous oxides prepared based on the same synthetic strategy (e.g., silica, titania, manganese oxides).[98] Packing is followed by oxidation

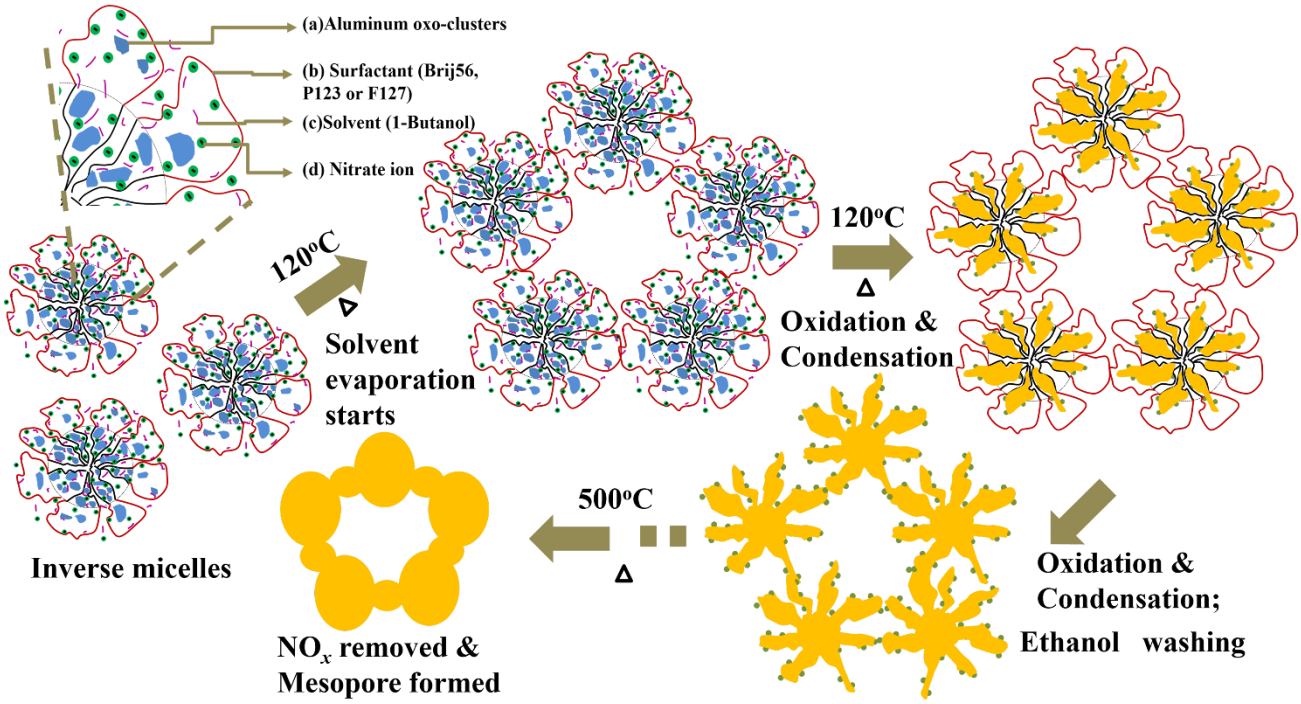

Scheme 3.1 Proposed formation mechanism of mesoporous alumina.

and condensation of the aluminum precursors in the micelles. Surfactant species were oxidized and formed carboxyl groups coordinated to aluminum oxo-clusters, which is observed with transition metal systems.[98] MA is formed as pH increases due to NO_x formation from thermal decomposition of nitrate ions during reaction. Finally, the residual surfactants are washed off, and surface NO_x and carboxyl species are removed after calcination. The crystalline walls of as-synthesized mesoporous

materials are made up of nanoparticles of alumina and the mesopores are the intra-connecting voids formed between randomly packed nanocrystals.[98] The hydrolysis and condensation of aluminum alkoxides are generally faster than that of silicon alkoxides,[87] so synthesis methods used for mesoporous silica have not always yielded satisfactory results for MA. As for our synthesis strategy, the rates of hydrolysis and condensation of aluminum precursors are controlled by *in situ* formation of NO_x from nitrate ions.

3.4.2 Effect of Synthesis Parameters on Textural Properties of MA

The fact that longer reaction times result in larger pore sizes is attributed to the longer condensation time for the precursors. The more precursors condensed during longer reaction time, the more inverse micelles are packed together to form a bigger mesopore and a larger pore volume. This is confirmed by the change of the gel color and the wall thickness. The as-formed gel was white after 4 h, which turned yellow after 6 h and golden yellow after 8 h (**Figure 3.11**). NO_x is adsorbed by the gel during reaction and the color darkens because more NO_x formed, which indicates more precursors participated in this reaction. The wall thickness increases by approximately 68% from reaction times of 4 h to 8 h. At the same time, the pore size increases by approximately 39%.

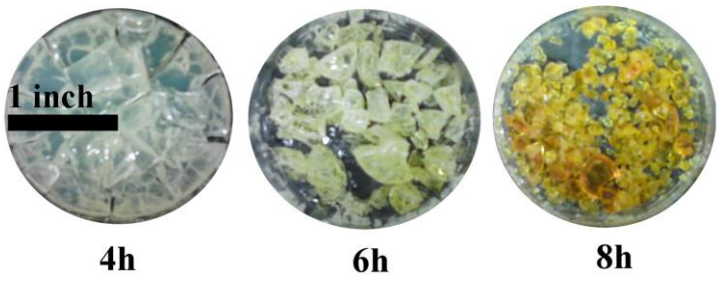

Figure 3.11 Gel color of MA for different reaction times at 120 °C.

There is no need for a stringent selection of surfactants to prepare MA with this facile method. MA with a high surface area and narrow pore size distribution is obtained with non-ionic surfactants like Brij56, P123, and F127 (**Table 3.2**). Furthermore, pore sizes of MA can be continuously adjusted by choosing surfactants with different chain lengths of the PEO block. The chain length of the PEO block of F127 and P123 surfactants is essential in determining the pore size and pore volume of MA,[11] with the central PPO block having the same length. The PEO block chain length of F127 is much longer than that of P123.The sizes of inverse surfactant micelle nanoreactors get bigger, more inverse micelles pack together, and interstitial voids (pores) formed in between the alumina nanoparticles get larger with longer surfactants. The unit number of PEO block of Brij56 is considerably smaller than that of P123 or F127, which generates MA with a smaller pore size and pore volume. PEO block is expected to be more closely associated with the alumina inorganic wall than the more hydrophobic PPO block because PEO blocks interact with the alumina species more strongly through a charge transfer interaction or hydrogen bonding.[99] Therefore, the wall thickness increases as expected by approximately 41% from surfactant of Brij56 to F127 with the increasing length of the PEO block. The pore size increases by approximately 69%. The surfactant chain length has a more efficient effect on increasing the pore size compared with the reaction time.

Calcination temperature and hold time have no obvious effect on the pore sizes of as-synthesized MA, which shows there is good thermal stability of the pore structures under these heat treatment conditions. The increased surface area and pore volume could be due to the departure of organic matter initially present in the pores and around the particles with increased calcination temperature or hold time.[109]

3.4.3 Effect of Textural Properties on D4 Siloxane Adsorption and Adsorbent Regeneration

Since the pore sizes of all the as-synthesized MA samples are larger than the molecular size of D4, pore size is not a limiting parameter for the MA adsorbents. Cabrera-Codony *et al.* reported

that adsorption is strongly related to the textural properties of activated carbons and pore volume plays a key role in D4 siloxane adsorption,[69] which is also a key factor in our systems. As presented in Table 1, although the pore sizes and surface areas of Al120-6h are larger than that of commercially activated alumina, the total pore volume of Al120-6h (0.20 cc g^{-1}) is less than that of commercially activated alumina (0.26 cc g^{-1}). The saturation capacity of Al120-6h (92 mg/g) is 28% less than that of commercially activated alumina. All textural parameters of Al120-8h are larger than that of commercially activated alumina (pore volume of Al120-8h is around 1.8 times of that of commercially activated alumina), and Al120-8h displays a much better performance than that of commercially activated alumina. This is in agreement with our previous work on mesoporous aluminosilicate.[86]

It is hard to avoid undesirable polymerization of D4 siloxane on the surface of the adsorbent.[86] D4 siloxane can interact with hydroxyl groups on the adsorbent surface by hydrogen bonding, and surface hydroxyl groups can function as catalytic active centers for ring-opening polymerization of siloxane.[69,107,110] However, lower or higher molecular weight siloxanes are not detected after one run, which is beneficial for the longevity and regeneration of adsorbents. In addition, acidic and basic sites on Al120-8h are related to the better adsorption performance induced by polymerization,[111] which can also explain the 15% capacity loss in the third recycle of the adsorbent. The CO_2-TPD profiles and FTIR spectra of pyridine adsorption were recorded to study differences in the types, strengths, and the amounts of basic and acidic sites of the selected Al120-8h and commercially activated alumina. These profiles are shown in **Figure 3.12 a and b**, respectively. The CO_2-TPD

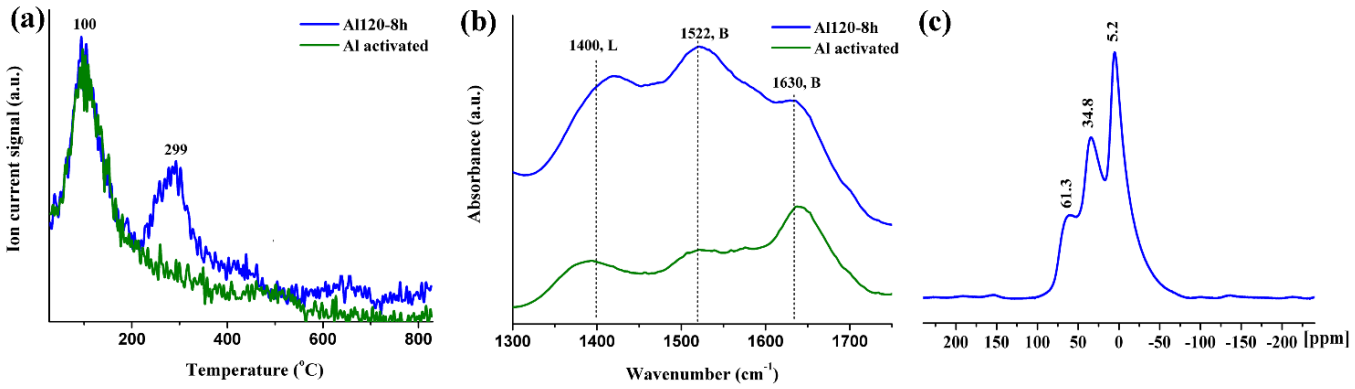

Figure 3.12 (a) CO_2-TPD profiles and (b) pyridine adsorption FTIR spectra for Al120-8h and commercially activated alumina. (c) ^{27}Al MAS NMR spectrum for as-synthesized Al120-8h.

profile of MA Al120-8h in **Figure 3.12a** shows three peaks, indicating the existence of basic sites on the surface of the sample studied. Desorption peaks are centered at 100 and 299 °C, while the main desorption peak of commercially activated alumina is located at 100 °C. Since acidic CO_2 desorbs at a higher temperature from stronger basic sites, and CO_2 desorbs at a higher temperature (299 °C) from MA, Al120-8h has stronger basic sites.[112,113] The amounts of desorbed CO_2 from MA were also larger than that from commercially activated alumina when equal amounts of sample were tested, indicating MA has a larger quantity of basic sites. **Figure 3.12b** shows FTIR spectra of pyridine adsorbed alumina samples at room temperature. Pyridine adsorbs on Brønsted acid sites (1522 and 1630 cm^{-1}) and is labeled as B, pyridine adsorbed on Lewis acid site (1400 cm^{-1}) is labeled as L.[114,115] Both materials contain Brønsted and Lewis acid sites together. The IR absorbance intensities from both acid sites of MA are higher than that of commercially activated alumina, indicating larger amounts of acid sites for MA. MA exhibits a higher amount of Brønsted acid sites accompanied by small amounts of Lewis acid sites. Since aluminum ions are the center of acidity, the acidity profile observed may be due to the aluminum ion distribution of the sample. The coordination environment of aluminum ions in as-synthesized Al120-8h was examined by ^{27}Al MAS NMR spectrometry. The spectrum of as-synthesized alumina displays three resonance signals

at δ=5, 35, and 61 (**Figure 3.12c**). These lines are indicative of six-, five-, and four-coordinate metal centers, respectively.[3] The presence of five-coordinate aluminum ion centers may have significant catalytic activity as Lewis acid centers.[3]

The advantage of a wormhole-like pore structure is its highly inter-connected pore system,[7,87]whose high porosities and large surface areas can be fully utilized. A wormhole-like pore structure can have better diffusion of D4 siloxane in view of mass-transfer limitations.[116] This structure also has enhanced accessibility of the D4 molecules to the active centers (acid-base sites on the adsorbent surface),[86,103,116] which may give rise to the excellent adsorption performance. This wormhole-like pore structure could be one of the reasons why a high adsorption capacity of D4 siloxane is obtained with MA Al120-8h.

3.5 Conclusions

In summary, a sol-gel-based inverse-micelle method with a non-polar solvent (1-butanol) and short reaction times (4-8 h) were successfully modified for the synthesis of MA. The reaction times, surfactant chain lengths, and calcination temperatures and hold times had independent effects on textural properties (pore sizes, surface areas and pore volumes) of MA. The reaction times and surfactants can be selected to continuously adjust the pore sizes and pore volumes of MA, while the calcination temperature and hold time can tune the surface areas and pore volumes without affecting the average pore size. Characterization studies of a representative sample, Al120-8h, by low angle XRD, N_2 sorption, TEM, CO_2-TPD and pyridine adsorption FTIR, show that the material formed a periodic wormhole-like pore structure with relatively high amounts of acidic and basic sites on the surface. Furthermore, Al120-8h presented a high capacity (168 mg/g) compared to commercially activated alumina for D4 siloxane adsorption, which was due to its large mesopore volume. Reusability studies indicate that the as-synthesized MA is a promising adsorbent for the removal of siloxanes from biogas under ambient conditions.

Chapter 4. Mesoporous Alumina Supported Metal Oxide for Methane Oxidation

4.1 Introduction

Natural gas is one of the alternative energy sources for hydrocarbons. Methane, the main component of natural gas, has high hydrogen to carbon ratio. [117] Nowadays, natural gas vehicles (NGVs) attract interests compared to diesel vehicles because of the lower emission of soot particulates and nitrogen oxides (NO_x).[118,119] Under lean burn conditions, NGVs are operated with high fuel efficiency compared to stoichiometric conditions. However, there is a tendency to release unburned methane.[92,120] Since methane is a second most prevalent greenhouse gas, it is highly encouraged to eliminate methane from the environment.[121] Besides, NO_x is favored to be formed at high temperatures. [122–124] One of the solutions to overcome the abovementioned problems is low-temperature catalytic combustion of methane.[125] A complete oxidation of methane at a relatively low temperature (< 500-550 ^oC) is crucial for decreasing unburned methane of the exhaust of NGVs. [126] It is not easy to design catalysts for removing methane due to the strongest carbon hydrogen single bond. Noble metals or supported noble metals (i.e., Pd, Pt, Rh, Pd/Al_2O_3) are active for the complete oxidation of methane. However, the search for catalysts made of earth-abundant elements (Mn, Co, Ni, Cu) is attractive due to the high cost of precious metals. [127–129]

Thermal stability of a catalyst at a temperature of 1,300 ^oC or at least 800 ^oC for engines using gasoline or diesel is required.[126] Alumina is used as support widely because of its good mechanical properties and its ability to have active oxide dispersed. [130] Supported copper oxide have been considered as potential candidates for emission control catalysts because copper oxide has been reported to exhibit a comparable CO oxidation activity with noble metal catalysts. [131] Therefore, MA-supported metal oxides (MnO_x, CoO_x, NiO_x, CuO_x) are promising candidates as thermal stable and efficient catalysts.[128,132,133]

In addition, the partial oxidation of methane has attracted considerable attention for the production of synthesis gas (H_2-CO mixture), which has milder exothermic characteristics and the desirable ratio of H_2/CO for the downstream chemical processes. [128,134]

4.2 Experimental Section

4.2.1 Catalyst Preparation

All chemicals were used as received without further purification. Take copper supported on mesoporous alumina for example. During the synthesis, 5 g aluminum sec-butoxide (Alfa-Aesar) was diluted in 10 g 1-butanol (Sigma-Aldrich) with adding 2 g nitric acid (J.T.Baker) at ambient temperature. At the same time, 2 g Pluronic P123 (Poly (ethylene glycol)-block-Poly(propylene glycol)-block-Poly(ethylene glycol); PEO_{20}-PPO_{70}-PEO_{20}; Sigma-Aldrich) was dissolved in 10 g 1-butanol followed by 0.5 g, 1g, 5g $Cu(NO_3)_2 \cdot 3\ H_2O$ (Sigma-Aldrich), respectively. The two solutions were reacting at 120 ^oC for 4 h, yielding a colored gel. The gel was washed several times with ethanol to remove surfactants and dried in a vacuum oven at room temperature overnight. The obtained powders, after grinding, were placed in a cuvette and calcined in air at 500 ^oC for 1 h, with a 100 $^oC\ min^{-1}$ heating rate. Samples are named as MAlx, with M as the transition metal element, x as the loading molar ratio versus aluminum. For example, CuAl5, CuAl10, and CuAl20 represent copper loading molar amount of 5%, 10% and 20% versus aluminum, respectively.

4.2.2 Characterization

The powder X-ray diffraction (XRD) studies were performed with a Rigaku Ultima IV diffractometer using Cu Kα (λ=0.15406 nm) radiation. A beam voltage of 40 kV and a beam current of 44 mA were used. The low-angle XRD patterns were collected over a 2θ range of 0.5-10° with a continuous scan rate of 0.5° min^{-1}, and the wide-angle XRD patterns were collected over a 2θ range of 10-80° with a continuous scan rate of 2.0° min^{-1}. The crystallographic phases were identified by comparing the wide-angle XRD pattern with the Joint Committee on Powder Diffraction Society (JCPDS) database. The N_2 sorption experiments were done with a Quantachrome Autosorb-1-1C automated sorption system. All the samples were degassed at 150 °C for 3 h under vacuum prior to measurement. The surface areas were calculated using the Brunauer-Emmett-Teller (BET) method, and pore sizes and volumes were calculated from the desorption branch of

the isotherm using the Barrett-Joyner-Halenda (BJH) method. The surface morphologies of the synthesized materials were studied using FEI Nova NanoSEM 450 Field Emission Scanning Electron Microscopy (FE-SEM) on a Zeiss DSM 982 Gemini instrument with a Schottky emitter at an accelerating voltage of 3.0 kV with a beam current of 1.0 mA. The samples were ultrasonically dispersed in ethanol and deposited on Au-coated silicon chips prior to the analysis. The surface morphologies and the crystalline structures of the oxides were examined by high-resolution transmission electron microscopy (HR-TEM). Imaging was performed on a JEOL 2010 instrument with an accelerating voltage of 200 kV. A drop of the material dispersed in ethanol was placed on a carbon-coated copper grid and allowed to dry before analysis. X-ray photoelectron spectra (XPS) characterization of the synthesized materials was done on a Quantum 2000 Scanning ESCA Microprobe, using monochromatic Al Kα radiation (λ = 1486.6 eV) as the radiation source. The spectra were recorded in the fixed analyzer transmission mode with pass energies of 187 and 58 eV for recording survey and high-resolution spectra, respectively. The powder samples were pressed on a carbon tape stuck to a sample stage placed in the analysis chamber. Binding energies (BEs) were measured for C 1s, O 1s, and Cu 2p. The XPS spectra obtained were analyzed and fitted using CasaXPS software (version 2.3.12). Sample charging effects were eliminated by correcting the observed spectra with the C 1s BE value of 284.8 eV. The overlapped Cu 2p and O 1s peaks were deconvoluted into several sub-bands by using an optimal combination of Gaussian (70%) and Lorentzian (30%) functions. Temperature-programmed reduction (TPR) measurements were carried out using a Thermolyne 79300 model temperature programmable tube furnace, and the gases were monitored on a Cirrus MKS PPT Residual Gas Analyzer coupled with a quadrupole mass selective detector to investigate the redox properties of the catalysts. Approximately 0.100 g of catalyst was packed into a quartz tube (i.d. 7 mm) supported with quartz wool and pretreated in a 50 standard cubic centimeters (SCCM) Ar atmosphere at 200 °C for 1 h prior to TPR experiments. The feed of 5% H_2 in Ar with a flow rate of 50 SCCM was used as a reducing gas. The temperature of the sample was raised at a constant rate of 10 °C min^{-1} from RT to 800 °C. The exhaust gas was sampled via a vacuum manifold and heated capillary tube connected at a T-fitting, and the consumed

amount of H_2 and the possible products along with the reducing temperatures were identified and measured using a mass spectrometer.

4.2.3 Methane Combustion Evaluation

The methane combustion evaluations were carried out at atmospheric pressure using an experimental setup which consists of Alicat M-Series mass-flow controllers (MFC) and an electric furnace containing a Platinel II type thermocouple. The methane combustion activities were tested in a fixed-bed quartz reactor (i.d. 3 mm) containing 0.100 g of catalyst supported by quartz wool. The volumetric composition of the feed gas mixture was 2% CH_4 balanced by air and was passed through the catalyst at 100 °C until reaching a steady flow of 10 SCCM, thus giving a weight hourly space velocity (WHSV) of 6 L h^{-1} g^{-1}. After that the temperature was increased in 50 °C increments until 600 °C by holding the temperature for 15 min at each temperature before the injection. The concentrations of the feed gas and the reactor outflow gases were analyzed online with a gas chromatograph (SRI 8610C) equipped with a thermal conductivity detector (TCD) using molecular sieve 13X (6′) and silica gel (6′) columns.

The methane concentration of the feed gas and the reactor outflow, and carbon balance were calculated based on the calibration plot constructed from the integrated GC peak areas of a standard series of methane, carbon dioxide, and carbon monoxide concentration. The conversion of methane, x (%), is defined as the percentage of methane feed that has reacted x (%) = $\{[(CH_4^{\circ} - CH_4)/(CH_4^{\circ})] \times 100\}$. In this function, $CH4^{\circ}$ is the methane concentration at 100 °C and CH_4 is the concentration at a given temperature. The activity of the catalysts was characterized by T10, T50, and T90, which represent the temperatures of methane conversion at 10, 50, and 90%, respectively.

4.3 Results

4.3.1 Physicochemical Characterizations

To illustrate the generality of this synthesis approach, a series of transition metal elements, manganese, cobalt, nickel, and cerium, were supported on mesoporous alumina with different molar ratios of 5%, 10% and 20% using a one-pot synthesis. As shown in **Figure 4.1**, all samples show typical Type IV isotherm curves, which demonstrate their mesoporosity. Monomodal pore size distributions are presented in **Figure 4.2**. Regardless of transition metal elements or amounts, the pore size remains almost the same value for a certain series. **Table 4.1** summarizes the textural properties for all the samples. Moreover, a larger amount of loading is possible as demonstrated by loading 50% of cerium,

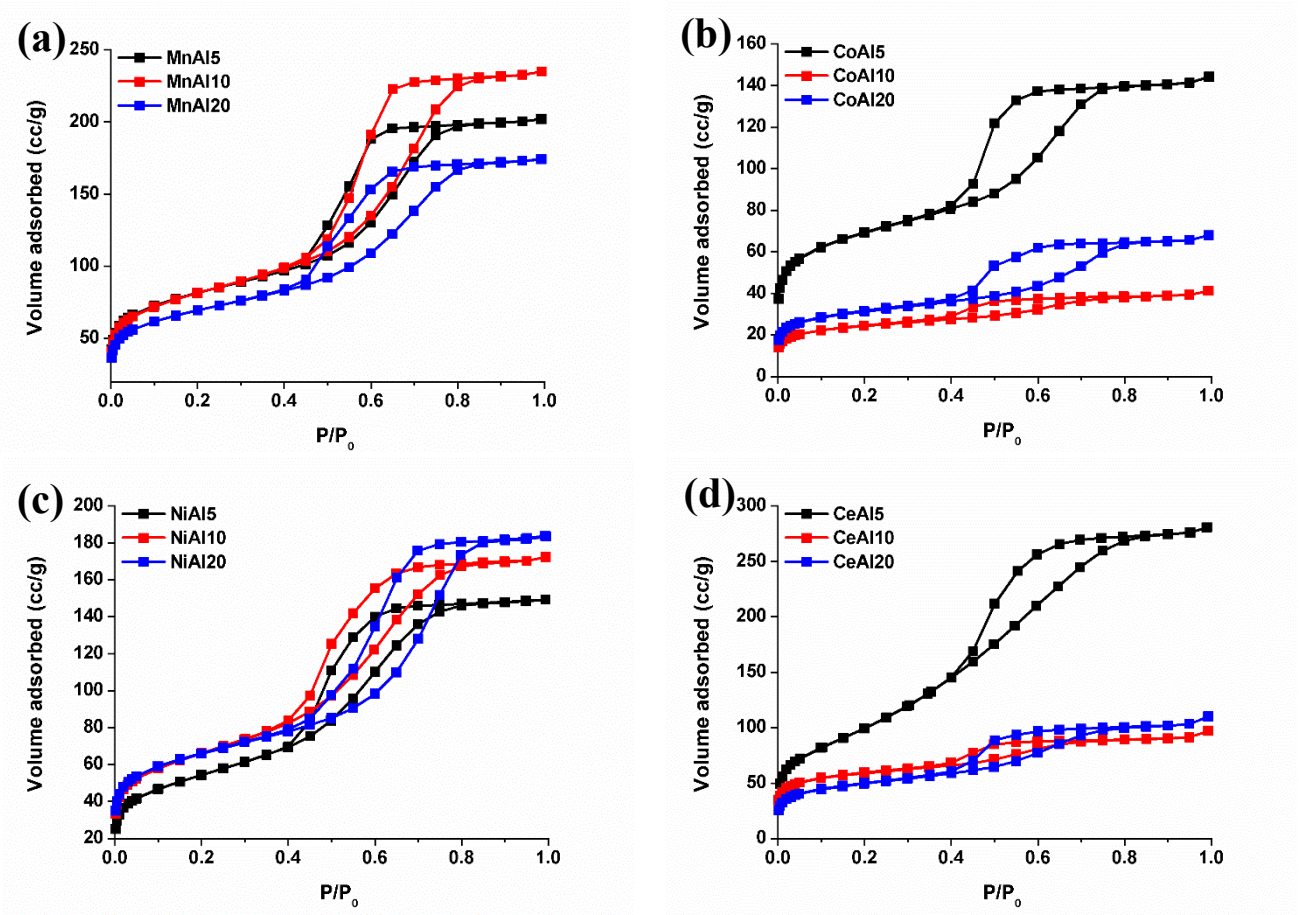

Figure 4.1 Nitrogen sorption isotherm curves of (a)MnAl5, MnAl10, MnAl20; (b) CoAl5, CoAl10, CoAl20; (c)NiAl5, NiAl10, NiAl20; and (d) CeAl5, CeAl10, CeAl20.

enlarging the pore size to 8.8 nm, which provides the possibility of a cerium-alumina support for further applications.

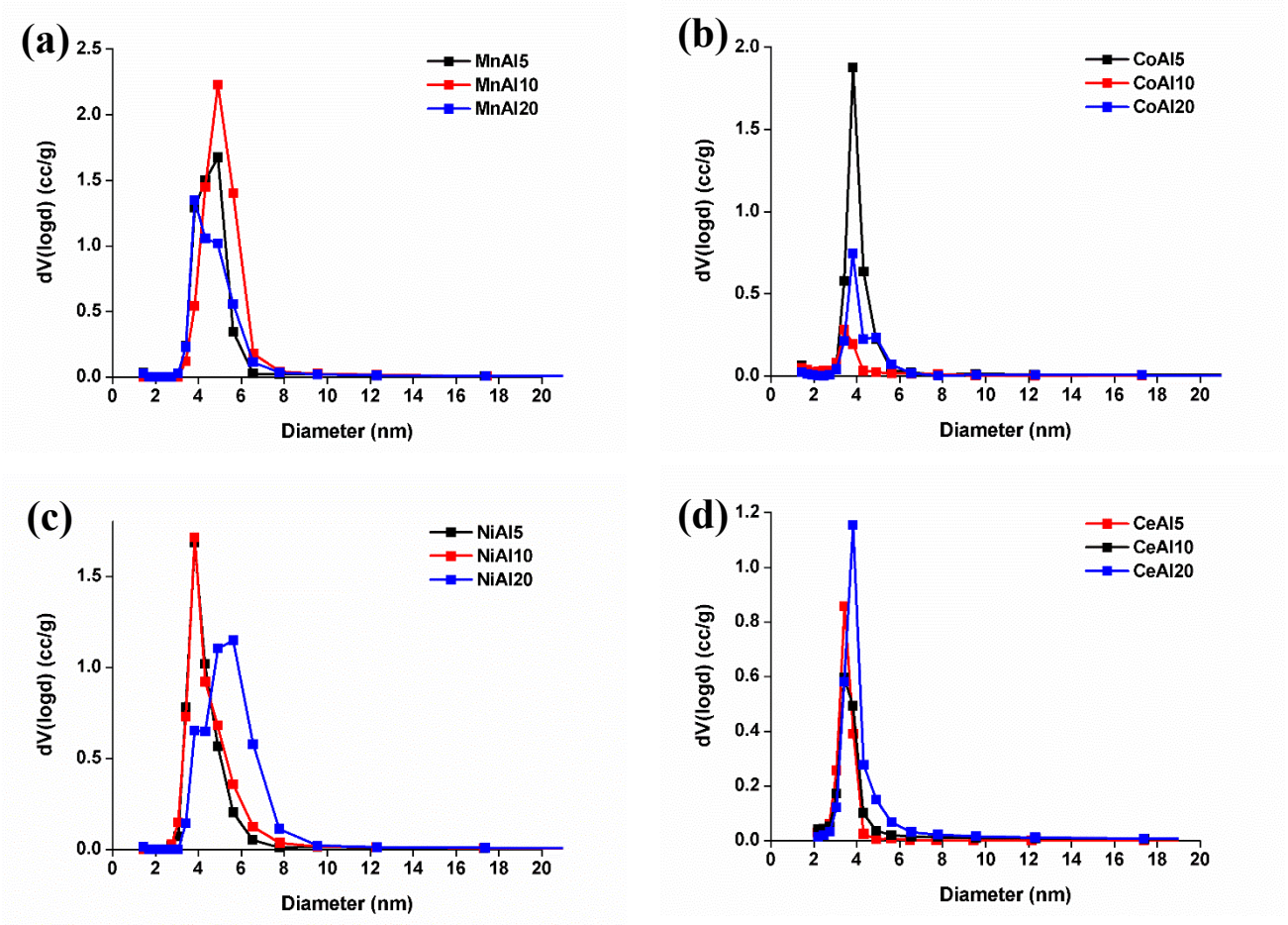

Figure 4.2 Pore size distribution of (a) MnAl5, MnAl10, MnAl20; (b) CoAl5, CoAl10, CoAl20; (c) NiAl5, NiAl10, NiAl20; and (d) CeAl5, CeAl10, CeAl20.

Table 4.1 Texture properties of transition metal supported mesoporous alumina.

	Surface Area (m^2/g)	**Pore Diameter (nm)**	**Total Pore Volume (cc/g)**
MnAl5	273	4.3	0.29
MnAl10	264	4.9	0.35
MnAl20	234	3.8	0.25
CoAl5	216	3.8	0.19
CoAl10	79	3.4	0.03
CoAl20	103	3.8	0.09
NiAl5	186	3.8	0.23
NiAl10	233	3.8	0.25
NiAl20	209	4.9	0.27
CeAl5	195	2.7	0.13
CeAl10	190	3.4	0.11
CeAl20	165	3.8	0.15
CeAl50	146	8.8	0.32

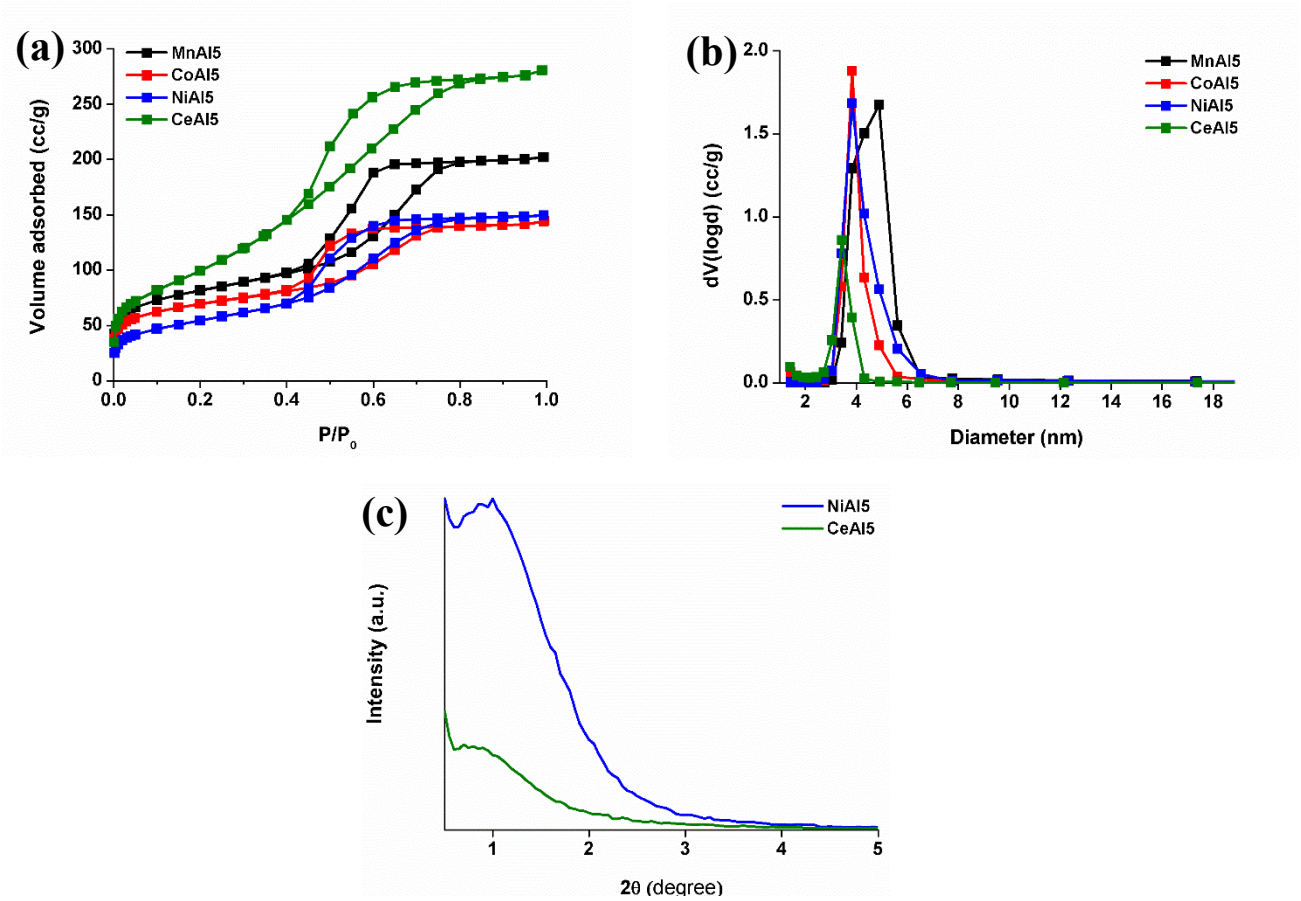

Figure 4.3 (a) N_2 sorption isotherm curves and (b) pore size distribution for samples MnAl5, CoAl5, NiAl5, and CeAl5. (c) low-angle XRD for samples NiAl5 and CeAl5.

This approach is applicable for synthesizing different transition metals supported on mesoporous alumina. The reaction time at 120 ^{o}C for all the samples is 4 hours, and the gel after washing is put directly in the furnace at 500 ^{o}C with a high ramp rate. As for mesoporous alumina, reaction time at 4 h leads to a small surface area of 56 m^2/g and pore diameter of 3.1 nm compared to that of the transition metal supported ones (**Table 4.4**). The inclusion of transition metal elements promotes the micelle formation and the mesopore structure construction. However, from the structural point of view, only NiAl5 and CeAl5 among 5% loading materials show peaks in the low-angle XRD range, which indicates loading Ni and Ce maintains

the uniform and organized mesopore structure. NiAl5 has a more organized mesostructure due to the higher intensity of the low angle XRD peak. **Figure 4.3** shows N_2 sorption isotherm curves for four samples with theoretical molar ratio 5% of transition metal elements (Mn, Co, Ni, Ce). All of them have typical Type IV isotherm curves and steep capillary condensation. This indicates that including transition metals does not affect the mesoporosity of the alumina support. The isotherm curves show H1 hysteresis loops. The slight shift of condensation steps to higher relative pressures with different transition metals is hard to distinguish, which indicates that a change of pore size is not obvious. According to the pore size distribution, the slight increasing order is as follows: CeAl5< CoAl5=NiAl5<MnAl5, which is also summarized with the values in **Table 4.2**. MnAl5 has the maximum values for all the textural properties. SEM-EDX data give an elemental molar ratio of transition metal versus aluminum, which is in the range of 2%-4%.

Table 4.2 Texture property for transition metals (5%) supported on mesoporous alumina.

Sample	**EDX Ratio**	**Surface Area (m^2/g)**	**Pore Diameter (nm)**	**Pore Volume (cc/g)**
MnAl5	4%	273	4.3	0.29
CoAl5	2%	216	3.8	0.19
NiAl5	3%	186	3.8	0.23
CeAl5	2%	195	2.7	0.13

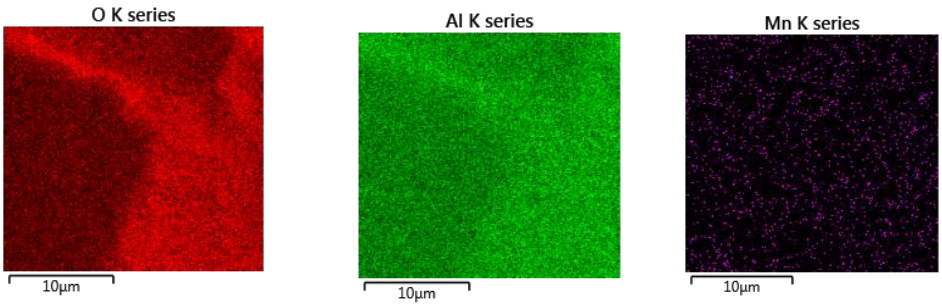

Figure 4.4 Elemental mapping for representative sample MnAl5.

The elemental mapping of representative MnAl5 (**Figure 4.4**) in the same region shows manganese is supported evenly on aluminum. Methane partial oxidation was evaluated over the four samples by temperature-programmed studies. Take NiAl5 for example. A partial oxidation mechanism can be proposed based on the studies in **Figure 4.5**. CO_2 and H_2O are formed at approximately 100 ^oC. Then at the temperature of 500 ^oC, CO and H_2 are increased steeply at the expenses of CO_2 and H_2O. The reforming

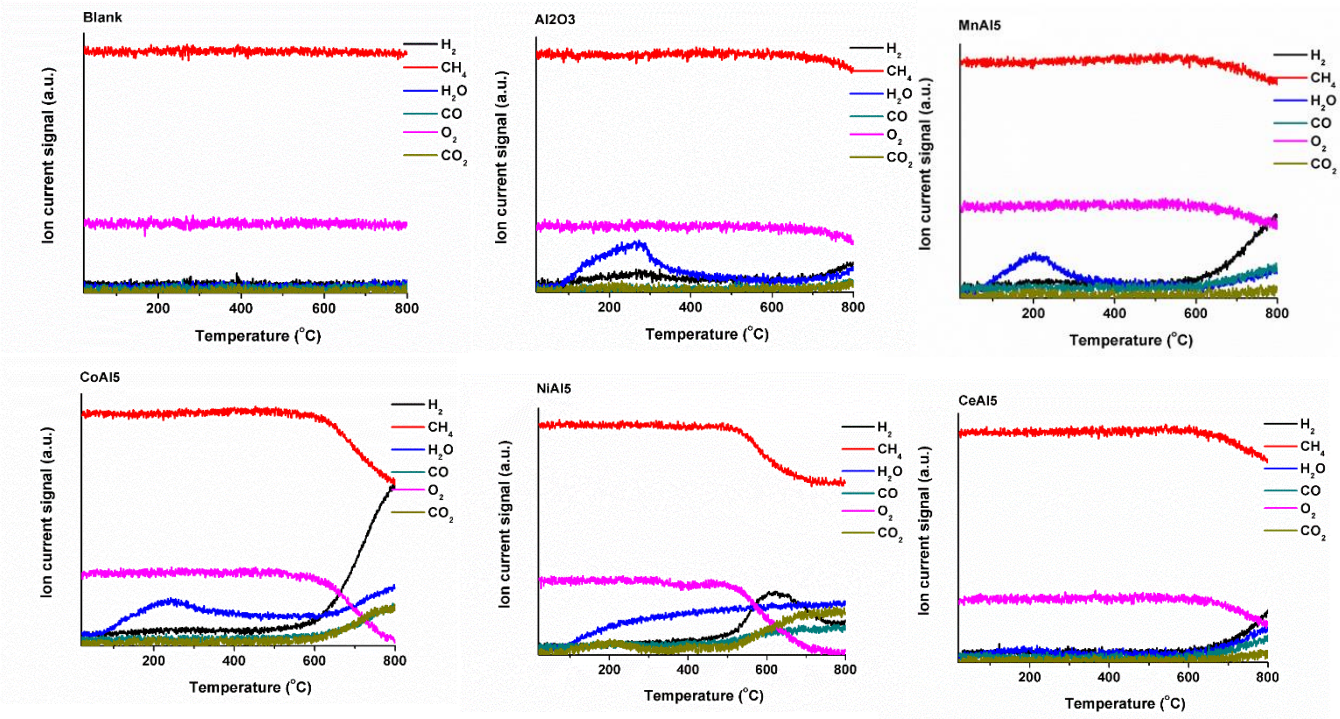

Figure 4.5 Temperature-programmed studies for methane partial oxidation over blank quartz wool, samples alumina, MnAl5, CoAl5, NiAl5, and CeAl5.

reaction of CH_4 with CO_2 and H_2O to form CO and H_2 occurs, which is in agreement with an indirect oxidation mechanism. [135,136] Reduced transition metals supported on mesoporous alumina are expected to have higher selectivities for synthesis gas.[128] As for methane combustion shown in **Figure 4.6** and **Table**

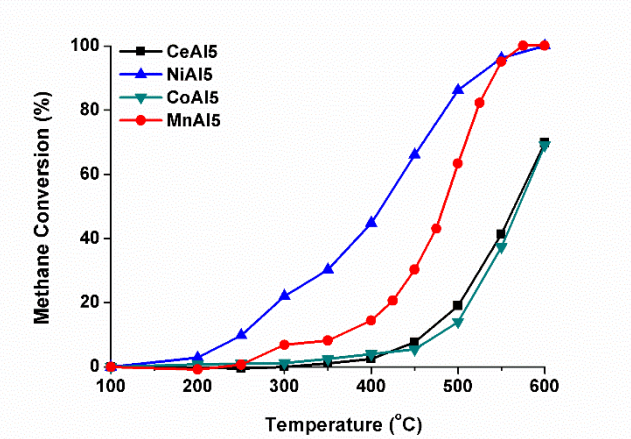

Figure 4.6 Methane combustion evaluation over samples MnAl5, CoAl5, NiAl5, and CeAl5.

4.3, methane conversion temperature T_{10} and T_{50} follow the order of NiAl5<MnAl5<CeAl5<CoAl5. Carbon balance is calculated for all of the samples during the temperature range tested, CeAl5 and CoAl5 have carbon balance except that there is CO produced at 600 °C for CeAl5. Even though MnAl5 and NiAl5 have better performance for methane combustion, carbon balance is not maintained during a certain temperature range (**Table 4.3**), which indicates that there are other products containing carbon except for CO_2 and CO not detected by TCD detectors of GC-MS. A cold trap set-up should be used to quench the product for further analysis.

Table 4.3 Methane combustion performance evaluation for transition metal supported on alumina.

Sample	T10 (°C)	T50(°C)	T90 (°C)	CO (ppmv at 600 °C)	No Carbon balance Range

MnAl5	365	485	541	0	300-450
NiAl5	250	413	520	0	250-600
CeAl5	461	567	-	0.0013	-
CoAl5	475	569	-	0	-

4.3.2 Copper supported on Mesoporous Alumina

As shown in **Figure 4.7**, N_2 sorption isotherm curves are typical Type IV regardless of different copper

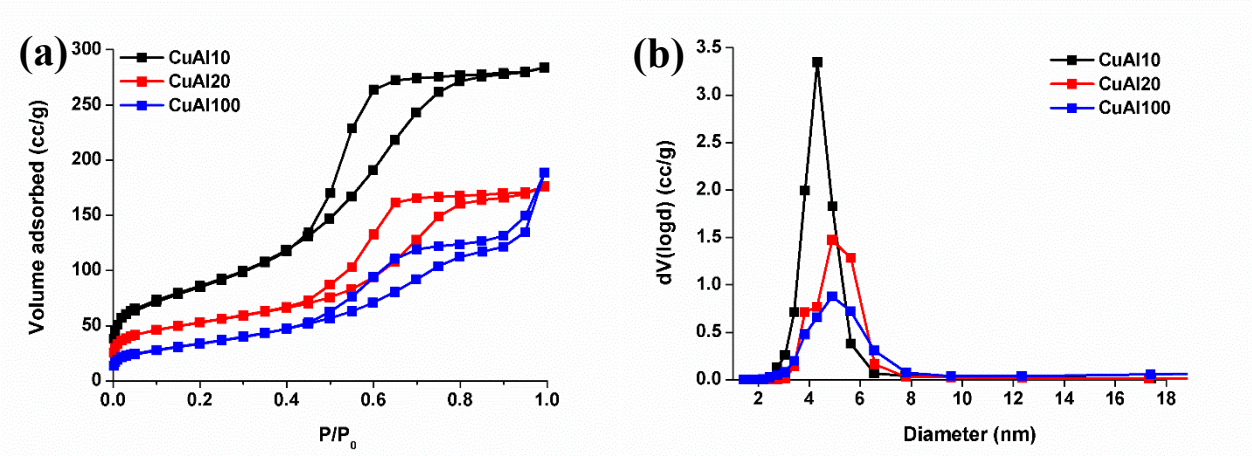

Figure 4.7 (a) N_2 sorption isotherm curves and (b) pore size distribution for samples CuAl10, CuAl20, and CuAl100.

loadings. Only CuAl100 shows a peak in the low angle XRD range. As shown in **Table 4.4**, the surface areas of CuAl10, CuAl20, and CuAl100 are 309, 182, and 126 m^2/g, respectively. The average pore diameters are 4.3, 4.9, and 4.9 nm, respectively. With the introduction of copper to 10% versus aluminum molar amount, the surface area increases to approximately 5.5 times as compared to pure mesoporous alumina. The pore diameter increases from 3.1 nm to 4.3-4.9 nm when including the copper element on the pure mesoporous alumina. Urea is used as a structure directing agent for comparisons based on the studies of Yu *et al.*[137] SEM-EDX elemental mapping (**Figure 4.8**) of CuAl10 demonstrates that copper is distributed uniformly on the mesoporous alumina. TEM images in **Figure 4.9** show black spots are

supported on mesoporous alumina. The spreading areas of the black spots are enlarged on increasing the loading amount.

Table 4.4 Texture property of copper supported on alumina

Samples	Surface Areas (m^2/g)	Pore Diameter (nm)	Pore Volume (cc/g)
CuAl10-Urea1	244	2.3	0.14
CuAl10-Urea3	108	2.4	0.06
CuAl10-120/6h	115	11.1	0.32
CuAl10	309	4.3	0.48
CuAl20	182	4.9	0.28
CuAl100	126	4.9	0.3
Al120-4h	56	3.1	0.05

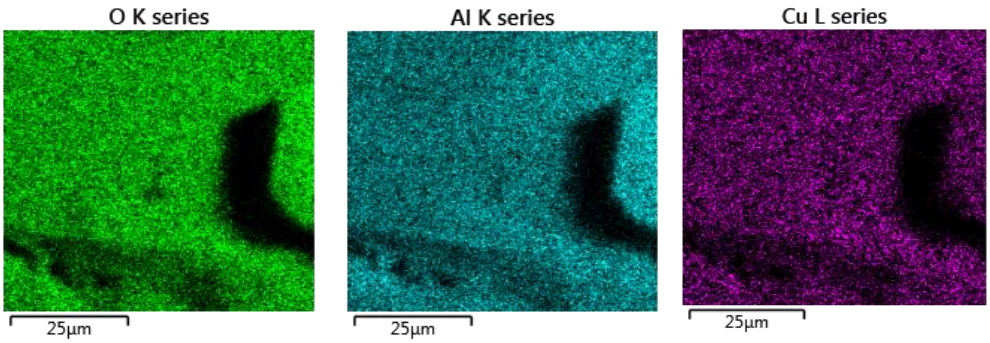

Figure 4.8 SEM-EDX elemental mapping for representative sample CuAl10.

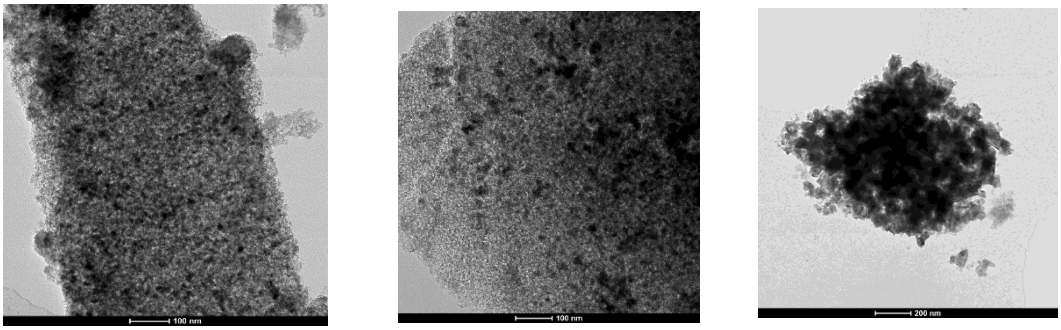

Figure 4.9 TEM images for samples CuAl10, CuAl20, and CuAl100.

4.3.3 Methane Combustion Evaluation

As shown in **Figure 4.10** and **Table 4.5**, a carbon balance is maintained during the whole reaction processes for all the samples, which indicates the processes are total methane oxidation or methane combustion. The measured T_{10} follows the order of CuAl100 (290 ^{o}C) < CuAl20 (320 ^{o}C) < CuAl100-mix

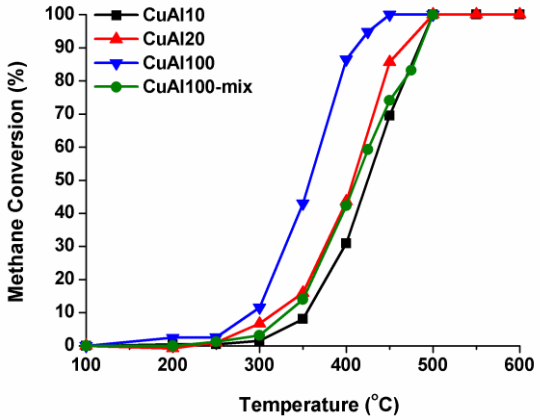

Figure 4.10 Methane combustion evaluation over samples CuAl10, CuAl20, CuAl100, and CuAl100-mix.

(335 ^{o}C) < CuAl10 (355 ^{o}C). T_{50} follows the order of CuAl100 < CuAl20 < CuAl100-mix < CuAl10. The order for T_{90} is CuAl100 < CuAl20 < CuAl10 < CuAl100-mix. Since the methane oxidation activity is improved with increased copper loading, a 100% ratio of copper versus aluminum was selected to be mixed with mesoporous alumina by grinding, for comparison. Based on the temperature at different methane conversions, mechanical mixing of copper oxide and mesoporous alumina has a less efficient methane catalytic oxidation effect than the one-pot synthesized sample when the theoretical molar ratio of Cu vs. Al is the same. This is further confirmed by H_2-TPR tests (**Figure 4.11**). CuAl100 has a lower hydrogen

consumption temperature than that of the CuAl100-mix. Generally, impregnation is used for preparing supported metal oxides. But this route is limited by incorporating a certain amount of target elements. Herein, impregnation of copper nitrate solution was tried, however, 100% molar ratio incorporation failed to form aggregated hard particles adhered to the bottom of the vial. This is because the copper amount is too large to be impregnated on mesoporous alumina.

Table 4.5 Methane combustion performance evaluation for copper supported on alumina.

Sample	T10 (ºC)	T50(ºC)	T90 (ºC)	CO	No Carbon balance range
CuAl10	355	424	484	0	-
CuAl20	320	408	466	0	-
CuAl100	290	357	413	0	-
CuAl100-mix	335	409	486	0	-

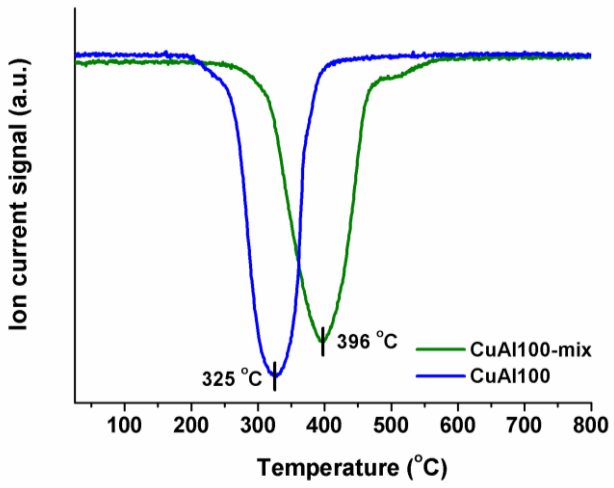

Figure 4.11 H_2-TPR for CuAl100 and CuAl100-mix.

The copper environments of samples CuAl10, CuAl20, and CuAl100 were studied by EPR tests (**Figure 4.12**). Both CuAl10 and CuAl20 show that Copper (II) species have an asymmetric derivative peak at higher magnetic field and one small absorption peak, which corresponds to an axially elongated octahedral geometry, and coordination to one atom, respectively. CuAl100 shows an octahedral geometry without obvious coordination to another atom.

Table 4.6 Total number of spins from EPR test.

Sample	Total number of spins
CuAl10	1.9×10^{19}
CuAl20	2.5×10^{19}
CuAl100	9.3×10^{18}

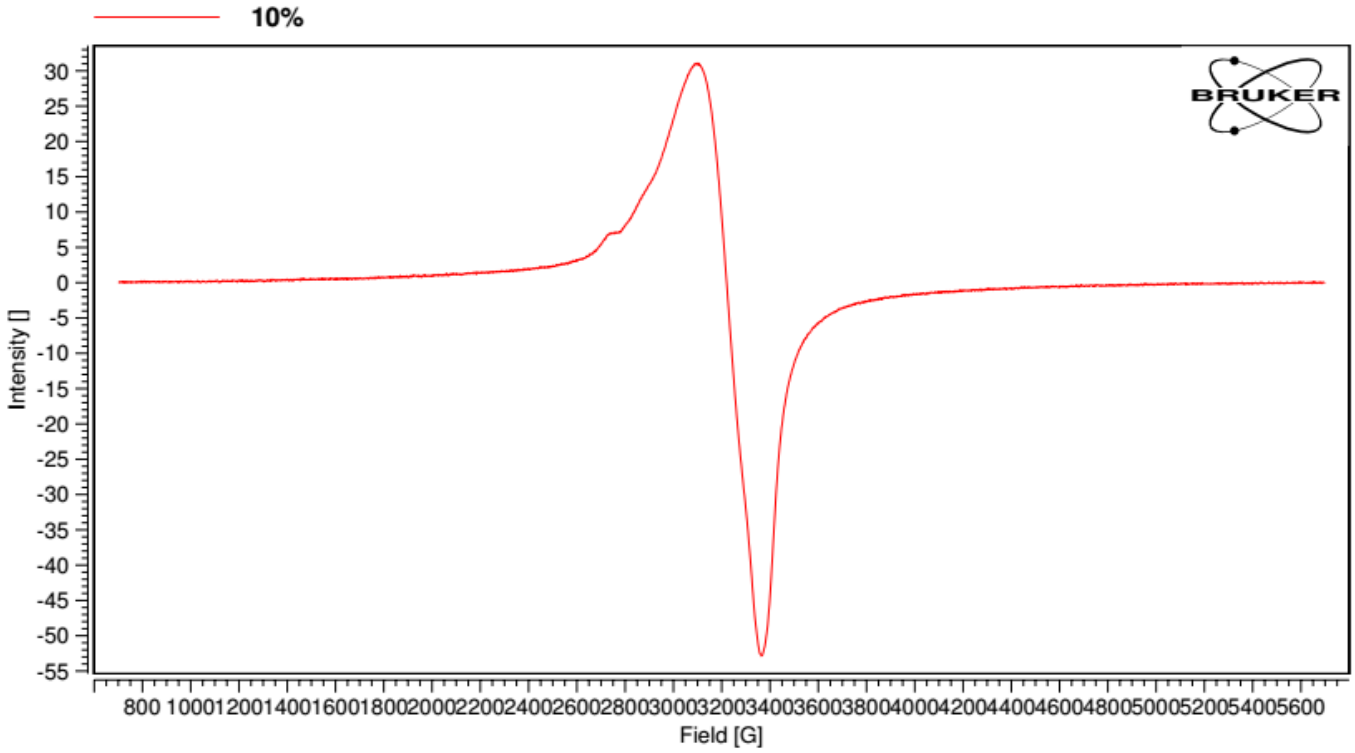
10%
BRUKER
Intensity []
30
25
20
15
10
5
0
-5
-10
-15
-20
-25
-30
-35
-40
-45
-50
-55
800 1000 1200 1400 1600 1800 2000 2200 2400 2600 2800 3000 3200 3400 3600 3800 4000 4200 4400 4600 4800 5000 5200 5400 5600
Field [G]

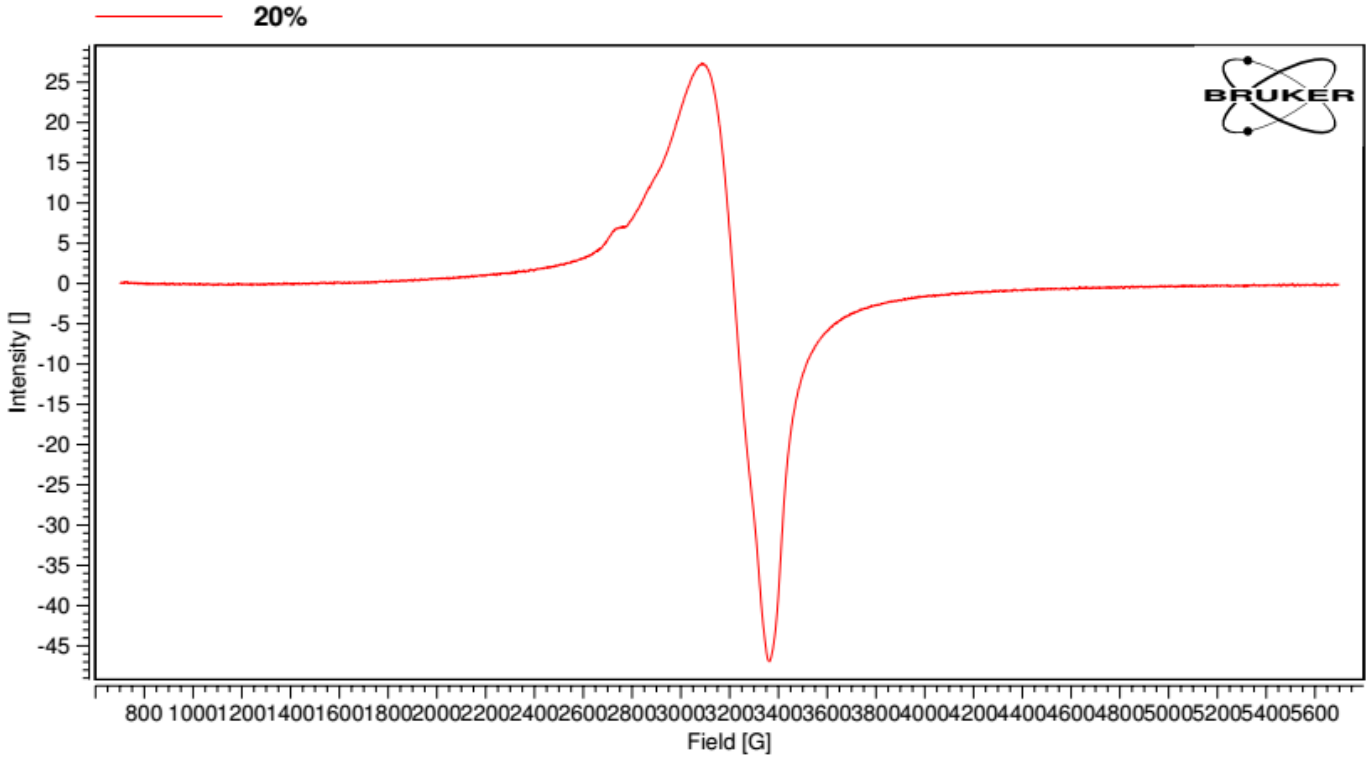
20%
BRUKER
Intensity []
25
20
15
10
5
0
-5
-10
-15
-20
-25
-30
-35
-40
-45
800 1000 1200 1400 1600 1800 2000 2200 2400 2600 2800 3000 3200 3400 3600 3800 4000 4200 4400 4600 4800 5000 5200 5400 5600
Field [G]

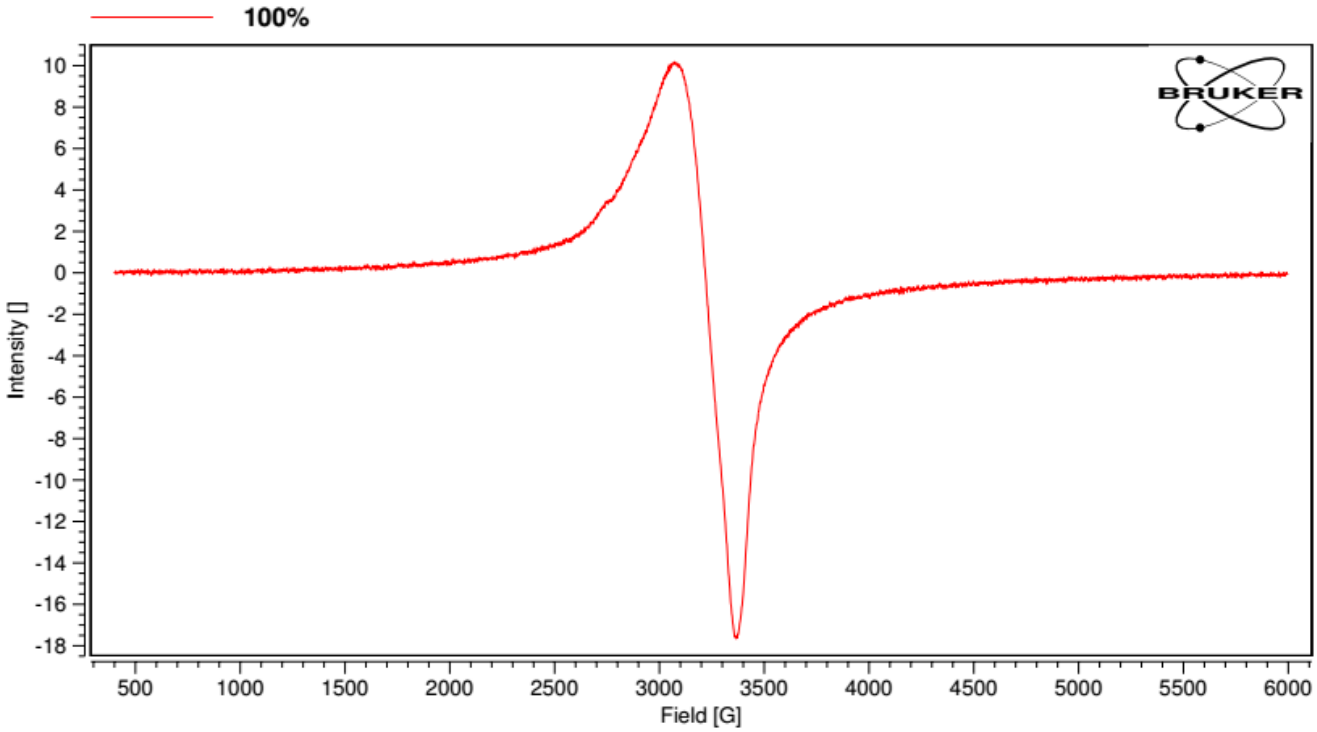

Figure 4.12 EPR spectra for samples CuAl10, CuAl20, and CuAl100.

Chapter 5. Outlook

- **Mesoporous Alumina for Antimony Adsorption**

Antimony is widely used for a variety of industrial purposes, such as battery composites, glass refining agents, semiconductor ingredients. In 2013, world Sb mine production was estimated to be 163,000 metric tons according to the US Geological Survey.[138] High concentrations of Sb in several aquatic environments are from anthropic Sb mining, smelting, and disposal as well as rock weathering and soil runoff. Typical concentrations of antimony in fresh water are less than 1 μg/L. [139] While in mining areas, Sb concentrations range from 2 to 6384 μg/L. [140–142]

The United States Environmental Protection Agency (USEPA) and the European Union (EU) consider antimony and its compounds to be priority pollutants.[139,143] There is a high risk of contaminating local drinking water sources from elevated levels of Sb in ground water. Therefore, it is an urgent issue for water supply safety to remove Sb from the water. The ways to remove Sb include adsorption, coagulation-flocculation and membrane separation. [144–147] Among them, adsorption is simple, flexible in installations, easy to operate. An effective adsorbent with high performance is the key factor to this method. [138] Sb is bounded with charged minerals in soil and sediments, which includes iron, aluminum, and manganese oxyhydroxides and (hydr) oxides.[148] Therefore, goethite, AlOOH, Fe-Mn oxides, and Fe-Zr oxides have been studied for removal of Sb.[149,150] Aluminum has a higher abundance than iron or manganese, suggesting aluminum oxides and hydroxides have potential as cost-effective adsorbents. Mesoporous alumina (MA) has high surface areas, large pore volumes, tunable pore sizes, which have demonstrated advantages in mitigation of AsO_4^{3-} and PO_4^{3-}. [151,152] The similarity between As, P, and Sb also suggests that MA can be a promising candidate for Sb removal. Moreover, MA-supported metal oxides (FeO_x, MnO_x) are promising candidates as Sb adsorbents.

It is an urgent challenge to remove Sb from fresh water. Moreover, due to the knowledge gaps in understanding Sb adsorption to the mineral surface on a molecular-level, experimental and theoretical studies are of fundamental importance.

- **Materials for Methane Oxidation**

Ordered hexagonal mesoporous alumina (MA) is expected to be obtained after modification of the synthesis strategy described above. The modification includes the reaction temperature and time (e.g. 60 ^{o}C for 24 h), and the ratio of surfactant and nitric acid. It is meaningful to compare the adsorption and methane (or hydrocarbon) oxidation performances between different mesoporous structures. Ni supported on MA is expected to show high selectivity for synthesis gas.[135,136] This can be prepared by *in-situ* hydrogen reduction after loading nickel on MA. Copper oxide is expected to have good methane combustion performances at low temperatures. It is interesting and a challenge to synthesize copper oxides by soft chemistry methods with mesoporous structures which have large specific surface areas and size selectivity. [153] Mesoporous perovskite materials provide tremendous possibilities for methane oxidation and other applications (e.g. water splitting, oxygen or hydrogen evolution), however, synthesis methods need to be studied due to the high calcination temperatures for crystal phase formation of perovskites where much information is not known. Modular design of catalysts to combine different components is expected to show exceptional activity at low temperatures for methane combustion. [154]

References

(1) Čejka, J. Organized Mesoporous Alumina: Synthesis, Structure and Potential in Catalysis. *Appl. Catal. A Gen.* **2003**, *254* (2), 327–338.

(2) Bagshaw, S. a; Prouzet, E.; Pinnavaia, T. J. Templating of Mesoporous Molecular Sieves by Nonionic Polyethylene Oxide Surfactants. *Science* **1995**, *269* (5228), 1242–1244.

(3) Bagshaw, S. A.; Pinnavaia, T. J. Mesoporous Alumina Molecular Sieves. *Angew. Chemie Int. Ed. English* **1996**, *35* (10), 1102–1105.

(4) Vaudry, F.; Khodabandeh, S.; Davis, M. E. Synthesis of Pure Alumina Mesoporous Materials. *Chem. Mater.* **1996**, *8* (7), 1451–1464.

(5) Yada, M.; Kitamura, H.; Machida, M.; Kijima, T. Biomimetic Surface Patterns of a Layered Aluminum Oxide Mesophase Templated by Mixed Surfactant Assemblies. *Langmuir* **1997**, *13* (20), 5252–5257.

(6) Yada, M.; Hiyoshi, H.; Ohe, K.; Machida, M.; Kijima, T. Synthesis of Aluminum-Based Surfactant Mesophases Morphologically Controlled through a Layer to Hexagonal Transition. *Inorg. Chem.* **1997**, *36* (24), 5565–5569.

(7) Cabrera, S.; Haskoiiri, J. E.; Alamo, J.; Beltrán, A.; Beltrân, D.; Mendioroz, S.; Dolores Marcos, M.; PedroAmorôs. Surfactant-Assisted Synthesis of Mesoporous Alumina Showing Continuously Adjustable Pore Sizes. *Adv. Mater.* **1999**, *11* (5), 379–381.

(8) Deng, W.; Bodart, P.; Pruski, M.; Shanks, B. H. Characterization of Mesoporous Alumina Molecular Sieves Synthesized by Nonionic Templating. *Microporous Mesoporous Mater.* **2002**, *52* (3), 169–177.

(9) Mitsunori Yada, M. M. and T. K. D. Synthesis and Deorganization of an Aluminium-Based Dodecyl Sulfate Mesophase with a Hexagonal Structure. *chem.Commun.* **1996**, 769–770.

(10) Zhang, Z.; Pinnavaia, T. J. Mesoporous ??-Alumina Formed through the Surfactant-Mediated Scaffolding of Peptized Pseudoboehmite Nanoparticles. *Langmuir* **2010**, *26* (12), 10063–10067.

(11) Cai, W.; Yu, J.; Jaroniec, M. Effect of Nonionic Structure-Directing Agents on Adsorption and Structural Properties of Mesoporous Alumina. *J. Mater. Chem.* **2011**, *21* (25), 9066.

(12) Rashidi, F.; Kharat, A. N.; Rashidi, A. M.; Lima, E.; Lara, V.; Valente, J. S. Fractal Geometry Approach to Describe Mesostructured Boehmite and Gamma-Alumina Nanorods. *Eur. J. Inorg. Chem.* **2010**, No. 10, 1544–1551.

(13) Sing, K. S. W. Reporting Physisorption Data for Gas/solid Systems with Special Reference to the Determination of Surface Area and Porosity (Recommendations 1984). *Pure Appl. Chem.* **1985**, *57* (4), 603–619.

(14) Naumov, S. Hysteresis Phenomena in Mesoporous Materials, 2009.

(15) Lowell, S.; Shields, J. E.; Thomas, M. A.; Thommes, M. Other Surface Area Methods; 2004; pp 82–93.

(16) Diaz, I.; Mayoral, A. TEM Studies of Zeolites and Ordered Mesoporous Materials. *Micron* **2011**, *42* (5), 512–527.

(17) González-Pea, V.; Díaz, I.; Márquez-Alvarez, C.; Sastre, E.; Pérez-Pariente, J. Thermally Stable Mesoporous Alumina Synthesized with Non-Ionic Surfactants in the Presence of Amines. *Microporous Mesoporous Mater.* **2001**, *44–45*, 203–210.

(18) Tao, F. F.; Shan, J.-J.; Nguyen, L.; Wang, Z.; Zhang, S.; Zhang, L.; Wu, Z.; Huang, W.; Zeng, S.; Hu, P. Understanding Complete Oxidation of Methane on Spinel Oxides at a Molecular Level. *Nat. Commun.* **2015**, *6*, 7798.

(19) Ricaurte Ortega, D.; Subrenat, a. Siloxane Treatment by Adsorption into Porous Materials. *Environ. Technol.* **2009**, *30* (10), 1073–1083.

(20) El-Nadjar, W.; Bonne, M.; Trela, E.; Rouleau, L.; Mino, A.; Hocine, S.; Payen, E.; Lancelot, C.; Lamonier, C.; Blanchard, P.; Courtois, X.; Can, F.; Duprez, D.; Royer, S. Infrared Investigation on Surface Properties of Alumina Obtained Using Recent Templating Routes. *Microporous Mesoporous Mater.* **2012**, *158*, 88–98.

(21) Chin, Y. H.; Buda, C.; Neurock, M.; Iglesia, E. Consequences of Metal-Oxide Interconversion for C-H Bond Activation during CH4 Reactions on Pd Catalysts. *J. Am. Chem. Soc.* **2013**, *135* (41), 15425–15442.

(22) Luo, Z.; Poyraz, A. S.; Kuo, C.; Miao, R.; Meng, Y.; Chen, S.; Jiang, T.; Wenos, C.; Suib, S. L. Crystalline Mixed Phase (Anatase / Rutile) Mesoporous Titanium Dioxides for Visible Light Photocatalytic Activity. *Chem. Mater.* **2015**, *27* (1), 6–17.

(23) Gomathi Devi, L.; Girish Kumar, S.; Mohan Reddy, K.; Munikrishnappa, C. Photo Degradation of Methyl Orange an Azo Dye by Advanced Fenton Process Using Zero Valent Metallic Iron: Influence of Various Reaction Parameters and Its Degradation Mechanism. *J. Hazard. Mater.* **2009**, *164* (2–3), 459–467.

(24) Xu, Y.; Li, X.; Cheng, X.; Sun, D.; Wang, X. Degradation of Cationic Red GTL by Catalytic Wet Air Oxidation over Mo-Zn-Al-O Catalyst under Room Temperature and Atmospheric Pressure. *Environ. Sci. Technol.* **2012**, *46* (5), 2856–2863.

(25) Ovejero, G.; Sotelo, J. L.; Rodríguez, A.; Vallet, A.; García, J. Wet Air Oxidation and Catalytic Wet Air Oxidation for Dyes Degradation. *Environ. Sci. Pollut. Res. Int.* **2011**, *18* (9), 1518–1526.

(26) Levec, J.; Pintar, A. Catalytic Wet-Air Oxidation Processes: A Review. *Catal. Today* **2007**, *124* (3–4), 172–184.

(27) Arslan-Alaton, I.; Ferry, J. L. Application of Polyoxotungstates as Environmental Catalysts: Wet Air Oxidation of Acid Dye Orange II. *Dye. Pigment.* **2002**, *54* (1), 25–36.

(28) Rodríguez, A.; Ovejero, G.; Romero, M. D.; Díaz, C.; Barreiro, M.; García, J. Catalytic Wet Air Oxidation of Textile Industrial Wastewater Using Metal Supported on Carbon Nanofibers. *J. Supercrit. Fluids* **2008**, *46* (2), 163–172.

(29) Wu, J.-M.; Wen, W. Catalyzed Degradation of Azo Dyes under Ambient Conditions. *Environ. Sci. Technol.* **2010**, *44* (23), 9123–9127.

(30) Liu, Y.; Sun, D. Development of Fe2O3-CeO2-TiO2/γ-Al2O3 as Catalyst for Catalytic Wet Air Oxidation of Methyl Orange Azo Dye under Room Condition. *Appl. Catal. B Environ.* **2007**, *72* (3–4), 205–211.

(31) Duprez, D.; Can, F.; Courtois, X.; Batiot-dupeyrat, C.; Laassiri, S.; Alamdari, H. Perovskites as Substitutes of Noble Metals for Heterogeneous Catalysis : Dream or Reality. *Chem. Rev.* **2014**, *114*, 10292.

(32) Ma, H.; Zhuo, Q.; Wang, B. Characteristics of CuO-MoO3-P2O5 Catalyst and Its Catalytic Wet Oxidation (CWO) of Dye Wastewater under Extremely Mild Conditions. *Environ. Sci. Technol.* **2007**, *41* (21), 7491–7496.

(33) Srikhaow, A.; Smith, S. M. Preparation of Cu2(OH)3NO3/ZnO, a Novel Catalyst for Methyl Orange Oxidation under Ambient Conditions. *Appl. Catal. B Environ.* **2013**, *130–131* (3), 84–92.

(34) Huang, J.; Wang, X.; Li, S.; Wang, Y. ZnO/MoO3 Mixed Oxide Nanotube: A Highly Efficient and Stable Catalyst for Degradation of Dye by Air under Room Conditions. *Appl. Surf. Sci.* **2010**, *257* (1), 116–121.

(35) Zhang, Y.; Li, D.; Chen, Y.; Wang, X.; Wang, S. Catalytic Wet Air Oxidation of Dye Pollutants by Polyoxomolybdate Nanotubes under Room Condition. *Appl. Catal. B Environ.* **2009**, *86* (3–4), 182–189.

(36) Bokare, A. D.; Chikate, R. C.; Rode, C. V.; Paknikar, K. M. Iron-Nickel Bimetallic Nanoparticles for Reductive Degradation of Azo Dye Orange G in Aqueous Solution. *Appl. Catal. B Environ.* **2008**, *79* (3), 270–278.

(37) Leiw, M. Y.; Guai, G. H.; Wang, X.; Tse, M. S.; Ng, C. M.; Tan, O. K. Dark Ambient Degradation of Bisphenol A and Acid Orange 8 as Organic Pollutants by Perovskite $SrFeO_3$ -δ Metal Oxide. *J. Hazard. Mater.* **2013**, *260*, 1–8.

(38) Dvininov, E.; Joshi, U. a; Darwent, J. R.; Claridge, J. B.; Xu, Z.; Rosseinsky, M. J. Room Temperature Oxidation of Methyl Orange and Methanol over Pt-HCa2Nb3O10 and Pt-WO3 Catalysts without Light. *Chem. Commun. (Camb).* **2011**, *47* (3), 881–883.

(39) Li, G.; Zhang, Y.; Wu, L.; Wu, F.; Wang, R.; Zhang, D.; Zhu, J.; Li, H. An Efficient Round-the-Clock La2NiO4 Catalyst for Breaking down Phenolic Pollutants. *RSC Adv.* **2012**, *2* (11), 4822.

(40) Sun, M.; Jiang, Y.; Li, F.; Xia, M.; Xue, B.; Liu, D. Dye Degradation Activity and Stability of Perovskite-Type LaCoO3−x (x=0∼0.075). *Mater. Trans.* **2010**, *51* (12), 2208–2214.

(41) Fierro, J. L. G.; Tascón, J. M. D.; González Tejuca, L. Surface Properties of LaNiO3: Kinetic Studies of Reduction and of Oxygen Adsorption. *J. Catal.* **1985**, *93*, 83–91.

(42) Royer, S.; Levasseur, B.; Alamdari, H.; Barbier, J.; Duprez, D.; Kaliaguine, S. Mechanism of Stearic Acid Oxidation over Nanocrystalline L a1 - X A′x B O3 (A′ = Sr, Ce; B = Co, Mn): The Role of Oxygen Mobility. *Appl. Catal. B Environ.* **2008**, *80* (1–2), 51–61.

(43) Pere??iguez, R.; Gonzalez-delaCruz, V. M.; Caballero, A.; Holgado, J. P. LaNiO 3 as a Precursor of Ni/La 2O 3 for CO 2 Reforming of CH 4: Effect of the Presence of an Amorphous NiO Phase. *Appl. Catal. B Environ.* **2012**, *123–124*, 324–332.

(44) Gallego, J.; Batiot-Dupeyrat, C.; Barrault, J.; Mondragón, F. Severe Deactivation of a LaNiO3 Perovskite-Type Catalyst Precursor with H2S during Methane Dry Reforming. *Energy and Fuels* **2009**, *23* (10), 4883–4886.

(45) Ling, T.; Chen, Z.; Lee, M. Studies on Catalytic and Conductive Properties of LaNiO3 for Oxidation of C2HsOH, CH3CHO, and CH4. **1995**, *26*, 79–86.

(46) Ling, T. R.; Chen, Z. B.; Lee, M. D. Catalytic Behavior and Electrical Conductivity of LaNiO3 in Ethanol Oxidation. *Appl. Catal. A Gen.* **1996**, *136* (2), 191–203.

(47) Li, Y.; Yao, S.; Wen, W.; Xue, L.; Yan, Y. Sol-Gel Combustion Synthesis and Visible-Light-Driven Photocatalytic Property of Perovskite LaNiO3. *J. Alloys Compd.* **2010**, *491* (1–2), 560–564.

(48) Choisnet, Jacques; Abadzhieva, Nevena; Stefanov, Plamen; Klissurski, Dimitar; Marc Bassat, Jean; Rives, V. X-Ray Photoelectron Spectroscopy, Temperature-Programmed Desorption and Temperature-Programmed Reduction Study of LaNiO3 and La2NiO4+d Catalysts for Methanol Oxidation. *J.Chem.Soc.Faraday Trans.* **1994**, *90* (13), 1987–1991.

(49) Qiao, L.; Bi, X. Direct Observation of Ni 3+ and Ni 2+ in Correlated LaNiO 3−δ Films. *EPL (Europhysics Lett.* **2011**, *93* (5), 57002.

(50) Gibert, M.; Zubko, P.; Scherwitzl, R.; Íñiguez, J.; Triscone, J.-M. Exchange Bias in LaNiO3–LaMnO3 Superlattices. *Nat. Mater.* **2012**, *11* (3), 195–198.

(51) Suntivich, J.; Gasteiger, H. a; Yabuuchi, N.; Nakanishi, H.; Goodenough, J. B.; Shao-Horn, Y. Design Principles for Oxygen-Reduction Activity on Perovskite Oxide Catalysts for Fuel Cells and Metal-Air Batteries. *Nat. Chem.* **2011**, *3* (7), 546–550.

(52) Czuprat, O.; Arnold, M.; Schirrmeister, S.; Schiestel, T.; Caro, J. Influence of CO2 on the Oxygen Permeation Performance of Perovskite-Type BaCoxFeyZrzO3-?? Hollow Fiber Membranes. *J. Memb. Sci.* **2010**, *364* (1–2), 132–137.

(53) Efimov, K.; Czuprat, O.; Feldhoff, A. In-Situ X-Ray Diffraction Study of Carbonate Formation and Decomposition in Perovskite-Type BCFZ. *J. Solid State Chem.* **2011**, *184* (5), 1085–1089.

(54) Kaus, I.; Wiik, K.; Krogh, B.; Dahle, M.; Hofstad, K. H.; Aasland, S. Stability of SrFeO 3 -Based Materials in H 2 O/CO 2 -Containing Atmospheres at High Temperatures and Pressures. *J. Am. Ceram. Soc.* **2007**, *90* (7), 2226–2230.

(55) Hu, B.; Mahapatra, M. K.; Keane, M.; Zhang, H.; Singh, P. Effect of CO2 on the Stability of Strontium Doped Lanthanum Manganite Cathode. *J. Power Sources* **2014**, *268*, 404–413.

(56) Sun, M.; Jiang, Y.; Li, F.; Xia, M.; Xue, B.; Liu, D. Structure, Dye Degradation Activity and Stability of Oxygen Defective BaFeO3-X. *Mater. Trans.* **2010**, *51* (11), 1981–1989.

(57) Sun, M.; Jiang, Y.; Li, F.; Xia, M.; Xue, B.; Liu, D. Dye Degradation Activity and Stability of Perovskite-Type LaCoO3−x (x=0∼0.075). *Mater. Trans.* **2010**, *51* (12), 2208–2214.

(58) Gou, G.; Grinberg, I.; Rappe, A. M.; Rondinelli, J. M. Lattice Normal Modes and Electronic Properties of the Correlated Metal LaNiO3. *Phys. Rev. B - Condens. Matter Mater. Phys.* **2011**, *84* (14), 1–13.

(59) Jeon, Y.; Park, D.-H.; Park, J.-I.; Yoon, S.-H.; Mochida, I.; Choy, J.-H.; Shul, Y.-G. Hollow Fibers Networked with Perovskite Nanoparticles for H2 Production from Heavy Oil. *Sci. Rep.* **2013**, *3*, 2902.

(60) Jeevanandam, P.; Koltypin, Y.; Palchik, O.; Gedanken, a. Synthesis of Morphologically Controlled Lanthanum Carbonate Particles Using Ultrasound Irradiation. *J. Mater. Chem.* **2001**, *11* (3), 869–873.

(61) Salavati-Niasari, M.; Hosseinzadeh, G.; Davar, F. Synthesis of Lanthanum Hydroxide and Lanthanum Oxide Nanoparticles by Sonochemical Method. *J. Alloys Compd.* **2011**, *509* (10), 4098–4103.

(62) Pecora, W. T.; Kerr, J. H. Burbankite and Calkinsite , Two New Cabonate Minerals from Montana. *Am. Miner.* **1953**, *38*, 1169–1183.

(63) Busca, G.; Berardinelli, S.; Resini, C.; Arrighi, L. Technologies for the Removal of Phenol from Fluid Streams: A Short Review of Recent Developments. *J. Hazard. Mater.* **2008**, *160* (2–3), 265–288.

(64) Baiocchi, C.; Brussino, M. C.; Pramauro, E.; Bianco, A.; Palmisano, L.; Marc, G. Characterization of Methyl Orange and Its Photocatalytic Degradation Products by HPLC / UV – VIS Diode Array and Atmospheric Pressure Ionization Quadrupole Ion Trap Mass Spectrometry. **2002**, *214*, 247–256.

(65) Parshetti, G. K.; Telke, a a; Kalyani, D. C.; Govindwar, S. P. Decolorization and Detoxification of Sulfonated Azo Dye Methyl Orange by Kocuria Rosea MTCC 1532. *J. Hazard. Mater.* **2010**, *176* (1–3), 503–509.

(66) Murali, V.; Ong, S. A.; Ho, L. N.; Wong, Y. S. Evaluation of Integrated Anaerobic-Aerobic Biofilm Reactor for Degradation of Azo Dye Methyl Orange. *Bioresour. Technol.* **2013**, *143*, 104–111.

(67) Cai, P. J.; Xiao, X.; He, Y. R.; Li, W. W.; Chu, J.; Wu, C.; He, M. X.; Zhang, Z.; Sheng, G. P.; Lam, M. H. W.; Xu, F.; Yu, H. Q. Anaerobic Biodecolorization Mechanism of Methyl Orange by Shewanella Oneidensis MR-1. *Appl. Microbiol. Biotechnol.* **2012**, *93* (4), 1769–1776.

(68) Burriel, M.; Wilkins, S.; Hill, J. P.; Muñoz-Márquez, M. a.; Brongersma, H. H.; Kilner, J. a.; Ryan, M. P.; Skinner, S. J. Absence of Ni on the Outer Surface of Sr Doped La2NiO4 Single Crystals. *Energy Environ. Sci.* **2014**, *7* (1), 311.

(69) Cabrera-Codony, A.; Montes-Morán, M. a.; Sánchez-Polo, M.; Martín, M. J.; Gonzalez-Olmos, R. Biogas Upgrading: Optimal Activated Carbon Properties for Siloxane Removal. *Environ. Sci. Technol.* **2014**, *48* (12), 7187–7195.

(70) Mito-oka, Y.; Horike, S.; Nishitani, Y.; Masumori, T.; Inukai, M.; Hijikata, Y.; Kitagawa, S. Siloxane D4 Capture by Hydrophobic Microporous Materials. *J. Mater. Chem. A* **2013**, *1* (27), 7885.

(71) de Arespacochaga, N.; Valderrama, C.; Raich-Montiu, J.; Crest, M.; Mehta, S.; Cortina, J. L. Understanding the Effects of the Origin, Occurrence, Monitoring, Control, Fate and Removal of Siloxanes on the Energetic Valorization of Sewage biogas—A Review. *Renew. Sustain. Energy Rev.* **2015**, *52*, 366–381.

(72) Sigot, L.; Ducom, G.; Benadda, B.; Labouré, C. Comparison of Adsorbents for H2S and D4 Removal for Biogas Conversion in a Solid Oxide Fuel Cell. *Environ. Technol.* **2016**, *37* (1), 86–95.

(73) Cabrera-Codony, A.; Gonzalez-Olmos, R.; Martín, M. J. Regeneration of Siloxane-Exhausted Activated Carbon by Advanced Oxidation Processes. *J. Hazard. Mater.* **2015**, *285*, 501–508.

(74) Du, S.; Sun, Y.; Gamliel, D. P.; Valla, J. A.; Bollas, G. M. Catalytic Pyrolysis of Miscanthus??giganteus in a Spouted Bed Reactor. *Bioresour. Technol.* **2014**, *169*, 188–197.

(75) Du, S.; Valla, J. a.; Bollas, G. M. Characteristics and Origin of Char and Coke from Fast and Slow, Catalytic and Thermal Pyrolysis of Biomass and Relevant Model Compounds. *Green Chem.* **2013**, *15*, 3214.

(76) Schweigkofler, M.; Niessner, R. Removal of Siloxanes in Biogases. *J. Hazard. Mater.* **2001**, *83* (3), 183–196.

(77) Dewil, R.; Appels, L.; Baeyens, J. Energy Use of Biogas Hampered by the Presence of Siloxanes. *Energy Convers. Manag.* **2006**, *47* (13–14), 1711–1722.

(78) Soreanu, G.; Béland, M.; Falletta, P.; Edmonson, K.; Svoboda, L.; Al-Jamal, M.; Seto, P. Approaches Concerning Siloxane Removal from Biogas - A Review. *Can. Biosyst. Eng.* **2011**, *53*, 8.1-8.18.

(79) Yu, M.; Gong, H.; Chen, Z.; Zhang, M. Adsorption Characteristics of Activated Carbon for Siloxanes. *J. Environ. Chem. Eng.* **2013**, *1* (4), 1182–1187.

(80) Finocchio, E.; Montanari, T.; Garuti, G.; Pistarino, C.; Federici, F.; Cugino, M.; Busca, G. Purification of Biogases from Siloxanes by Adsorption: On the Regenerability of Activated Carbon Sorbents. *Energy & Fuels* **2009**, *23* (8), 4156–4159.

(81) Higgins, V. L. Siloxane Removal Process. US7,306,652 B2, 2007.

(82) Nam, S.; Namkoong, W.; Kang, J.-H.; Park, J.-K.; Lee, N. Adsorption Characteristics of Siloxanes in Landfill Gas by the Adsorption Equilibrium Test. *Waste Manag.* **2013**, *33* (10), 2091–2098.

(83) Park, J.-K.; Lee, G.-M.; Lee, C.-Y.; Hur, K.-B.; Lee, N.-H. Analysis of Siloxane Adsorption Characteristics Using Response Surface Methodology. *Environ. Eng. Res.* **2012**, *17* (2), 117–122.

(84) Finocchio, E.; Garuti, G.; Baldi, M.; Busca, G. Decomposition of Hexamethylcyclotrisiloxane over Solid Oxides. *Chemosphere* **2008**, *72* (11), 1659–1663.

(85) Lee, Seung-Ho; Cho, Wonihl; Song, Taek-Yong; Kim, Hoyeon; Lee, Woo-Jin; Lee, Young-Chul; Baek, Y. Removal Process for Octamethylcyclotetrasiloxane from Biogas in Sewage Treatment Plant. *J.Ind.Eng.Chem.* **2001**, *7* (5), 276–280.

(86) Jiang, T.; Zhong, W.; Jafari, T.; Du, S.; He, J.; Fu, Y.-J.; Singh, P.; Suib, S. L. Siloxane D4 Adsorption by Mesoporous Aluminosilicates. *Chem. Eng. J.* **2016**, *289*, 356–364.

(87) Kim, Y.; Kim, C.; Choi, I.; Rengaraj, S.; Yi, J. Arsenic Removal Using Mesoporous Alumina Prepared via a Templating Method. *Environ. Sci. Technol.* **2004**, *38* (3), 924–931.

(88) Morris, S. M.; Fulvio, P. F.; Jaroniec, M. Ordered Mesoporous Alumina-Supported Metal Oxides Ordered Mesoporous Alumina-Supported Metal Oxides. *J. Am. Chem. Soc.* **2008**, *130* (October), 15210–15216.

(89) Fulvio, P. F.; Brosey, R. I.; Jaroniec, M. Synthesis of Mesoporous Alumina from Boehmite in the Presence of Triblock Copolymer. *ACS Appl. Mater. Interfaces* **2010**, *2* (2), 588–593.

(90) Kim, P.; Kim, Y.; Kim, H.; Song, I. K.; Yi, J. Synthesis and Characterization of Mesoporous Alumina for Use as a Catalyst Support in the Hydrodechlorination of 1 , 2-Dichloropropane : Effect of Preparation Condition of Mesoporous Alumina. *J. Mol. Catal. A Chem.* **2004**, *219*, 87–95.

(91) Niesz, K.; Yang, P.; Somorjai, G. a. Sol-Gel Synthesis of Ordered Mesoporous Alumina. *Chem. Commun. (Camb).* **2005**, No. 15, 1986–1987.

(92) Wasalathanthri, N. D.; Poyraz, A. S.; Biswas, S.; Meng, Y.; Kuo, C. H.; Kriz, D. A.; Suib, S. L. High-Performance Catalytic CH4 Oxidation at Low Temperatures: Inverse Micelle Synthesis of Amorphous Mesoporous Manganese Oxides and Mild Transformation to K2-xMn8O16 and ??-MnO2. *J. Phys. Chem. C* **2015**, *119* (3), 1473–1482.

(93) Poyraz, A. S.; Song, W.; Kriz, D.; Kuo, C.-H.; Seraji, M. S.; Suib, S. L. Crystalline Mesoporous K2–xMn8O16 and ε-MnO2 by Mild Transformations of Amorphous Mesoporous Manganese Oxides and Their Enhanced Redox Properties. *ACS Appl. Mater. Interfaces* **2014**, *6* (14), 10986–10991.

(94) Song, W.; Poyraz, A. S.; Meng, Y.; Ren, Z.; Chen, S. Y.; Suib, S. L. Mesoporous Co3O4 with Controlled Porosity: Inverse Micelle Synthesis and High-Performance Catalytic Co Oxidation at -60 °c. *Chem. Mater.* **2014**, *26* (15), 4629–4639.

(95) Miao, R.; Luo, Z.; Zhong, W.; Chen, S.-Y.; Jiang, T.; Dutta, B.; Nasr, Y.; Zhang, Y.; Suib, S. L. Mesoporous TiO2 Modified with Carbon Quantum Dots as a High-Performance Visible Light Photocatalyst. *Appl. Catal. B Environ.* **2016**, *189*, 26–38.

(96) Jiang, T.; Du, S.; Jafari, T.; Zhong, W.; Sun, Y.; Song, W.; Luo, Z.; Hines, W. a.; Suib, S. L. Synthesis of Mesoporous γ-Fe2O3 Supported Palladium Nanoparticles and Investigation of Their Roles as Magnetically Recyclable Catalysts for Nitrobenzene Hydrogenation. *Appl. Catal. A Gen.* **2015**, *502*, 105–113.

(97) Jiang, T.; Poyraz, A. S.; Iyer, A.; Zhang, Y.; Luo, Z.; Zhong, W.; Miao, R.; El-Sawy, A. M.; Guild, C. J.; Sun, Y.; Kriz, D. a.; Suib, S. L. Synthesis of Mesoporous Iron Oxides by an Inverse Micelle Method and Their Application in the Degradation of Orange II under Visible Light at Neutral pH. *J. Phys. Chem. C* **2015**, *119* (19), 10454−10468.

(98) Poyraz, A. S.; Kuo, C.-H.; Biswas, S.; King'ondu, C. K.; Suib, S. L. A General Approach to Crystalline and Monomodal Pore Size Mesoporous Materials. *Nat. Commun.* **2013**, *4*, 2952.

(99) Zhao, D.; Feng, J.; Huo, Q.; Melosh, N.; Fredrickson, G.; Chmelka, B.; Stucky, G. Triblock Copolymer Syntheses of Mesoporous Silica with Periodic 50 to 300 Angstrom Pores. *Science* **1998**, *279* (5350), 548–552.

(100) Čejka , Jiří ; Žilková, Naděžda ; Rathouský, Jiří and Zukal, A. Nitrogen Adsorption Study of Organised Mesoporous Alumina. *Phys. Chem. Chem. Phys.* **2001**, *3* (22), 5076–5081.

(101) Zhang, W.; Pinnavaia, T. J. Rare Earth Stabilization of Mesoporous Alumina Molecular Sieves Assembled through an N○I○ Pathway. *Chem. Commun.* **1998**, No. 11, 1185–1186.

(102) Naik, B.; Prasad, V. S.; Ghosh, N. N. Development of a Simple Aqueous Solution Based Chemical Method for Synthesis of Mesoporous γ-Alumina Powders with Disordered Pore Structure. *J. Porous Mater.* **2010**, *17* (1), 115–121.

(103) Cai, W.; Yu, J.; Anand, C.; Vinu, A.; Jaroniec, M. Facile Synthesis of Ordered Mesoporous Alumina and Alumina-Supported Metal Oxides with Tailored Adsorption and Framework Properties. *Chem. Mater.* **2011**, *23* (5), 1147–1157.

(104) Jafari, T.; Noshadi, I.; Khakpash, N.; Suib, S. L. Superhydrophobic and Stable Mesoporous Polymeric Adsorbent for Siloxane Removal: D4 Super-Adsorbent. *J. Mater. Chem. A* **2015**, *3* (9), 5023–5030.

(105) J.M.Bellama; J.Schraml. 29Si Nuclear Magnetic Resonance. In *Determination Of Organic Structures By Physical Methods*; Nachod, F. C., Ed.; Elsevier, 2012; pp 203–268.

(106) Montanari, T.; Finocchio, E.; Bozzano, I.; Garuti, G.; Giordano, A.; Pistarino, C.; Busca, G. Purification of Landfill Biogases from Siloxanes by Adsorption: A Study of Silica and 13X Zeolite Adsorbents on Hexamethylcyclotrisiloxane Separation. *Chem. Eng. J.* **2010**, *165* (3), 859–863.

(107) Sigot, L.; Ducom, G.; Germain, P. Adsorption of Octamethylcyclotetrasiloxane (D4) on Silica Gel (SG): Retention Mechanism. *Microporous Mesoporous Mater.* **2015**, *213*, 118–124.

(108) Yoshitake, H.; Yokoi, T.; Tatsumi, T. Adsorption of Chromate and Arsenate by Amino-Functionalized MCM-41 and SBA-1. *Chem. Mater.* **2002**, *14* (11), 4603–4610.

(109) Bippus, L.; Jaber, M.; Lebeau, B.; Schleich, D.; Scudeller, Y. Thermal Conductivity of Heat Treated Mesoporous Silica Particles. *Microporous Mesoporous Mater.* **2014**, *190*, 109–116.

(110) Soreanu, Gabriela; Béland, Michel; Fallettal, Patricia; Edmonson, Kara; Svoboda, Lewina; Al-Jamal, Mohamad; Seto, P. Approaches Concerning Siloxane Removal from biogas—A Review. *Can. Biosyst. Eng.* **2011**, *53*, 8.1-8.18.

(111) Mitariten, Michael J.; Brown, Roy; Ballantyne, Wayne; Rossin, Joseph; Knapke, M. Regenerative Adsorption Process for Removal of Silicon-Containing Contaminants from Process Gas Using a Neutral Adsorbent Media. US 20140366726A1, 2014.

(112) Yu-Wen Chen, H.-Y. C. and W.-F. L. BASICITIES OF ALUMINA-SUPPORTED ALKALINE EARTH METAL OXIDES. *React.Kinet.Catal.Lett.* **1998**, *65* (1), 83–86.

(113) Seki, T.; Onaka, M. Elucidation of Basic Properties of Mesoporous Alumina through the Temperature-Programmed Desorption of Carbon Dioxide and Heterogeneous Basic Catalysis of Mesoporous Alumina for the Knoevenagel Reaction in Supercritical CO2. *J. Mol. Catal. A Chem.* **2007**, *263* (1–2), 115–120.

(114) Poyraz, A. S.; Kuo, C.-H.; Kim, E.; Meng, Y.; Seraji, M. S.; Suib, S. L. Tungsten-Promoted Mesoporous Group 4 (Ti, Zr, and Hf) Transition-Metal Oxides for Room-Temperature Solvent-Free Acetalization and Ketalization Reactions. *Chem. Mater.* **2014**, *26* (9), 2803–2813.

(115) Mallesham, B.; Sudarsanam, P.; Raju, G.; Reddy, B. M. Design of Highly Efficient Mo and W-Promoted SnO2 Solid Acids for Heterogeneous Catalysis: Acetalization of Bio-Glycerol. *Green Chem.* **2013**, *15* (2), 478–489.

(116) Wang, G.; Zhang, L.; Dai, H.; Deng, J.; Liu, C.; He, H.; Au, C. T. P123-Assisted Hydrothermal Synthesis and Characterization of Rectangular Parallelepiped and Hexagonal Prism Single-Crystalline Mgo with Three-Dimensional Wormholelike Mesopores. *Inorg. Chem.* **2008**, *47* (10), 4015–4022.

(117) Zhu, Q.; Wegener, S. L.; Xie, C.; Uche, O.; Neurock, M.; Marks, T. J. Sulfur as a Selective "Soft" Oxidant for Catalytic Methane Conversion Probed by Experiment and Theory. *Nat. Chem.* **2013**, *5* (2), 104–109.

(118) Gélin, P.; Urfels, L.; Primet, M.; Tena, E. Complete Oxidation of Methane at Low Temperature over Pt and Pd Catalysts for the Abatement of Lean-Burn Natural Gas Fuelled Vehicles Emissions: Influence of Water and Sulphur Containing Compounds. *Catal. Today* **2003**, *83* (1–4), 45–57.

(119) Gélin, P.; Primet, M. Complete Oxidation of Methane at Low Temperature over Noble Metal Based Catalysts: A Review. *Appl. Catal. B Environ.* **2002**, *39* (1), 1–37.

(120) Chen, J.; Zhang, X.; Arandiyan, H.; Peng, Y.; Chang, H.; Li, J. Low Temperature Complete Combustion of Methane over Cobalt Chromium Oxides Catalysts. *Catal. Today* **2013**, *201*, 12–18.

(121) Machej, T.; Serwicka, E. M.; Zimowska, M.; Dula, R.; Michalik-Zym, A.; Napruszewska, B.; Rojek, W.; Socha, R. Cu/Mn-Based Mixed Oxides Derived from Hydrotalcite-like Precursors as Catalysts for Methane Combustion. *Appl. Catal. A Gen.* **2014**, *474*, 87–94.

(122) Farrauto, R. J. Low-Temperature Oxidation of Methane. *Science (80-.).* **2012**, *337* (6095), 659 LP-660.

(123) Zarur, A. J.; Ying, J. Y. Reverse Microemulsion Synthesis of Nanostructured Complex Oxides for Catalytic Combustion. *Nature* **2000**, *403* (6765), 65–67.

(124) Ponce, S.; Peña, M. A.; Fierro, J. L. G. Surface Properties and Catalytic Performance in Methane Combustion of Sr-Substituted Lanthanum Manganites. *Appl. Catal. B Environ.* **2000**, *24* (3–4), 193–205.

(125) Urdă, A.; Popescu, I.; Cacciaguerra, T.; Tanchoux, N.; Tichit, D.; Marcu, I.-C. Total Oxidation of Methane over Rare Earth Cation-Containing Mixed Oxides Derived from LDH Precursors. *Appl. Catal. A Gen.* **2013**, *464–465*, 20–27.

(126) Tao, F. F.; Shan, J.-J.; Nguyen, L.; Wang, Z.; Zhang, S.; Zhang, L.; Wu, Z.; Huang, W.; Zeng, S.; Hu, P. Understanding Complete Oxidation of Methane on Spinel Oxides at a Molecular Level. *Nat. Commun.* **2015**, *6*, 7798.

(127) Hu, L.; Peng, Q.; Li, Y. Selective Synthesis of Co3O4 Nanocrystal with Different Shape and Crystal Plane Effect on Catalytic Property for Methane Combustion. *J. Am. Chem. Soc.* **2008**, *130* (48), 16136–16137.

(128) Kim, P.; Kim, Y.; Kim, H.; Song, I. K.; Yi, J. Synthesis and Characterization of Mesoporous Alumina with Nickel Incorporated for Use in the Partial Oxidation of Methane into Synthesis Gas. *Appl. Catal. A Gen.* **2004**, *272* (1–2), 157–166.

(129) Águila, G.; Gracia, F.; Cortés, J.; Araya, P. Effect of Copper Species and the Presence of Reaction Products on the Activity of Methane Oxidation on Supported CuO Catalysts. *Appl. Catal. B Environ.* **2008**, *77* (3–4), 325–338.

(130) Wierzchowski, P. T.; Zatorski, L. W. Kinetics of Catalytic Oxidation of Carbon Monoxide and Methane Combustion over Alumina Supported Ga2O3, SnO2 or V2O5. *Appl. Catal. B Environ.* **2003**, *44* (1), 53–65.

(131) Park, P.; Ledford, J. The Influence of Surface Structure on the Catalytic Activity of Alumina Supported Copper Oxide Catalysts Oxidation of Carbon Monoxide and Methane. *Appiled Catal. B Environ.* **1998**, *15*, 221–231.

(132) Park, H. S.; Lee, Y. C.; Choi, B. G.; Hong, W. H.; Yang, J. W. Clean and Facile Solution Synthesis of iron(III)-Entrapped ??-Alumina Nanosorbents for Arsenic Removal. *ChemSusChem* **2008**, *1* (4), 356–362.

(133) Craciun, R.; Nentwick, B.; Hadjiivanov, K.; Knözinger, H. Structure and Redox Properties of MnOx/Yttrium-Stabilized Zirconia (YSZ) Catalyst and Its Used in CO and CH4 Oxidation. *Appl. Catal. A Gen.* **2003**, *243* (1), 67–79.

(134) Al-Sayari, S. A. Recent Developments in the Partial Oxidation of Methane to Syngas. *Open Catal. J.* **2013**, *6* (2), 17–28.

(135) Li, Chun-Yi; Zhang, Zhao-Bin; Yu, Chang-Chun and Shen, S.-K. Temperature-Programmed Studies on Partial Oxidation of CH(4) to Syngas Over a Ni/Al(2)O(3) Catalyst. *Fuel Chem. Div. Prepr.* **2002**, *47* (1), 123–125.

(136) York, A. P. E.; Xiao, T.; Ã, M. L. H. G. Brief Overview of the Partial Oxidation of Methane to Synthesis Gas. *Top. Catal.* **2003**, *22* (3–4), 345–358.

(137) Xing, Y.; Liu, Z.; Gomez, S.; Suib, S. L. Tuning of Texture and Structure of Copper-Containing Nanocomposite Oxide Materials. *J. Phys. Chem. C* **2008**, *112* (5), 1446–1454.

(138) Dou, X.; Mohan, D.; Zhao, X.; Pittman, C. U. Antimonate Removal from Water Using Hierarchical Macro-/mesoporous Amorphous Alumina. *Chem. Eng. J.* **2015**, *264*, 617–624.

(139) Filella, M.; Belzile, N.; Chen, Y.-W. Antimony in the Environment: A Review Focused on Natural Waters: I. Occurrence. *Earth-Science Rev.* **2002**, *57* (1–2), 125–176.

(140) Filella, M.; Belzile, N.; Chen, Y.-W. Antimony in the Environment: A Review Focused on Natural Waters: II. Relevant Solution Chemistry. *Earth-Science Rev.* **2002**, *59* (1–4), 265–285.

(141) Fu, Z.; Wu, F.; Amarasiriwardena, D.; Mo, C.; Liu, B.; Zhu, J.; Deng, Q.; Liao, H. Antimony, Arsenic and Mercury in the Aquatic Environment and Fish in a Large Antimony Mining Area in Hunan, China. *Sci. Total Environ.* **2010**, *408* (16), 3403–3410.

(142) He, M.; Wang, X.; Wu, F.; Fu, Z. Antimony Pollution in China. *Sci. Total Environ.* **2012**, *421–422*, 41–50.

(143) Ramadugu, S. K.; Mason, S. E. DFT Study of Antimony (V) Oxyanion Adsorption on α-Al2O3 (1-102). *J. Phys. Chem. C* **2015**, *119* (32), 18149–18159.

(144) Shan, C.; Ma, Z.; Tong, M. Efficient Removal of Trace antimony(III) through Adsorption by Hematite Modified Magnetic Nanoparticles. *J. Hazard. Mater.* **2014**, *268*, 229–236.

(145) Salam, M. A.; Mohamed, R. M. Removal of Antimony (III) by Multi-Walled Carbon Nanotubes from Model Solution and Environmental Samples. *Chem. Eng. Res. Des.* **2013**, *91* (7), 1352–1360.

(146) Nishiyama, S.; Saito, K.; Saito, K.; Sugita, K.; Sato, K.; Akiba, M.; Saito, T.; Tsuneda, S.; Hirata, A.; Tamada, M.; Sugo, T. High-Speed Recovery of Antimony Using Chelating Porous Hollow-Fiber Membrane. *J. Memb. Sci.* **2003**, *214* (2), 275–281.

(147) Guo, X.; Wu, Z.; He, M. Removal of antimony(V) and antimony(III) from Drinking Water by Coagulation–flocculation–sedimentation (CFS). *Water Res.* **2009**, *43* (17), 4327–4335.

(148) Wilson, S. C.; Lockwood, P. V; Ashley, P. M.; Tighe, M. The Chemistry and Behaviour of Antimony in the Soil Environment with Comparisons to Arsenic: A Critical Review. *Environ. Pollut.* **2010**, *158* (5), 1169–1181.

(149) Li, X.; Dou, X.; Li, J. Antimony(V) Removal from Water by Iron-Zirconium Bimetal Oxide: Performance and Mechanism. *J. Environ. Sci.* **2012**, *24* (7), 1197–1203.

(150) Leng, Y.; Guo, W.; Su, S.; Yi, C.; Xing, L. Removal of antimony(III) from Aqueous Solution by Graphene as an Adsorbent. *Chem. Eng. J.* **2012**, *211–212*, 406–411.

(151) Yu, M. J.; Li, X.; Ahn, W. S. Adsorptive Removal of Arsenate and Orthophosphate Anions by Mesoporous Alumina. *Microporous Mesoporous Mater.* **2008**, *113* (1–3), 197–203.

(152) Han, C.; Li, H.; Pu, H.; Yu, H.; Deng, L.; Huang, S.; Luo, Y. Synthesis and Characterization of Mesoporous Alumina and Their Performances for Removing arsenic(V). *Chem. Eng. J.* **2013**, *217*, 1–9.

(153) Lai, X.; Li, X.; Geng, W.; Tu, J.; Li, J.; Qiu, S. Ordered Mesoporous Copper Oxide with Crystalline Walls. *Angew. Chemie - Int. Ed.* **2007**, *46* (5), 738–741.

(154) Cargnello, M.; Jaen, J. J. D.; Garrido, J. C. H.; Bakhmutsky, K.; Montini, T.; Gamez, J. J. C.; Gorte, R. J.; Fornasiero, P. Exceptional Activity for Methane Combustion over Modular Pd@CeO2 Subunits on Functionalized Al2O3. *Science (80-.).* **2012**, *337* (6095), 713–717.

(155) Díaz, I.; González-Pena, V.; Márquez-Alvarez, C.; Kikkinides, E. S. Transmission Electron Microscopy Combined with Stochastic Reconstruction Methods for Structural Characterization of Porous Alumina Synthesized via Non-Ionic Surfactant-Templating Route. *Microporous Mesoporous Mater.* **2004**, *68* (1–3), 11–19.

Appendix

- **Journal articles and book chapter:**

NO.	List of Author(s), Article Title, Journal Title , Year of Publication, Volume #, Issue #, Pages	No. of Citations
1.	**Wei Zhong**, Ting Jiang, Tahereh Jafari, Altug S. Poyraz, Wei Wu, David A. Kriz, Shoucheng Du, Sourav Biswas, Michael Thompson Pettes, Steven L. Suib. Modified inverse micelle synthesis for mesoporous alumina with a high D4 siloxane adsorption capacity. Microporous and Mesoporous Materials, 2017, 239:328-335.	
2.	**Wei Zhong**, Ting Jiang, Sheng-Yu Chen, Chung-Hao Kuo, David Kriz, Junkai He, Andrew Meguerdichian, Zhu Luo, Steven L. Suib. Non-photocatalytic Dye Removal from Water by Perovskite-type $LaNiO_{3-\delta}$ Material. In manuscript.	
3.	**Wei Zhong**, Niluka D. Wasalathanthri , Yanliu Dang, Tharindu Kankanam, Junkai He, Seven L. Suib. Methane Oxidation for Efficient Utilization of Natural Gas. In manuscript.	

4.	Ran Miao, Junkai He, Sanjubala Sahoo, Zhu Luo, **Wei Zhong**, Sheng-Yu Chen, Curtis Guild, Tahereh Jafari, Biswanath Dutta, Shaylin A Cetegen, Mingchao Wang, S. Pamir Alpay, Steven L. Suib. Reduced graphene oxide supported nickel−manganese−cobalt spinel ternary oxide nanocomposites and their chemically converted sulfide nanocomposites as efficient electrocatalysts for alkaline water splitting. ACS Catalysis, 2017, 7(1):819-832.	2
5.	Ben Liu, Pu Wang, Aaron Lopes, Lei Jin, **Wei Zhong**, Yong Pei, Steven L. Suib and Jie He. Au–carbon electronic interaction mediated selective oxidation of styrene. ACS Catalysis, 2017,7(5): 3483-3488.	
6.	Ting Jiang, **Wei Zhong**, Tahereh Jafari, Shoucheng Du, Junkai He, You-Jun Fu, Prabhakar Singh, Steven L.Suib. Siloxane D4 adsorption by mesoporous aluminosilicates. Chemical Engineering Journal, 2016, 289:356-364.	13
7.	Tahereh Jafari, Ting Jiang, **Wei Zhong**, Nasser Khakpash, Bahareh Deljoo, Mark Aindow, Prabhakar Singh, Steven L. Suib. Modified mesoporous silica for efficient siloxane capture. Langmuir, 2016, 32: 2369-2377.	9
8.	Ran Miao, Zhu Luo, **Wei Zhong**, Sheng-Yu Chen, Ting Jiang, Biswanath Dutta, Youmna Nasr, Yashan Zhang, Steven L.Suib. Mesoporous TiO_2 modified with carbon quantum dots as a high-performance visible light photocatalyst. Applied Catalysis B: Environmental, 2016,189: 26-38.	36

9.	Zhu Luo, Ran Miao, Tran Doan Huan, Islam M. Mosa, Altug S. Poyraz, **Wei Zhong**, Jacqueline E. Cloud, David A. Kriz, Srinivaz Thanneeru, Junkai He, Yashan Zhang, Rampi Ramprasad, Steven L. Suib. Mesoporous MoO_{3-x} material as an efficient electrocatalyst for hydrogen evolution reactions. Advanced Energy Materials, 2016:1600528.	16
10.	Ting Jiang, Shoucheng Du, Tahereh Jafari, **Wei Zhong**, Yu Sun, Wenqiao Song, Zhu Luo, William A. Hines, Steven L. Suib. Synthesis of mesoporous γ-Fe_2O_3 supported palladium nanoparticles and investigation of their roles as magnetically recyclable catalysts for nitrobenzene hydrogenation. Applied Catalysis A: General, 2015, 502:105-113.	11
11.	Ting Jiang, Altug S. Poyraz, Aparna Iyer, Yashan Zhang, Zhu Luo, **Wei Zhong**, Ran Miao, Abdelhamid M. El-Sawy, Curtis J. Guild, Yu Sun, David A. Kriz, and Steven L. Suib. Synthesis of mesoporous iron oxides by an inverse micelle method and their application in the degradation of orange II under visible light at neutral pH. J. Phys. Chem. C, 2015, 119(19): 10454–10468.	23
12.	**Wei Zhong**, Yihan Ling, Yuanyuan Rao, Ranran Peng, Yalin Lu. Calcium doped $Y_3Fe_5O_{12}$ as a new cathode material for intermediate temperature solid oxide fuel cells. Journal of Power Sources, 2012, 213:140-144.	2
13.	Yuanyuan Rao, Zhiquan Wang, **Wei Zhong**, Ranran Peng, Yalin Lu. Novel Ni-$Ba_{1+x}Zr_{0.3}Ce_{0.5}Y_{0.2}O_{3-\delta}$ hydrogen electrodes as effective reduction barriers for reversible solid oxide cells based on doped ceria electrolyte thin film. Journal of Power Sources, 2012, 199:142-145.	18

	Book(s) Title	List of Author(s)	Published by	Percentage of Personal Contribution
1	**Chapter 8**, All-oxides Nanoheterostructures (synthesis, characterization, and properties) in Hybrid Nanocrystal Architectures: Synthesis, Properties, and Applications.	Andrew Meguerdichian, Ting Jiang, **Wei Zhong**. Steven L. Suib.	Imperial College Press	6071 (33%)

- **Patents**

1. **Wei Zhong**, Ting Jiang, Tahereh Jafari, Steven L. Suib. UCT Materials and other Manganese Materials for competitive Organic Sulfur Adsorption. In preparation
2. .
3. Prabhakar Singh, Steven L. Suib, Ting Jiang, **Wei Zhong**, Tahereh Jafari. US 20160129388A1.
4. Tahereh Jafari, Ting Jiang, **Wei Zhong**, Steven L. Suib, Prabhakar Singh. US 20160122186A1.
5. Ranran Peng, Yalin Lu, Yihan Ling, Zhiquan Wang, Yuanyuan Rao, **Wei Zhong**, Xiahui Yao. CN 201210189164.

- **Meeting**

Wei Zhong, Steven L.Suib *et al.* Efficient dye degradation via non-photocatalytic route by perovskite type $LaNiO_{3-\delta}$ materials. 249th American Chemical Society National Meeting, 2015, Denver, CO, USA.

- **Reviewer Service**

1. Chemical Engineering Research and Design;
2. Journal of Physics D: Applied Physics